

POLITECNICO DI TORINO

---

COLLEGIO DI INGEGNERIA MECCANICA, AEROSPAZIALE,  
DELL'AUTOVEICOLO E DELLA PRODUZIONE

Corso di Laurea in Ingegneria Aerospaziale

Tesi di Laurea Magistrale

# Fluid-Structure Interaction analysis of resonant wind generators

Vortex-Induced Vibrations phenomena



**Relatore**

prof. Giuliana Mattiazzo

**Correlatore:**

prof. Giovanni Bracco

**Laureando**

Marco FONTANA

matricola: 224467

---

ANNO ACCADEMICO 2018 – 2019





## **Abstract**

Energy harvesting from natural sources using fluid-elastic phenomena is a new focus of engineering fields, those both industrial than to academic. Several studies, conducted in recent times, indicate as scope of vibration-based energy harvesting the power supply of small devices, like micromechanical systems and sensors.

This thesis aims to analyze and simulate the Fluid-Structure Interaction of two possible harvester designs based on , the Vortex-induced vibrations (VIVs) and the Galloping of prismatic structures. The interaction between a bluff body without streamline shape and the flow field in which is immersed cause self-excited phenomena, the separation occurs arising excitation forces, the behavior concerns Fluid-Structure Interaction. From a classical engineering point of view, these scenarios are considered as problems that have to predict in order to be avoided. The opposite perspective is to exploit these excitations to collect energy from a natural and renewable source, it has to be considered that the potential of such a kind of energy collecting is a debate.

Within this framework, VIVs and Galloping are introduced in the first section of this work. Furthermore, an analysis of the physical models and the parameters involved was carried out. The focus is the Computational Fluid Dynamics simulation of the flow field whose forces due to pressure and shear shall be the external forces of the structure, simulated by FEM-aided analysis.



# Chapter 1

## Introduction

Any body or structure subjected to the fluid flow might be affected by excitations and vibrations, whether they are large or negligible. In case of excessive vibrations, engineers' purpose is avoiding these to suppress damage or failure or even to prevent fatigue phenomena. From the energy harvesting point of view, the scope is to profit by, converting vibrations into usable electric energy.

It is common to bestow the first documentation of vortex shedding upon the sketches of Leonardo Da Vinci (14th century), the first example of a tool based on these vibrations is perhaps the aeolian harp, a musical instrument of ancient Greece (which was solved in a paper by Lord Rayleigh). The scientific and modern studies of vortex shedding started with Strouhal (1878) and von Karman (1912), whereas the vortex-induced vibrations with Bishop & Hassan (1964) [5]. In the previous historical overview, one must pay tribute to the works of Zdravkovich, whose activity leads to the publication of two volumes (1997 [31], 2003 [32]) for a total of more than 1200 pages.

The very first approach to Vortex Induced Vibrations, hereinafter referred as VIVs, was aimed to their suppression to avoid damage and failure of civil structures, in this sense the prime example is the Tacoma Bridge collapse due to vortex-induced vibrations as proven by von Karman tests realized in the wind tunnel at Caltech in the Daniel Guggenheim Aeronautical Laboratory with a model of the entire span constructed to 1/234 scale [2].

The energy harvesting approach is much more recent as shown by Abdelkefi's review (2016) [1] and though years led to the development of various harvesters.

The VIVs based generators are wind power harvesters and they are placed on the energy segment market as competitors of solar technologies, this odd placement will be deepened subsequently. Traditional horizontal axis wind turbine are becoming bigger as show in Fig. 1.2, to maximize performances in terms of annual energy output that varies almost with the cube of the wind speed, so HAWTs became taller, and the square of the rotor diameter.

**Betz Limit** The theoretical maximum efficiency for a wind turbine is the Betz limit and it represents the maximum kinetic energy obtainable from wind that can be used to spin rotor, hence the turbine, in order to generate electricity. Considering the schematic of fluid flow through the rotor in Fig.1.1.

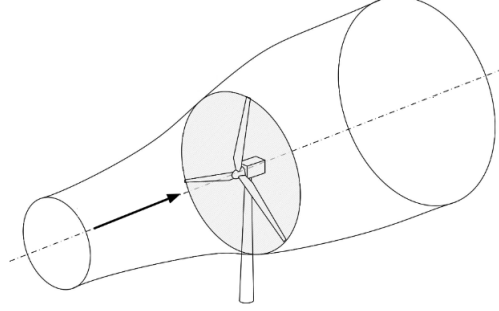


Figure 1.1: Actuator disc model of airstream flow through turbine

If the continuity law holds, and it does, the mass flow rate  $\dot{m}$  is:

$$\dot{m} = \rho V_1 A_1 = \rho V_2 A_2 = \rho V A \quad (1.1)$$

Where  $\rho$  is air density, subscripts 1 and 2 refers respectively to backward and forward fluid flow, while  $A$  and  $V$  are the rotor's area and airstream velocity through. The impulse is equal to momentum variation:

$$Ft = m(V_1 - V_2) \quad (1.2)$$

$$F = \dot{m}(V_1 - V_2) \quad (1.3)$$

Power delivered to the rotor is:

$$P = FV = \dot{m}V(V_1 - V_2) \quad (1.4)$$

On the other hand  $P$  can be obtained considering the power balance through the disc:

$$P = \dot{m} \left( \frac{V_1^2 - V_2^2}{2} \right) \quad (1.5)$$

Hence the velocity at disc is:

$$V = \frac{V_1 + V_2}{2} \quad (1.6)$$

Defining an interference coefficient  $a$  as:

$$a = 1 - \frac{V}{V_1} \quad (1.7)$$

$$\text{so } V = V_1(1 - a) \quad (1.8)$$

$$\text{and } V_2 = V_1(1 - 2a) \quad (1.9)$$

It led to write the power as:

$$P = \rho A V_1 (1 - a) \left( \frac{V_1^2 - V_1^2 (1 - a)}{2} \right) = \quad (1.10)$$

$$= \rho A V_1^3 2a(1 - a)^2 \quad (1.11)$$

By differentiating  $P$  with respect to  $a$ , it is found  $a_{P_{max}} = 1/3$  as the value that maximize the kinetic power  $P$ . Replacing  $a = a_{P_{max}}$ :

$$P = \frac{8}{27} \rho A V_1^3 \quad (1.12)$$

Eq.1.12 must be compared with the power in region 1:

$$P_1 = \frac{\rho A V_1^3}{2} \quad (1.13)$$

The power coefficient is:

$$C_P = \frac{P}{P_1} = \frac{16}{27} = 0.593 \quad (1.14)$$

It represents the is dimensionless ratio of the extractable power  $P$  to the kinetic power  $P_1$  available in the undistributed stream.

Performance's growth leads to reach high efficiency (circa 45%) that is quite close to the Betz limit of 59.7% (that is the equivalent of Carnot limit efficiency for thermal machines). Size growth, as shown in Fig.1.2, even carries some drawbacks which have made traditional wind turbine unpopular. For instance the noise pollution can reach 60dB at low frequencies, wind turbines are a cause of bird mortality about like airplanes and furthermore aesthetic is a point of the debate. It is obvious that the wind sector is crucial in the energy landscape, both in global and national scenarios. The ANEV research “ Il contributo dell'eolico italiano per il raggiungimento degli obiettivi al 2030 ” [28] estimates a potential of 17,150 MW by 2030, of which 950 MW off-shore and 400 MW small-scale, with an annual production of over 36 TWh. At the end of 2016 the wind farm installed in Italy was around 9.3 GW for a production of around 17.5 TWh. It cannot be doubted that the wind energy situation represents an opportunity of economic growth and energy independence, both considering new sites and revamping of the existing ones, with benefits of about 2 billions of euros and thousands of new jobs created [8].

The traditional wind generators cannot be introduced in urban areas, so new concepts of mini wind systems were developed in order to aim a feasible integration. None of these devices can be considered fully completed, some designs were deserted or set aside while other are still in progress.

Two example of concepts are Vortex Bladeless SL and The Saphonian as explained in next chapter.

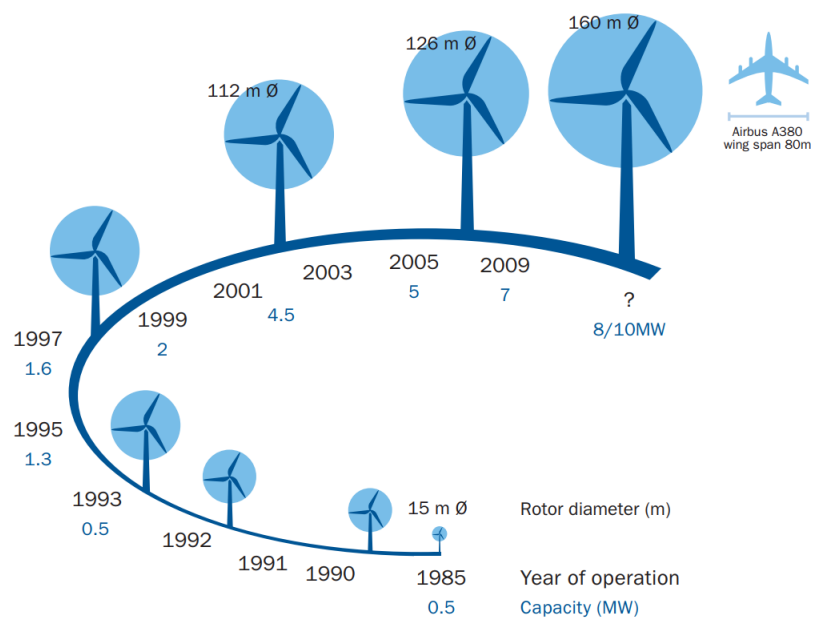


Figure 1.2: Size growth of wind turbines over time [9]



# Chapter 2

## State of the art

Even though the wind industry sees global investments of about \$100 billions, turbine growth and energy conversions are reaching their limits. It should be pointed that these devices are not intended as substitutes to typical wind turbines, but in synergy with conventional harvesters.

New trends of development move in the direction of blade-less technologies and the most important devices are sorted and briefly described in the sections below.

### 2.1 The Saphonian

The first example of these kind of devices is the Saphonian by Saphon Energy shown in Fig. 2.1.



Figure 2.1: The Saphonian

The essential idea is to remove the whole spin system replacing it with a sail-inspired body that mimics the way sailboats convert wind energy into mechanical one. Instead of rotation the kinematics is in 3 dimensions, i.e. a motion in a 3D space without regard to the forces that cause the motion. Developers said the machine reaches an efficiency at least double than a traditional HAWT with the same size. The ease of such a minimal concept leads to a cost more than halved compared to classic turbine with blades.

## 2.2 O-Wind

O-Wind Turbine is an omnidirectional and single axis turbine developed for urban areas. The design is kite-inspired and the spherical shape, shown in Fig.2.2, permits to achieve rotation under omnidirectional winds. The physics behind is quite



Figure 2.2: O-Wind Turbine

simple, based on Bernoulli's principle. The entrance is larger than the exit, so the pressure difference cause the turbine movement that rotate around the fixed axis regardless of wind direction.

## 2.3 Vortex Bladeless

Perhaps the most famous zero-blade device is the Vortex Bladeless, developed by the namesake Spanish SME. The system is a bladeless cylinder (Fig.2.3) that oscillates under the effect of vorticity that generates the well-known vortex pattern called VonKarmann street.

Physics behind the machine is not only due to the vortex pattern but to the synchronization of the vortex shedding frequency and the natural one the structure's vibrations. Structure consists of two parts: the base (i.e. the white part at human



Figure 2.3: Vortex Bladeless

height in Fig.2.3) that includes the anchoring and the location of power output system, and the cylindrical shaped mast that is the oscillating element containing even a tuning system that provides to fit the natural frequency of the structure in order to allow its resonance at different wind speeds.

Vortex Bladeless is clearly a wind harvester which responds to the weaknesses mentioned in Chapter 1, it's harmless to wildlife, quite easy to build and to install, the lack of rotating system led to low maintenance, gears and breaks are absent so no oiling is needed. On the other hand the low frequency vibration brings to noise, the fundamentally turbulent oscillation raise the difficult to optimize the energy harvested, and lastly the conversion to electrical power is based on a piezoelectric system as shown in Fig.2.4 and it drops the efficiency. Furthermore such a device is strongly subjected to fatigue effects that in combination with piezo's low efficiency constituted a non negligible issue.

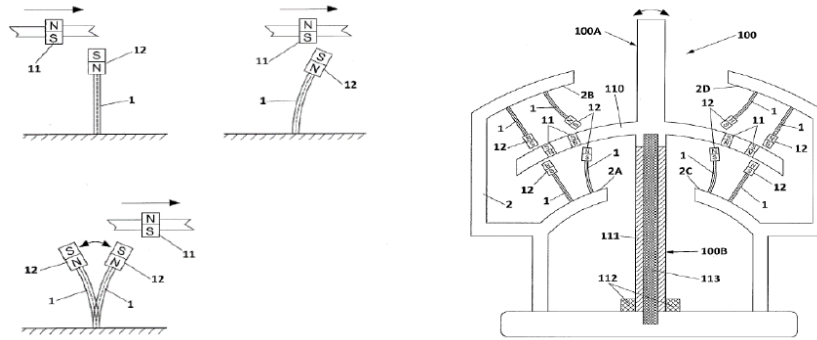


Figure 2.4: Scheme of omnidirectional piezoelectric energy converter

In the eyes of a fluid dynamics engineer the physics of such a device is translated into a fluid-structure interaction analysis whose numerical treatment needs around



10'000 cpu hours [7] without counting the experiments to validate models. The typical CFD based analysis is a sort of cap for such of these problems in terms of computational costs (both time and money) even for supercomputers and HPC systems. This consideration brings newest approaches to promote numerical study which are not based on classic RANS,LES or DNS model. In this thesis a model of this kind is adopted and compared to CFD simulations.

## 2.4 VIVACE

VIVACE (acrostic for Vortex Induced Vibration Aquatic Clean Energy) is a converter of hydrokinetic energy (river or ocean) into an usable form of energy. Invented by Bernitas and Raghavan, patent pending on University of Michigan [4], VIVACE represents an interesting device which exploits VIVs phenomena instead of suppressing it, inverting the typical approach (see Tacoma Bridge) as said in the introductory chapter.

The device consists of a rake of cylinders elastically mounted in a box placed on the bottom of a river or ocean, the current through cylinders allows them to bob up and down exploiting vortices. Each cylinder moves a magnet coil creating DC current. Using water instead of air as energy carrier increases the amount of power output proportionally to the ratio between water's density and air, so about 1000 times higher.

Working with water flows means also dealing with more stable flows, since rivers and ocean currents are distinguished by nearly constant speed and direction which makes it possible an aimed design, matching dimensions and mechanical specification with a well defined current velocity.

This device is the model of reference of this thesis since it is the best example of exploitation of Vortex Induced Vibrations. Unlike the other devices, VIVACE was developed precisely to work in water, that is the largest medium of storing energy, 0.1% of the ocean energy would cover the energy needs of 15 billions of people.

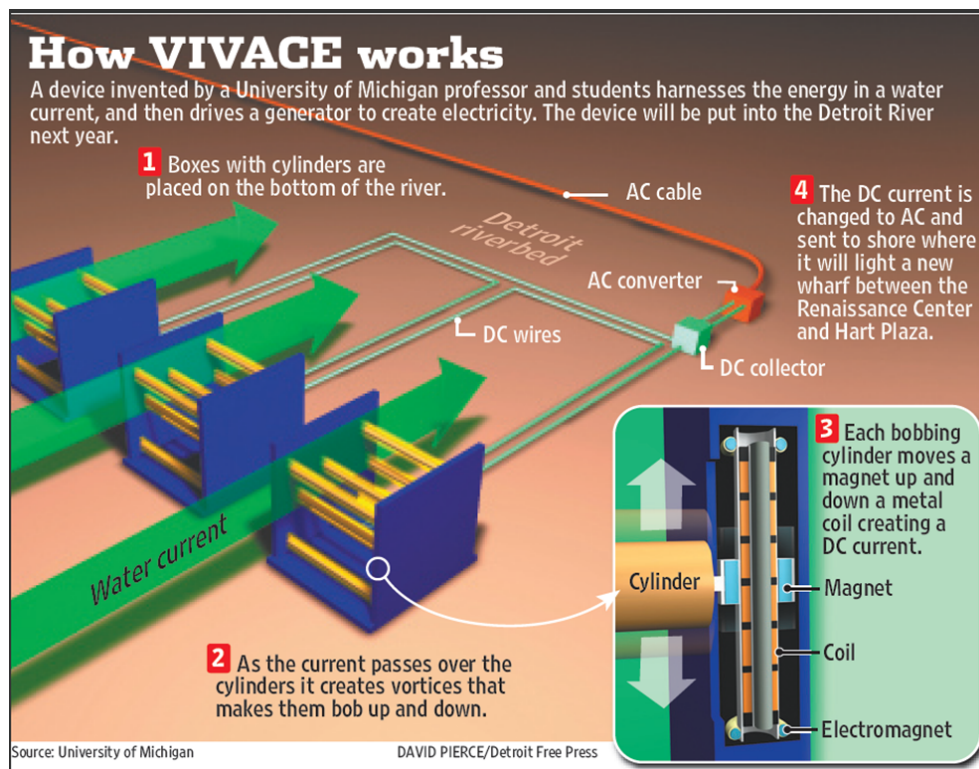


Figure 2.5: VIVACE



## Chapter 3

# Vortex Induced Vibrations

Vortex induced vibrations are a class of the vast phenomena of Flow Induced Vibrations where the interaction between fluid forces and the stressed structure causes a coupling, whose feedback is described in Fig.3.1. The fluid forces due to pressure

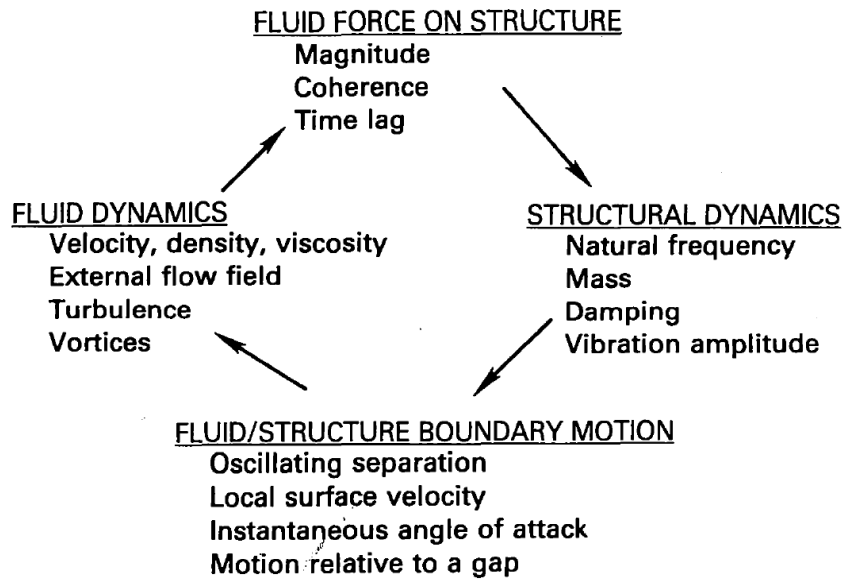


Figure 3.1: Feedback between fluid and structure

and shear, for example, cause the body deformation. As it deforms, the flow state may change and so on. Even in case of rigid structures elastically mounted vibrations may arise. The baseline taxonomy according to Blevins[6] of flow-induced vibrations is shown in Fig. 3.2. To be noticed that vibrations occurs even in case of steady flow, indeed such a kind of excitations are the focus of this thesis.

It ought be noted the distinction between flutter and vortex induced vibrations.

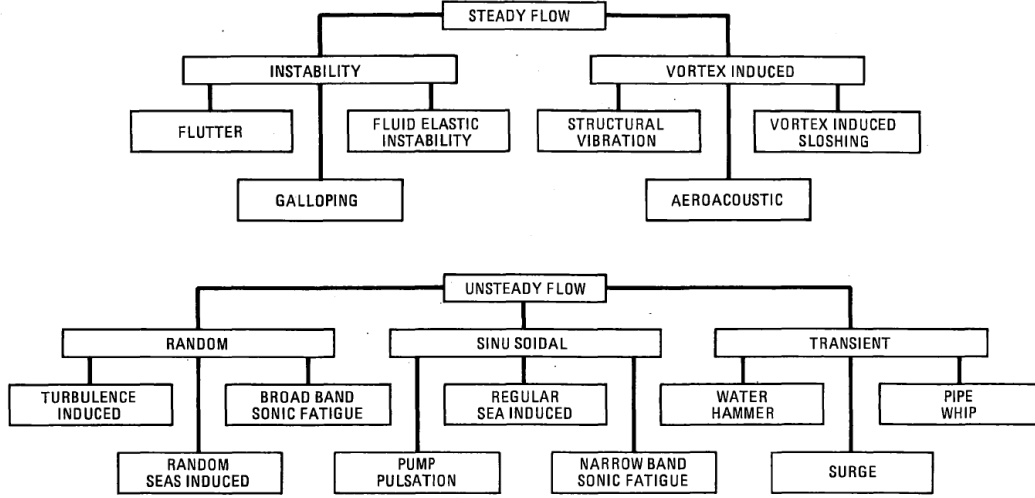


Figure 3.2: A classification of flow induced vibrations

The first phenomenon commonly refers to aerodynamic bodies that oscillate with large amplitude, which generates vortices at wake. In the latter, the oscillations of the structure (not necessary streamlined-shape, actually a bluff body) are caused by vortices.

As well as other fluid dynamic phenomena the aim is the understanding, prediction and eventually the prevention, while in case of energy harvesting is the exploitation. These objectives require simulations that could be direct numerical like DNS with spectral methods, or RANS and LES with particular sub-grid scale models. Anyway, all of these techniques depend upon experiments and measurements with preferably non-intrusive methods. One of major problems in VIV scope are precisely the empirical data obtained through digital particle image velocimetry (DPIV) or laser Doppler or even pressure sensitive paints, which are expensive both in terms of cost and time. The lack of experimental data, especially at high Reynolds, is a critical point in VIVs' studies.

The study of FIV requires the generation of model both for the fluid and the structure. In general the structural models consist of linear equations (systems if more than one degree of freedom is present) since the most of structure's deformations are near-linear with increasing loads.

### 3.1 Flow around cylinders and vortex shedding

In fluid dynamics, study of flow around cylinder is surely one the most thoughtful subject. This flow is fundamentally Reynolds-dependent, that is defined as:

$$Re = \frac{UD}{\nu}$$

where  $U$  is the free-stream velocity,  $D$  the characteristic length (here the diameter of cylinder) and  $\nu$  the kinematic viscosity. Referring to Fig.3.3 it is possible


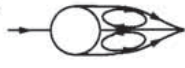







a)		No separation. Creeping flow	$Re < 5$
b)		A fixed pair of symmetric vortices	$5 < Re < 40$
c)		Laminar vortex street	$40 < Re < 200$
d)		Transition to turbulence in the wake	$200 < Re < 300$
e)		Wake completely turbulent. A: Laminar boundary layer separation	$300 < Re < 3 \times 10^5$ Subcritical
f)		A: Laminar boundary layer separation B: Turbulent boundary layer separation; but boundary layer laminar	$3 \times 10^5 < Re < 3.5 \times 10^5$ Critical (Lower transition)
g)		B: Turbulent boundary layer separation; the boundary layer partly laminar partly turbulent	$3.5 \times 10^5 < Re < 1.5 \times 10^6$ Supercritical
h)		C: Boundary layer com- pletely turbulent at one side	$1.5 \times 10^6 < Re < 4 \times 10^6$ Upper transition
i)		C: Boundary layer comple- tely turbulent at two sides	$4 \times 10^6 < Re$ Transcritical

Figure 3.3: Flow around cylinder varying  $Re$  [26]

to identify changes of flow patterns and wake structure increasing the free-stream velocity. A real fluid is considered so the interaction between its viscosity and the

body's surface generates an important boundary layer. Increasing  $U$ , hence  $Re$ , at a certain point a separation of the boundary layer will occur.

The very first Reynolds range, called *Stokes flow*, sees a major influence of viscous effects and the streamlines surround the body. Indeed considering the physical meaning of  $Re$ , i.e. the ratio between inertial forces and viscous ones, the creeping is evident.

Increasing the free-stream velocity in the range  $5 < Re < 40$  separation occurs, a steady re-circulation bubble forms behind the body with two symmetrical counter-rotating vortices; the bubble length increase with increasing  $Re$ . Beyond a certain value of  $Re$ , in case of circular cylinder is  $Re \cong 46$  [27] the previous steady configuration become unstable until the restoration of a new equilibrium. This unsteadiness is characterized by an alternate and periodic shedding of vortices. The laminar vortex street is well-known as *VonKarmann Street* in honour of Theodore VonKarman.

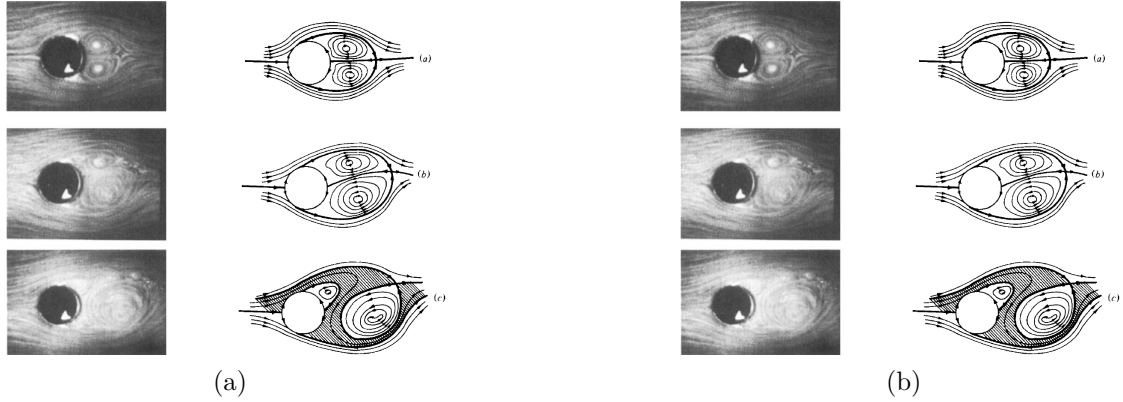


Figure 3.4: Flow in the near wake of a cylinder starting from rest [20]

Vortex shedding exerts an alternate and periodic force on the cylinder, this impose the oscillation in case it was elastically mounted or of distributed elasticity type. It is obvious the importance of shed with respect to Vortex Induced Vibrations.

The periodic pattern recurs with a particular frequency of vortex shedding  $f_{vs}$  that depends by body's shape and free-stream velocity through the *Strouhal number*:

$$f_{vs} = St \frac{U}{D} \quad (3.1)$$

Strouhal number as well as Reynolds will be discussed later in the section of the dimensionless parameters involved in Vortex Induced Vibrations.

## 3.2 Lock-in

Lock-in, also called synchronization, is a crucial phenomenon associated with vortex induced vibrations. In order to understand it a system with natural frequency  $f_n$  is considered. The system is externally excited by an oscillating force with frequency  $f_e$ . It can be observed that when  $f_e$  is close to  $f_n$  there is an interference or beating. When  $f_e$  approaches even more to  $f_n$  the beating vanishes and only a frequency  $f_e$  remains. A practical example is what happen to two or more pendulum clocks hung together on a wall: they were unsynchronized with another one in this condition but became synchronized when suspended to a thin wooden board. This example is know as Huygens's clocks.

In VIVs' study the external force with frequency  $f_e$  is the periodic pressure loading acting due to the vortices structure shed from the body sides. The mutual interaction of these two systems (vortices structure and oscillating body), manifests itself as a non-linear resonance between the fluctuating pressure, externally driving the body, and transversal motion, which may give rise to the synchronization of the system.

An important development of lock-in phenomenon is the violation of Strouhal law, hence vortex shedding is restrained by the body motion. In Fig.3.5 this violation is shown both for air and water, they differs according to the non negligible effect of added mass in case of high density fluid.

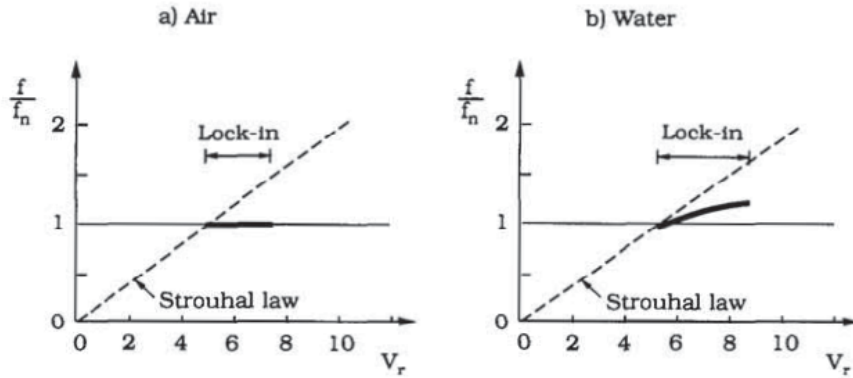


Figure 3.5: Frequency response in air (a) and water (b) with regard to cross-flow vibrations [26]

In these condition ( $f_e$  close to  $f_n$ ) resonance can occur which results in an harmonic oscillation. However, this resonance has showed to be nonlinear and it is reported [17] that no model is actually able to properly predict vortex-induced vibrations in lock-in range varying the mass-damping parameter. Differently from flutter and other aeroelastic instabilities that are fundamentally destructive phenomena, lock-in is self-limited, which means the stable amplitude of the harmonic



oscillation response is bounded to a certain value, typically in the order of the diameter of cylinder, for each velocity at which the body is subjected. Once the flow velocity overcomes the lock-in range the oscillations quickly disappeared.

### 3.3 Pattern of vortex shedding

Vortex Induced Vibrations involves large amplitudes and this afflicts the mode of shedding, that are not now described by the typical vonKarman vortex street model. In 1988, Williamson and Roshko [30] conducted an experimental campaign in order to capture the different patterns of vortex shedding in the range of lock-in. The takeovers acquired by Particle-Image-Velocimetry techniques led to the identification of four modes of vortex shedding as shown in Fig.3.6 where the amplitude ratio  $A^*$  is plotted versus the wavelength  $\lambda = UT_e$ , where  $T_e$  is the period of cylinder oscillation in the transverse y-direction, so  $\lambda$  corresponds to the wavelength of sine wave trajectory along which the body bobs up relative to the fluid. Outside

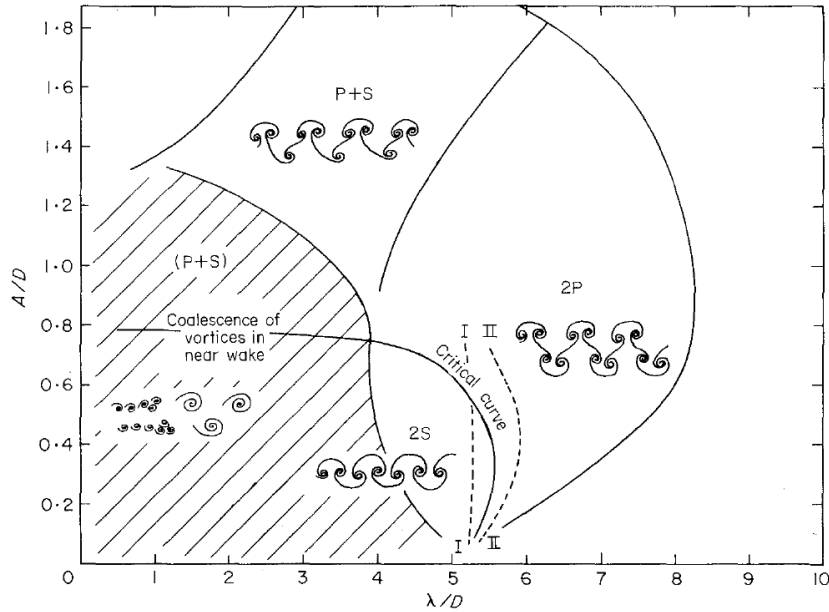


Figure 3.6: Map of vortex synchronization regions

ranges considered in Fig.3.6 there is no synchronized pattern observed. Capitals letter indicates the 4 modes detected, where S refers to the single vortex and P a counter-rotating pair:

2S Is the typical vonKarman vortex street mode where opposite vortices shed alternately from each side of cylinder. So a vortex breaks away from the cylinder every half cycle, the following one shows an opposite direction of

rotation. In lock-in range, the shedding frequency is equal to the natural one of the structure, so the wake acts as an external force introducing power in the system.

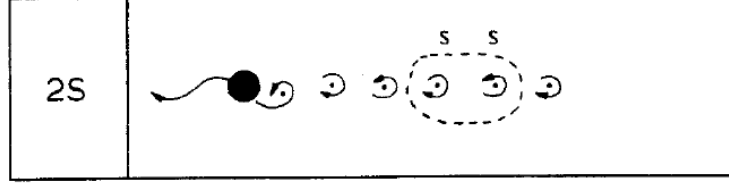


Figure 3.7: 2S Mode

2P This mode indicates the detach of an equal strength vortex pair every half cycle.

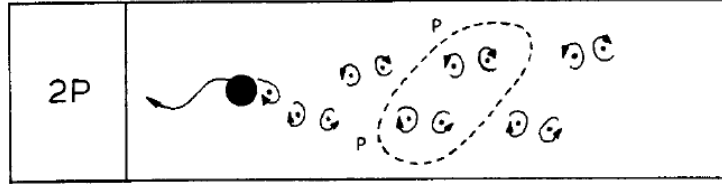


Figure 3.8: 2P Mode

P+S This third mode has a single vortex shed from one side of the cylinder and a pair P shed from the other side. An important outcome about P+S mode is

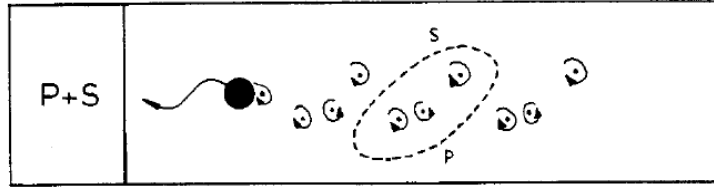


Figure 3.9: P+S Mode

found by Morse and Williamson [18]: energy is transferred to the fluid from the cylinder.

The critical curve in Fig.3.6 marks the transition from mode to another. The curves denoted by I and II refer to the jump in the phase of the lift force relative to the body displacement observed by Bishop and Hassan [5]. There are two different curves because of the hysteresis: I is for wavelength decreasing and II for the wavelength increasing.

### 3.4 VIVs first harmonic model

In summary:

- Alternate and periodic vortex shedding acts as an oscillatory force on cylinder.
- When the frequency of shed is close to the natural one of the structure lock-in occurs and the bluff body tends to vibrate at large amplitude

This implies that Vortex Induced Vibrations is a two-way Fluid-Structure Interaction phenomenon, so structure and wake have to be modeled.

In order to describe the VIV's physics, reference is made to the model in Fig.3.10. The rigid cylinder characterized by mass  $m$ , diameter  $D$  and length  $L$  is subjected

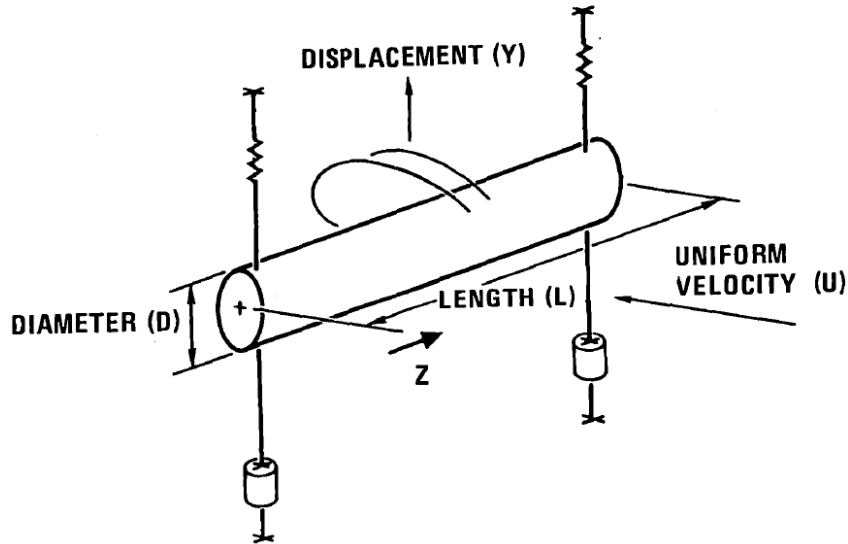


Figure 3.10: Scheme of cylinder elastically mounted

to a uniform flow of water with velocity  $U$ . The body is rigid and elastically mounted, in such a manner it is allowed to oscillate in the cross-flow direction  $y$ : it's a 1-DoF mass-damping-spring model, where supports have damping coefficient  $c$  and stiffness  $k$ .

This first simple model, that has one degree of freedom, is a typical linear oscillator and it allows to consider the cylinder's motion as a result of its interaction with the wake instead of considering a forced motion.

Since vortex shedding is not far from a sinusoidal process, the transverse force, or lift force acting on the cylinder could be assumed as harmonic in time with the shedding frequency:

$$F_L = \frac{1}{2} \rho U^2 D C_L \sin(\omega_s t) \quad (3.2)$$

where:

- $\rho$  : the fluid density
- $U$  : free stream velocity
- $D$  : cylinder diameter
- $C_L$  : lift coefficient
- $\omega_s = 2\pi f_s$  : vortex shedding angular frequency,  $f_s$  is given by Strouhal relation 3.1
- $F_L$  : lift force or transverse force

In the case considered, the cylinder is forced to bob up along transverse direction  $y$  so the governing equation is:

$$m\ddot{y} + 2m\zeta\omega_y\dot{y} + ky = F_L \quad (3.3)$$

where:

- $y$  : displacement along transverse direction with zero at equilibrium position
- $m$  : mass per unit length including the added mass (discussed later)
- $\zeta$  : damping factor
- $\omega_y = \sqrt{k/m}$  angular natural frequency
- $k$  : spring constant, ie. force over displacement

Supposing an harmonic response it is possible to find a solution for the linear governing equation 3.3:

$$y = A_y \sin(\omega_s t + \phi) \quad (3.4)$$

That substituting into 3.3 produces:

$$\frac{y}{D} = \frac{\frac{1}{2}\rho U^2 C_L \sin(\omega_s t + \phi)}{k \sqrt{[1 - (\omega_s/\omega_y)^2]^2 + (2\zeta\omega_s/\omega_y)^2}} \quad (3.5)$$

where the phase angle:

$$\tan \phi = \frac{2\zeta\omega_s\omega_y}{\omega_s^2 - \omega_y^2} \quad (3.6)$$

shifts by  $\pi$  [rad] when system passes through  $f_s = f_y$ , that is the resonance condition.

$$\left. \frac{A_y}{D} \right|_{f_s=f_y} = \frac{\rho U^2 C_L}{4k\zeta} \quad (3.7)$$

The mass  $m$  takes into account both the mass of the structure  $m_s$  and the fluid-added mass  $m_a$ .

In the case of unsteady motion of bodies underwater or unsteady flow around objects, it must be considered the additional effect (force) resulting from the fluid acting on the structure when formulating the system equation of motion. This added effect is *added mass*. In a physical sense, this added mass is the weight added to a system due to the fact that an accelerating or decelerating body must move some volume of surrounding fluid with it as it moves.

$$m_a = C_a \rho D^2 \frac{\pi}{4} \quad (3.8)$$

where  $C_a$  is the added mass coefficient. Considering the potential flow theory it is assumed as a constant value according to Blevins [6].

Similarly, the damping  $c$  models both structure's damping and the fluid-added damping:

$$r = r_s + r_a \quad \text{where} \quad r_a = \gamma \Omega \rho D^2 \quad (3.9)$$

In case of cylinder elastically mounted the frequency  $\Omega$  is equal to the frequency of vortex shedding  $\Omega_f$ . The coefficient  $\gamma$  is related to  $C_D$  but here assumed to be a constant.

Stiffness  $k$  is related to support on which cylinder is mounted.

All masses, dampings and stiffness parameters are defined per unit length.

### 3.5 Dimensionless Parameters

Citing [16] "large number of variables and parameters involved in analytical representations of VIV have been used in early works in this field" so the an important step forward is to identify the most significant parameter involved.

Mass Ratio	$m^*$	$\frac{m_s + m_a}{\rho D^2}$
Damping Ratio	$\zeta$	$\frac{c_s + c_f}{2\sqrt{k(m + m_a)}}$
Reduced Velocity	$U_r$	$\frac{U}{fD}$
Amplitude Ratio	$A^*$	$\frac{A}{D}$

Table 3.1: Dimensioless paramenterers

The effects of parameters in Tab.3.5 is mainly empirical. Firstly, **mass ratio** is considered and described by experimental data by Feng [11] and Khalak-Williamson

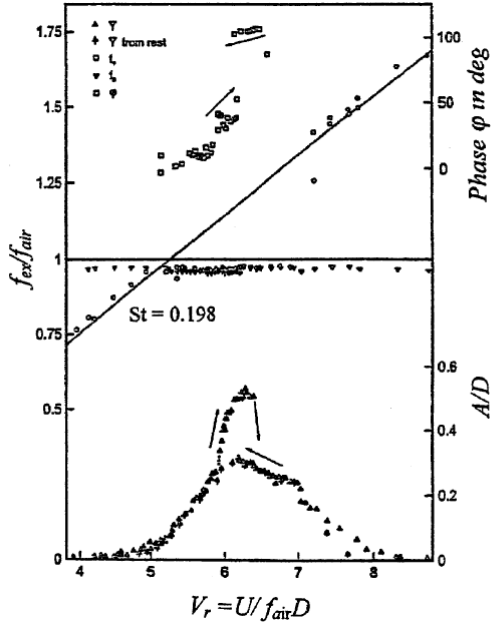


Figure 3.11: Feng's experimental data at high mass ratio

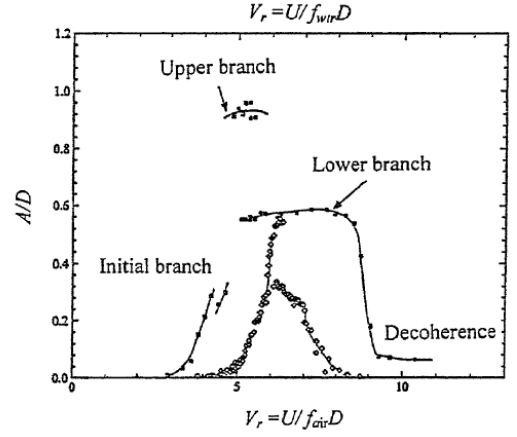


Figure 3.12: Khalak and Williamson's experimental data at small mass ratio

[14] with regards to figures below. In Fig.3.11 are reported responses in terms of amplitude ratio and frequency of a spring-mounted cylinder freely oscillating in air. It is noteworthy that the fluid in which the cylinder is immersed is air, so a small density compared with water, hence a high mass ratio  $m^*$ .

In the second Fig.3.12 it is observed the response of amplitude in water, about 800 times more dense than air, so it refers to cylinder freely oscillating with small mass ratio. Khalak's data are compared with Feng's in Fig.3.12 which show a broader locn-in range and, more important, 3 branches that are absent in case of high mass ratio.

Data of experiments are reported in Tab.3.5.

	$m^*$	$\zeta$	$m^*\zeta$	$A_{peak}$
Feng	248	0.00103	0.255	0.6
K-W	10.1	0.0013	0.013	0.9

Table 3.2: Data of experiments by Feng [11] and Khalak-Williamson [14]

The amplitude response indicates a greater peak in case of small ratio, ie. more dense fluid (water) due to the presence of *Upper Branch*. Khalak and Williamson stated "our studies here [...] indicate that it is principally the parameter  $(m^*\zeta)$ , which influences whether the Upper branch (see Fig.3.12) will appear or not".

This is a first important outcome, first for the physics understanding it results a clear change of response varying mass ratio, second, in terms of energy harvesting, water is more convenient.

Returning to Khalak and Williamson experiments, the rising of three response branches (*Initial*, *Upper* and *Lower*) is detected under condition of low mass-damping. Referring to the Fig.3.13 the transition *Initial* → *Upper* is hysteretic (H), while *Upper* → *Lower* shows an intermittent switching of modes (I).

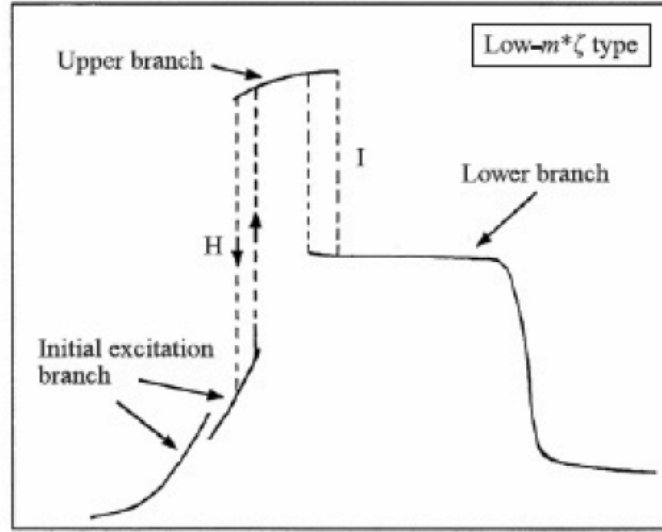


Figure 3.13: Response of low  $m^*\zeta$  system

Damping  $\zeta$ , as show in Tab.3.5, is maily affected by **Damping of fluid**. Differently from structural damping and material's one, the fluid damping is generated in behalf of relative motion between fluid and vibrating structure. Considering the governing equation of motion ??, the force  $F$  could be written through Morrison's equation per units length:

$$F = 0.5\rho C_D D(-\dot{y})|-\dot{y}| + \rho C_a A_{wet}(-\ddot{y}) \quad (3.10)$$

Replacing Eq.3.10 in the equation of motion Eq.??

$$(m + m_a)\ddot{y} + c\dot{y} + 0.5\rho C_D D|\dot{y}|\dot{y} + ky = 0 \quad (3.11)$$

such a solution is obtained:

$$y = A_y \exp(-\zeta\omega_d t) \cos(\omega_d t) \quad (3.12)$$

where  $\omega_d$  is the damping angular frequency defined as  $\omega_d = \omega_N \sqrt{1 - \zeta^2}$  and the

total damping factor  $\zeta = \zeta_s + \zeta_f$  as:

$$\zeta_s = \frac{c}{2\omega_d(m + m_a)} \quad \text{Structural damping factor} \quad (3.13)$$

$$\zeta_f = \frac{8}{3} \frac{\rho D^2}{4\pi(m + m_a)} C_D \frac{A}{D} \quad \text{Fluid damping factor} \quad (3.14)$$

In the expression of the damping factor of fluid it is clear the influence of the amplitude displacement and the added mass.

In VIVs' studies there are different combination of **mass-damping** parameters depending on scope. For instance, in flexible cantilevers, shall read rises, the peak amplitude is plotted versus a stability parameter  $K_S$ :

$$K_S = \pi^2(m^*\zeta) \quad (3.15)$$

From which it derives **Scruton number**:

$$Sc = \frac{\pi}{2}(m^*\zeta) \quad (3.16)$$

The question is: *"what range of value of mass-damping will yield a unique relation between  $A_{peak}$  and  $m^*\zeta$  ?"*. To answer the question **Skop-Griffin parameter** is introduced:

$$S_G = 2\pi^3 St^2(m^*\zeta) \quad (3.17)$$

where  $St$  is the Strouhal number. The scatter data in *Griffin Plot* in Fig.3.14 show

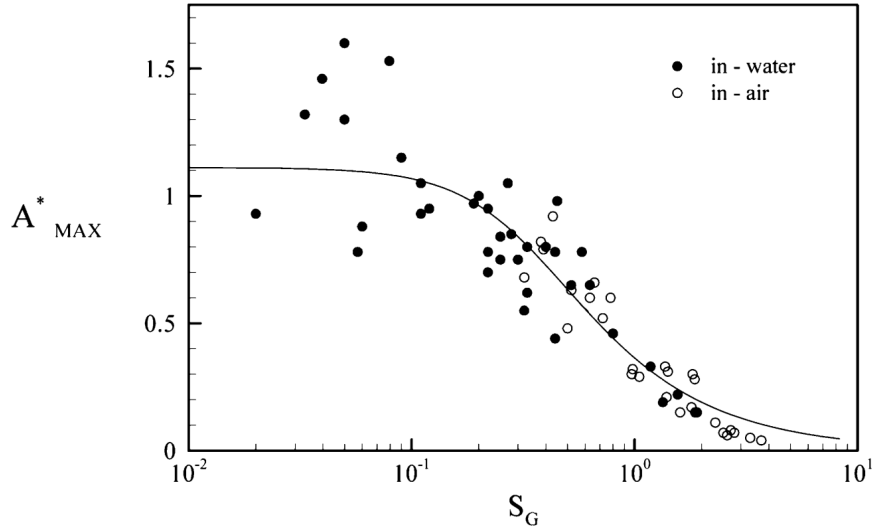


Figure 3.14: Griffin Plot

as the relation  $A_{peak} = f(S_G)$  is satisfactory for wind engineering, where there



are high mass-damping values, while it not acceptable working with more dense fluid like water. Griffin scatter plot in Fig.3.14 also indicates that the amplitude does not exceed two diameters even for very low  $SG$ , say *mass-damping*. Another dependency on Skop-Griffin parameter is the lock-in range as shown in Fig.3.15. The plots 3.14 and 3.15 demonstrate two important features about *self-limitation*

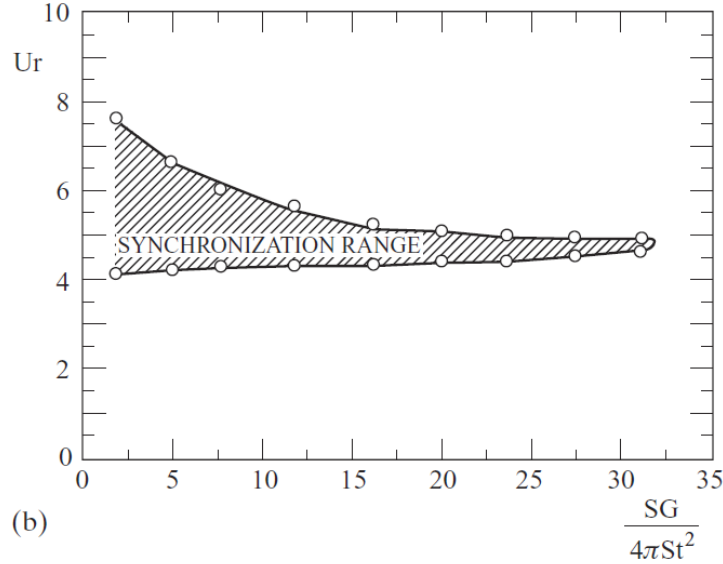


Figure 3.15: Effect of mass-damping parameter on the range of lock-in in terms of reduced velocity  $U_r$

of VIV phenomenon which differentiate it from aero-elastic instabilities such as galloping.

Last parameter described in Eq.3.18 is the **Reduced Velocity**:

$$U_r = \frac{U}{f_n D} \quad (3.18)$$

where  $U$  is the free stream velocity and  $f_n$  the natural frequency of the cylinder. As discussed later, reduced velocity and Strouhal number are related. Indeed resonance occurs when frequency of shedding become equal to that of the structure:

$$St U_r = \frac{f_s D}{U} \frac{U}{f_n D} = \frac{f_s}{f_n} = 1 \quad \text{when resonance occurs} \quad (3.19)$$

In summary the Fig.3.16 below represents the combined effect of reduced velocity and mass damping parameter on amplitude motion of a cylinder elastically mounted with length  $L$ .

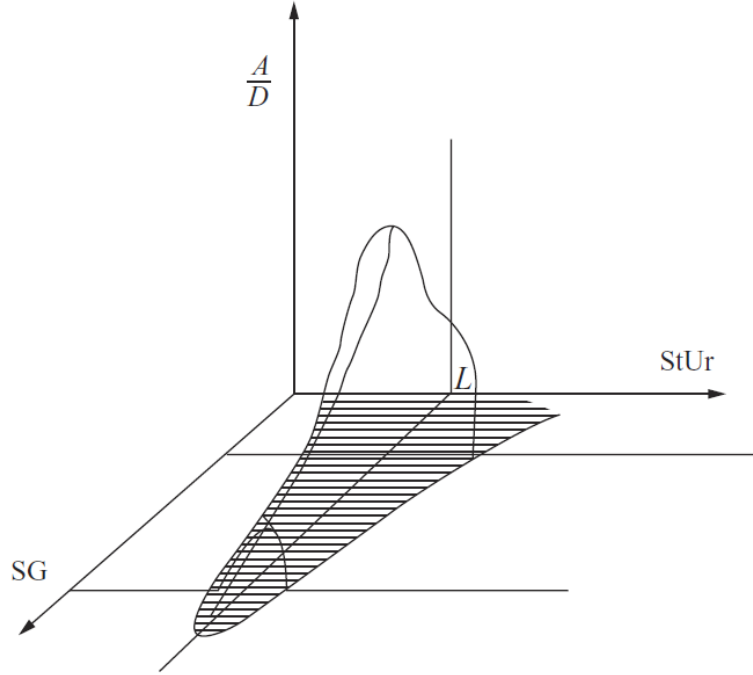


Figure 3.16: Combined effect of reduced velocity-Strouhal number and mass-damping parameter on amplitude ratio of motion of an elastically mounted cylinder due to VIV

### 3.6 Classification of models

The phenomenology of vortex induced vibration summarized gives an idea of the gargantuan number of existing models. Considering only the formulations based on experimental results, hence not all those theoretical models and numerical simulations built only primitive information of the flow, relating to oscillating cylinders treated as rigid solid, all these models could be classified depending on how the fluid-structure interaction is modeled [19].

The classification proposed by Païdoussis is based on the formulation of the fluid force:

$$F_{fluid} = -m_a \ddot{y} + F \quad (3.20)$$

where  $m_a$  is the discussed added mass.

The three type of models in Fig.3.17 can be detected:

Type A *Forced system models*:  $F$  is independent of  $y$ , so  $F = F(t)$

Type B *Fluidelastic system models*:  $F = F(y(t), t)$  and dependence in  $y$  may include all time derivatives

Type C *Coupled system models*: the force  $F$  depends on something related to the wake, say  $q$ , so  $F = F(q(t), t)$  and  $q = G(y(t), t)$

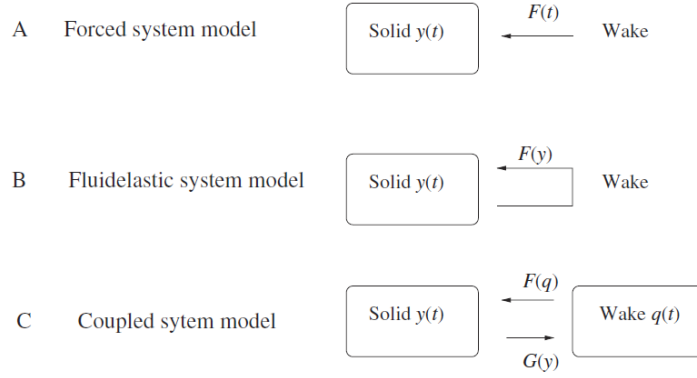


Figure 3.17: Classification of VIV models

Without going into too much detail, according to the formulations of type A and B, the fluid force is given as a function of time, for instance in the simplest formulation (Type A) in Eq.3.21:

$$F = F(t) = \frac{1}{2}\rho U^2 D C_L \sin\left(2\pi S t \frac{U}{D}\right) \quad (3.21)$$

Or it could be function of the amplitude ratio through  $C_L$ , as in fluid-elastic by Blevins [6] in Eq.3.22:

$$F = F(t) = \frac{1}{2}\rho U^2 D C_L \left(\frac{A}{D}\right) \sin\left(2\pi S t \frac{U}{D}\right) \quad (3.22)$$

where the dependency of  $C_L$  on amplitude ratio is straightforwardly a polynomial fit:

$$C_L \left(\frac{A}{D}\right) = C_L^0 + \alpha \left(\frac{A}{D}\right) + \beta \left(\frac{A}{D}\right)^2 \quad (3.23)$$

Lastly it could be a combination of amplitude and time, say frequency, for example Sarpkaya [22]:

$$F \left(\frac{A}{D}, U_r, t\right) = \frac{1}{2}\rho U^2 D \left[ \bar{C}_L \cos \phi \left(\frac{A}{D}, U_r \sin \omega t\right) - \bar{C}_L \sin \phi \left(\frac{A}{D}, U_r \cos \omega t\right) \right] \quad (3.24)$$

where  $\bar{C}_L$  is the amplitude an harmonic-assumed lift with phase  $\phi$ .

These types of modeling do not take into account the physics of wakes, while, on the contrary, forces in VIVs are the outcomes of wake dynamics, whose follows specific rules. According to this limitation formulation of Type C arise since the pioneering

work of Hartlen & Currie [12]. First example of so-called **wake oscillator** models, Hartlen & Currie introduced a *wake variable* as being the lift coefficient.

$$q(t) = C_L(t) \quad \Rightarrow \quad F(q(t), t) = \frac{1}{2} \rho U^2 D q(t) \quad (3.25)$$

The wake's dynamics  $q$  is governed by a Rayleigh equation:

$$W(q) = \ddot{q} - a\dot{q} + b\dot{q}^3 + \omega^2 q = 0 \quad (3.26)$$

In the *W-equation* 3.26 coefficients  $a$  and  $b$  are positive:

1. the term  $-a\dot{q}$  allows to represent the oscillating wake as a result from *self-sustained* flow instability at frequency  $\omega$
2. this instability is *self-limited* by the cubic term  $b\dot{q}^3$

Defined the wake dynamics, the only thing missing is the effect of body's motion on the wake, so looking at the Fig.3.17, the function  $G$ .

For the record, Hartlen & Currie assumed "rather arbitrarily" (it is a literal quote) the proportionality of  $G$  to cylinder's velocity  $G = c\dot{y}$ . The same assumption can be done for displacement  $y$  and acceleration  $\ddot{y}$  and it's discussed in Facchinetti & al [10].



## Chapter 4

# Numerical model and analysis

In this chapter numerical model and reasons why it has been chosen are presented. Firstly the wake oscillator model is described and a parametric analysis is carried out in order to estimate a performing set of parameters to design a feasible water everygy harvester.

Concerning the model it is necessary a calibration due to some model's parameters without a physical meaning.

Finally it follows a dimensional analysis and the results in terms of energy performance.

### 4.1 Wake oscillator model

Even if in recent years the computational power available increased making possible the CFD analysis of phenomena like VIV, low order methods are still more feasible in terms of computing time, say costs, at least in a preliminary approximation.

Wake oscillator models are a kind of such these, born of pioneering work by Hartlen & Currie [12] they describe the wake dynamics considering the feedback between fluid and structure.

Considering the scheme in Fig.4.1: The 1DoF scheme proposed by Facchinetti & al. [10] considers an elastically mounted rigid cylinder of diameter  $D$ , forced to bob up transversely to a stationary and uniform flow of free stream velocity  $U$ . A linear oscillator describes the structure:

$$m\ddot{Y} + c\dot{Y} + kY = F \quad (4.1)$$

where over-dot ( $\dot{\cdot}$ ) states the derivative with respect to the dimensional time  $T$ . As said, mass  $m$  takes into account the sum of the structure's mass  $m_s$  and the

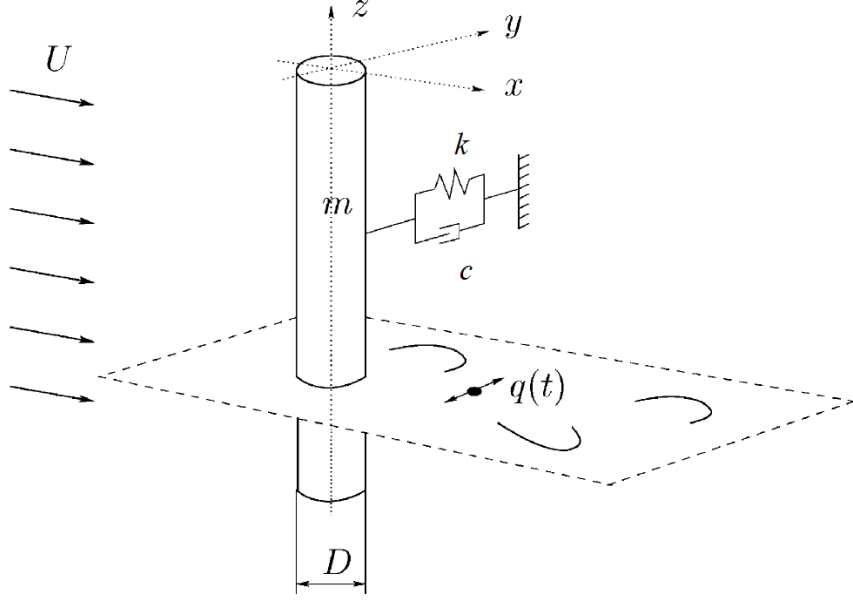


Figure 4.1: 1DoF model of coupled structure and wake oscillator

fluid-added one  $m_a$ , from which the dimensionless mass ratio is defined:

$$m = m_s + m_f, \quad m_a = C_A \rho D^2 \pi / 4, \quad m^* = (m_s + m_a) / \rho D^2 \quad (4.2)$$

The structure's equation 4.1 sees a linear damping  $c$  that models both viscous dissipation in the supports, henceforth structural damping  $c_s$ , and a fluid-added damping  $c_f$ :

$$c = c_s + c_f, \quad c_f = \gamma \Omega \rho D^2 \quad (4.3)$$

where the variable  $\gamma$  is a *stall parameter* discussed by Skop & Balasubramanian [25] in their reexamination of non-linear oscillator models. Stall parameter is nominally a function of oscillation amplitude through the drag coefficient  $C_D$ , and of Strouhal number, but here assumed as a constant. All mass, damping and stiffness are defined per unit length. In the case of cross-flow considered  $\Omega$  is the frequency of vortex shedding.

$$\gamma = \frac{C_D}{4\pi St}, \quad \Omega = \Omega_f = 2\pi St \frac{U}{D} \quad (4.4)$$

In order to conduct a forthcoming dimensionless set of equations, structural angular frequency  $\Omega_s = \sqrt{k/(m)}$  and structure reduced damping  $\zeta = c_s/(2m\Omega_s)$  are defined:

$$\ddot{Y} + \left( 2\zeta\Omega_s + \frac{\gamma}{m^*}\Omega_s \right) \dot{Y} + \Omega_s^2 Y = \frac{F}{m} \quad (4.5)$$

Last Eq.4.5 governs the structure describing it as a linear oscillator. There remains the wake dynamics and it is modeled by a wake oscillator as explained in the

previous chapter. The oscillations of vortex shedding is modeled by a non-linear oscillator and instead of the Rayleigh  $W$ -equation 3.26, the **van der Pol equation** is used:

$$\ddot{q} + \varepsilon\Omega_f(q^2 - 1)\dot{q} + \Omega_f^2 q = F' \quad (4.6)$$

henceforth called wake oscillator equation.  $q$  is a dimensionless variable without an explicit physical meaning, but pertinent to the fluctuating lift coefficient of the cylinder (Hartlen and Currie [12]), or it may be associated to a weighted average of the transverse component of the flow (Blevins [6]), or lastly assumed to be proportional to the transverse velocity of a near wake fluid mass (Krenk and Jielsen [15]). The RHS  $F'$  models the effects of the structure motion on the near wake. Referring to Rayleigh equation 3.26, here, the viscous term  $\varepsilon\Omega_f(q^2 - 1)\dot{q}$  confirms the capability of modeling a self-sustainable and stable oscillation of finite amplitude at frequency  $\Omega_f$ . Finally, introducing the dimensionless time  $t = T\Omega_f$ , that is the time scale from  $T$  to the *wake-based time scale*  $t$ , and the analogous displacement  $y = Y/D$  the **coupled fluid-structure dynamical system** is reached:

$$\begin{cases} \dot{y} + \left(2\zeta\delta + \frac{\gamma}{m^*}\right)\dot{y} + \delta^2 y = f \\ \ddot{q} + \varepsilon(q^2 - 1)\dot{q} + q = f' \end{cases} \quad (4.7)$$

where  $\delta$  is the reduced angular frequency of the structure:

$$\delta = \frac{\Omega_s}{2\pi St(U/D)} = \frac{1}{StU_r} \quad \text{with} \quad St = \frac{f_s D}{U} \quad \text{and} \quad U_r = \frac{2\pi U}{\Omega_s D} \quad (4.8)$$

The term  $f$  represents the action of the fluid in near wake on the cylinder and is commonly treated as a oscillating lift force; in dimensional terms:

$$F = \frac{1}{2}\rho U^2 D C_L \quad (4.9)$$

Note that lift coefficient  $C_L$  takes into account the forcing caused by the only vorticity in the wake and not the total instantaneous lift on structure. Following the prevailing notation is VIV's literature  $C_L$  is the vortex lift coefficient and  $C_{L_0}$  the observed lift coefficient on a fixed structure subjected to vortex shedding. In this sense, wake variable  $q$  is interpreted as a reduced vortex lift coefficient  $q = 2C_L/C_{L_0}$  so the ratio  $q/2$  represents the magnification with respect to a fixed structure under vortex shedding flow.

In dimensionless form, the oscillating lift force becomes:

$$f = Mq \quad \text{where} \quad M = \frac{C_{L_0}}{2} \frac{1}{8\pi^2 St^2 m^*} \quad (4.10)$$

Since  $M$  depends on mass ratio  $m^*$ , it is fundamentally a mass parameter that scales the effect of wake on structure.



An important step is the relation between the RHS term of wake oscillator and the equation on motion in  $y$ , that means the **fluid-structure coupling**.

$f' = Ay$  *displacement coupling* was the first considered and "rather arbitrarily" chosen by Hartlen & Currie [12]

$f' = A\dot{y}$  *velocity coupling* was suggested starting from energy considerations

$f' = A\ddot{y}$  *acceleration coupling* proposed by Facchinetti & al. was chosen in order to consider a linear inertial effect of the structure on the fluid

In this model the acceleration coupling is considered.

So set of equations 4.7 becomes:

$$\begin{cases} \dot{y} + \left(2\zeta\delta + \frac{\gamma}{m^*}\right)\dot{y} + \delta^2 y = Mq \\ \ddot{q} + \varepsilon(q^2 - 1)\dot{q} + q = A\ddot{y} \end{cases} \quad (4.11)$$

Where:

$$\gamma = \frac{C_{D0}}{4\pi St} \sqrt{1 + (2\pi St \dot{y})^2} \quad (4.12)$$

$$M = \frac{C_{L0}}{2} \frac{1}{8\pi^2 St^2 m^*} \sqrt{1 + (2\pi St \dot{y})^2} \quad (4.13)$$

Almost all the parameters in the set of equations governing 1 DoF VIVs are Reynolds dependent. In this first analysis a dimensionless investigation is conducted in order to evaluate amplitude ratios and energy performance parameters.

### 4.1.1 Tuning parameters

The van der Pol equation contains two semi-empirical parameter,  $\varepsilon$  and  $A$ , respectively named *cross-flow fluid damping parameter* and *coupling coefficient in cross-flow direction*. These coefficients do not have a physical meaning and they must be tuned on experimental data.

For such reason, a tuning analysis has been conducted. The baseline experiment is the one handled by Khalak & Williamson [13] on fluid forces and dynamics of an elastically mounted rigid cylinder, constrained to oscillate along transverse direction with respect to the free stream, data are shown in Fig.4.2. Since the fluid in question is water the experiment's system has a very low mass ratio, circa 1% of the value used in the experiments by Feng [11]. The experimental setup consists of an air-bearing facility atop the water channel, a 2-axis force balance with LVTDs measures lift and drag simultaneously through measurements of displacements.

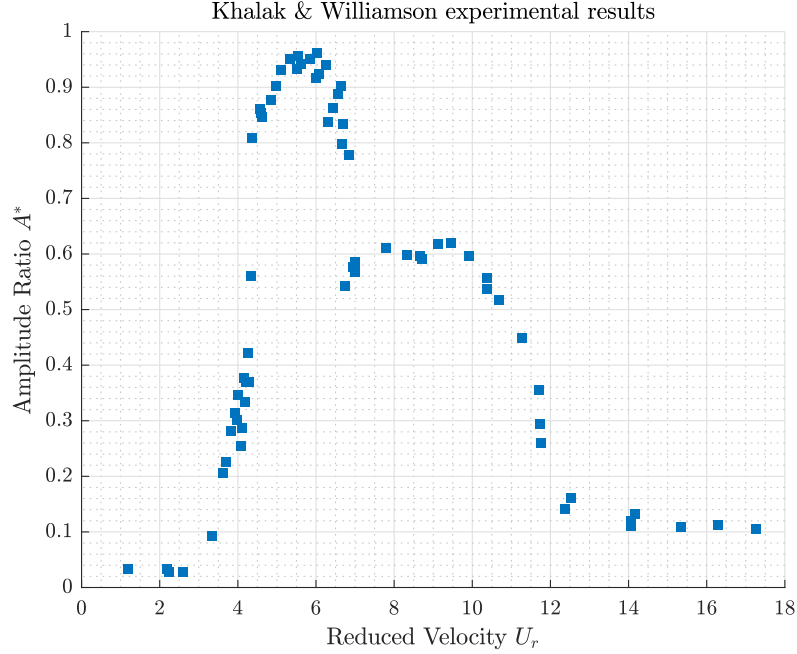


Figure 4.2: Khalak &amp; Williamson experimental data (1997) [13]

Description	Symbol	Values
Drag Coefficient	$C_{D_0}$	1.1856
Lift Coefficient	$C_{L_0}$	0.3842
Mass Ratio	$m^*$	2.36
Damping Ratio	$\zeta$	0.0045
Fluid Damping Parameter	$\varepsilon$	0.001 up to 1.05
Coupling Coefficient	$A$	1 up to 20

Table 4.1: Values of tuning analysis

Values of drag and lift coefficients have been found by CFD analysis at high Reynolds, as will be discussed in next chapter. The non linear feature passing from Upper Branch to the Lower is reflected by the need to define two values for both  $\varepsilon$  and  $A$  and the threshold of reduced velocity that set the boundary between Upper and Lower, named UB and LB.

Several attempts are then made to match experimental data in Fig.4.2 with the system of equation 4.11 varying  $\varepsilon$  and  $A$  between values in Tab.4.1.1. Since the different behavior of VIVs in Upper and Lower branches it was needed to impose two different sets of values of semi-empirical parameters. Literature is unclear about a rigorous threshold between UB and LB in terms of reduced velocity, this limit value is here named  $U_{r_{th}}$ . Figure 4.3 below shows different values of the limit of

reduced velocity on equal terms of all the other parameters.

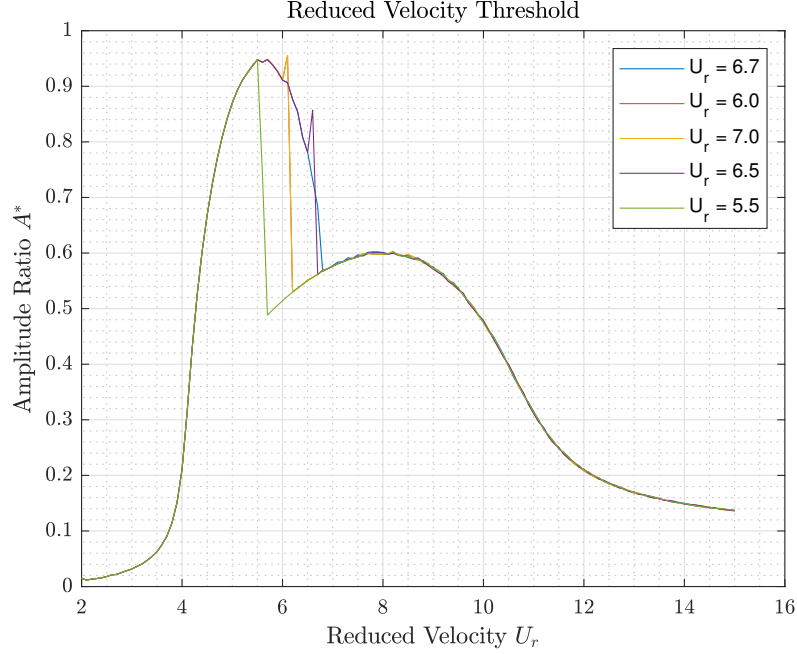
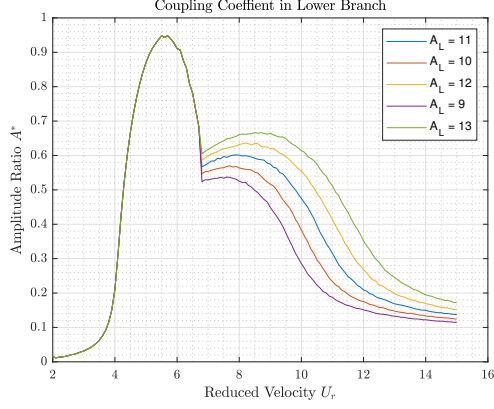


Figure 4.3: Effect of threshold of reduced velocity which separates Upper Branch from Lower

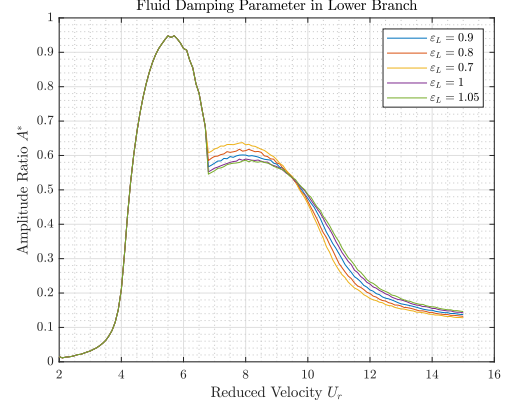
With the respect to tests in Fig.4.3 the limit value of  $U_r = 6.7$  has been chosen. The effects of semi-empirical parameters is interdependent, even if in general the fluid damping parameter  $\varepsilon$  raises the amplitude curve decreasing its values in the Upper branch, while there is a shift towards higher values of reduced velocity in the Lower branch. Coupling coefficient  $A$  lifts the curve increasing in the UB while in Lower branch the curves are shifted towards and upwards. The effects are summarized in figures below 4.8. This said, the various tuning tests conducted, such as the few reported in Fig.4.9, have led to results below in Tab.4.1.1.

	Upper Branch	Lower Branch
$U_r$	$< 6.75$	$> 6.75$
$A$	11	4
$\varepsilon$	0.9	0.05

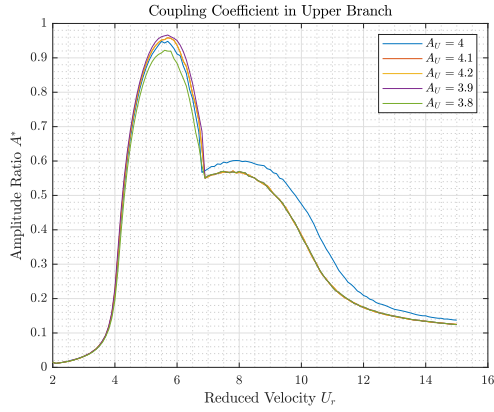
Table 4.2: Values of semi-empirical parameters in tuning analysis



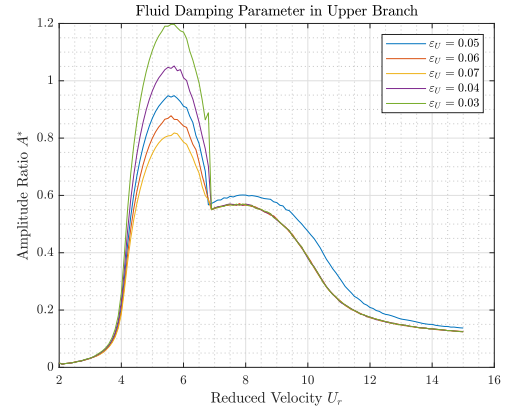
(a)  $A$  in LB



(b)  $\varepsilon$  in LB



(c)  $A$  in UB



(d)  $\varepsilon$  in UB

Figure 4.8: Dependency of semi-empirical parameters  $A$  and  $\varepsilon$  on amplitude ratio - reduced velocity chart.

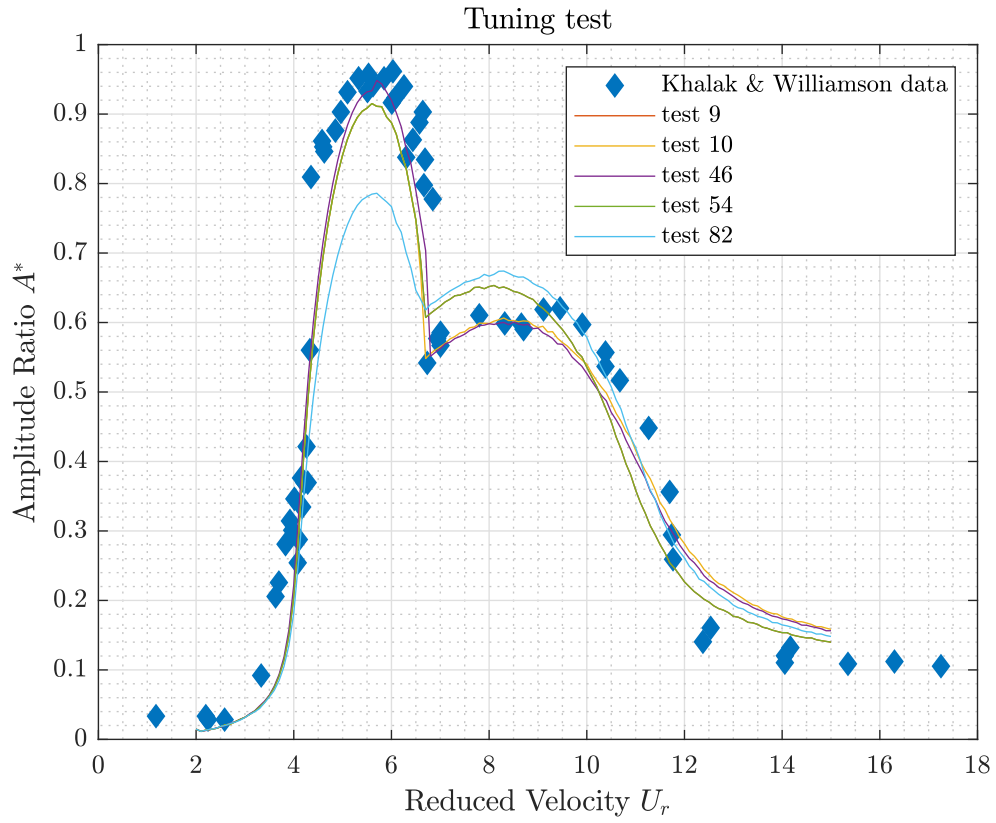


Figure 4.9: Some of tests conducted in order to calibrate model on Khalak & Williamson experimental data at very low mass ratio

## 4.2 Numerical solution procedure

The solution of governing non-linear coupled equation 4.11 is conducted and found through a 4th order Runge Kutta scheme for values of reduced velocity from 2 to 15.

$$\begin{aligned}
 \dot{x} &= f(t, x) \quad x(t_0) = x_0 \\
 \text{Considered a step size} \quad h &= \Delta t \\
 \text{And defined} \quad x_{n+1} &= x_n + \frac{1}{6}(k_1 + 2k_2 + 2k_3 + k_4) \\
 t_{n+1} &= t_n + \Delta t \\
 \text{For the n steps:} \quad k_1 &= \Delta t f(t_n, x_n) \\
 k_2 &= \Delta t f\left(t_n + \frac{\Delta t}{2}, x_n + \frac{k_1}{2}\right) \\
 k_3 &= \Delta t f\left(t_n + \frac{\Delta t}{2}, x_n + \frac{k_2}{2}\right) \\
 k_4 &= \Delta t f(t_n + \Delta t, x_n + k_3)
 \end{aligned}$$

where, in this case,  $x$  is the vector state  $[y \dot{y} q \dot{q}]$ .

The integration in time is handled for a total of 100 s and a time step of 0.1 s. Initial condition per  $t = 0$  are in Tab.4.2 below:

$y_0$	$\dot{y}_0$	$\ddot{y}_0$	$q_0$	$\dot{q}_0$
0	0	0	2	0

Table 4.3: Initial condition for the first iteration

For each reduced velocity between 2 and 15 with a step-size of 0.1, maximum amplitude  $A_{max}$ , frequency response  $f$  and maximum value of wake variable  $q$  have been obtained.

## 4.3 Energy efficiency performances

Since this thesis considers VIVs for energy harvesting it is necessary to describe the evaluation procedure in terms of *efficiency of conversion*.

As introduced in the introductory chapter, in the paragraph concerning the Betz Limit, an option of performance estimation might be the ratio:

$$\eta = \frac{\text{absorbed energy}}{\text{available power of swept area}} = \frac{\frac{1}{T} \int_0^T c \dot{Y}^2 dT}{\frac{1}{2} \rho U^3 (2Y + D)L} \quad (4.14)$$

where, since the Power Take-Off (PTO) system is a linear generator, so the control law which regulates the absorbed power is proportional to the force, ie. the damping term of equation of motion multiplied by the velocity  $\dot{y}$ .

Altering the Eq.4.14 into a dimensionless form it becomes:

$$\eta = 4(2\pi)^3 \frac{m^* \zeta}{U_r^3 \delta^2} \frac{1}{2y+1} \frac{1}{t} \int_0^t \dot{y}^2 dt \quad (4.15)$$

where all the dimensionless parameters have been already defined in previous sections. Integrals in preceding equation are numerically obtained through a 1st order closed Newton-Cotes over five complete oscillation so obtaining an averaged value.

## 4.4 Dimensionless analysis and results

In this section the dimensionless analysis' results are reported in terms of amplitude ratio  $A^*$  and conversion efficiency  $\eta$  in Eq.4.15.

A first point to note is the effect of damping ratio  $\zeta$ . As shown in figures, regardless of mass ratio, at very low damping, the system's feedback returns surely an highest amplitude, but a low conversion efficiency, since  $\zeta$  appears to the numerator of Eq.4.15 in the mass-damping parameter. As reported in figures, in case of very low damping, the energy extracted from fluid and converted into electricity is small, so efficiency drops down. However in the occurrence of high damping it suppresses the VIV resulting in zero harnessed energy. As result, seems to exist an optimum value of damping ratio in order to obtain a maximum efficiency of conversion for every mass ratio.

More than one value of reduced mass is presented in following figures, and each  $m^*$  is shown varying damping  $\zeta$  from the lowest value in literature to the highest.

The first figures plot the amplitude ratio or normalized semi-amplitude versus the reduced velocity for various values of mass ratio at same damping ratio  $\zeta$ .

$m^*$	1.5	2	2.36	2.5	3
$\zeta$	0.0045	0.0184	0.0322	0.0461	0.0600
	0.0738	0.0877	0.1016	0.1154	0.1293
	0.1432	0.1571	0.1709	0.1848	0.1987
	0.2125	0.2264	0.2403	0.2541	0.2680

Table 4.4: Mass ratio and damping values for the dimensionless analysis

Figures 4.10,4.11,4.12, 4.13 and 4.14 prove that the amplitude response decreases in absolute terms increasing mass ratio, that is consistent with the VIV's dynamics as exposed in the theory chapter. Considering, for example, the first value of damping  $\zeta = 0.0045$ , the trend of max amplitude ratio versus mass ratio is show in Fig.4.15. The next charts Figs.4.16,4.17, 4.18,4.19 and 4.20 propose the amplitude ratio versus five values in Tab.4.4, of damping factor  $\zeta$  for each mass ratio.

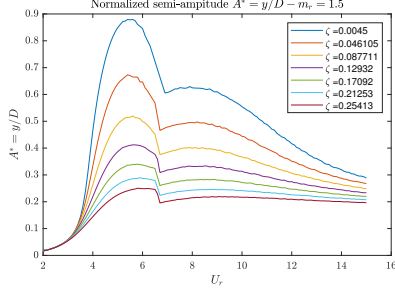


Figure 4.10:  $A^*$  for  $m^* = 1.5$

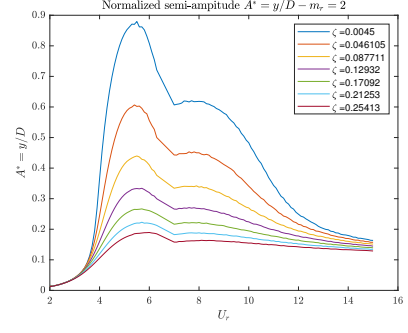


Figure 4.11:  $A^*$  for  $m^* = 2$

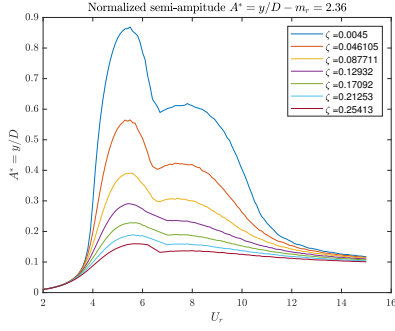


Figure 4.12:  $A^*$  for  $m^* = 2.36$

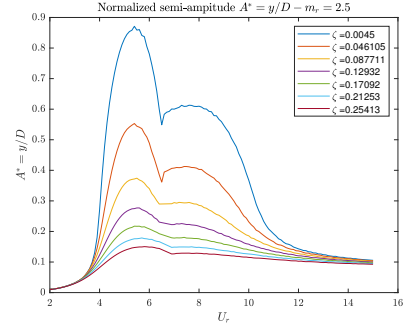


Figure 4.13:  $A^*$  for  $m^* = 2.5$

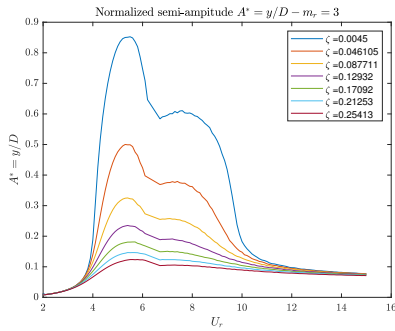


Figure 4.14:  $A^*$  for  $m^* = 3$

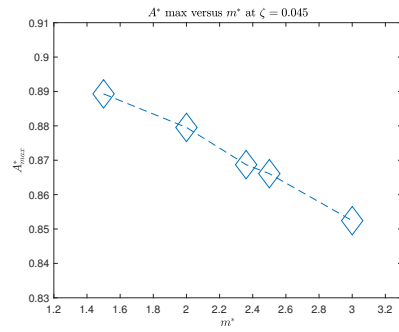


Figure 4.15: Trend of max amplitude ratio versus mass ratio for  $\zeta = 0.0045$



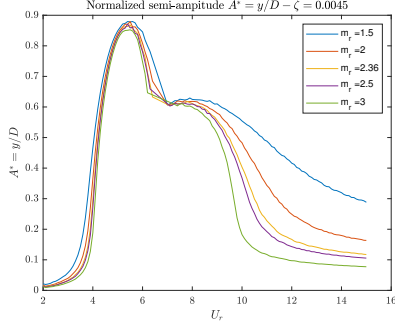


Figure 4.16:  $A^*$  for  $\zeta = 0.0045$

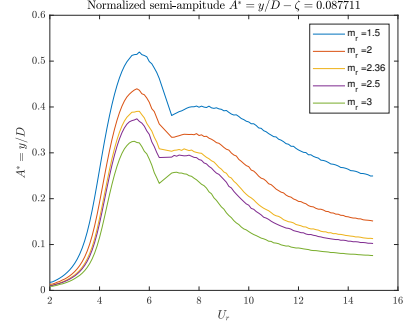


Figure 4.17:  $A^*$  for  $\zeta = 0.0877$

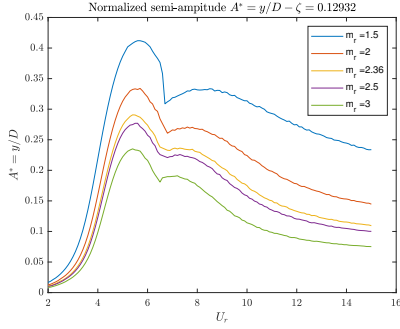


Figure 4.18:  $A^*$  for  $\zeta = 0.1293$

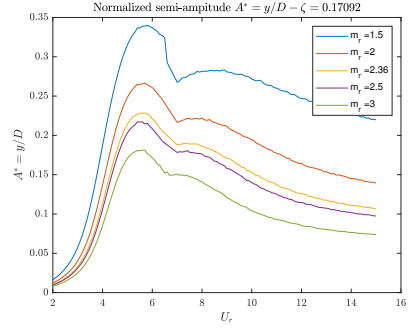


Figure 4.19:  $A^*$  for  $\zeta = 0.1709$

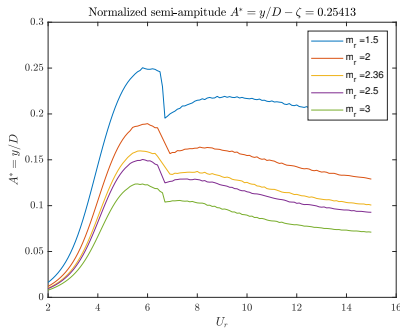


Figure 4.20:  $A^*$  for  $\zeta = 0.2541$

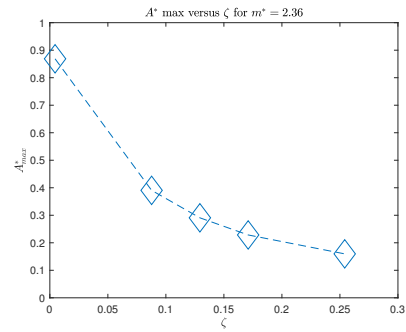


Figure 4.21: Trend of max amplitude ratio versus damping for  $m^* = 2.36$

Larger the value of mass ratio, more extended is the range in which amplitudes are consistent, as already outlined in theory chapter and here highlighted, for instance, by Fig.4.10 where  $A^*$  for the lowest value of mass ratio is shown. Another in physics consistent outcome is what emerges from Fig.4.15 where amplitude ratio decreases increasing mass ratio.

From a damping point of view figures from 4.16 to 4.20 unveil an increasing dependence of system's response increasing the value of damping. In fact for low  $\zeta$ , according to plot of  $A^*$  for  $\zeta = 0.0045$  in Fig.4.16 there is quite no impact due to mass ratio, while increasing the damping value the curves move away from each other and, in absolute terms, the amplitude decreases because the system is more damped.

Once all cases considered have been assessed in the previous figures, follows the observations on maximum values of efficiency  $\eta$ . The plot on Fig.4.22 shows that the maximum of energy conversion efficiency  $\eta$  is quite not afflicted by the damping ratio, in absolute terms is more or less equal for each value of mass ratio, about 6.5%, just shifted forward towards higher value of damping factor.

Maybe the most important and crucial feature of dimensionless analysis is consists of the expression of maximum conversion efficiency as a function of mass-damping. The chart in Fig.4.23 clearly demonstrates a collapse of maximum  $\eta$  around  $m^*\zeta \cong 0.2$ , coherently with the value found by Barrero & Gil in [3].

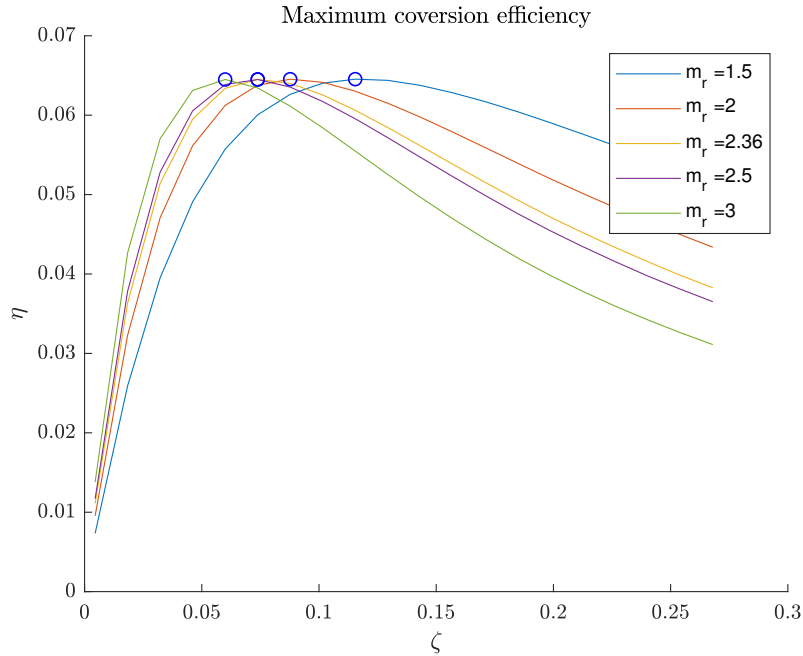


Figure 4.22: Maximum efficiency  $\eta$  versus damping factor  $\zeta$  for each mass ratio  $m^*$

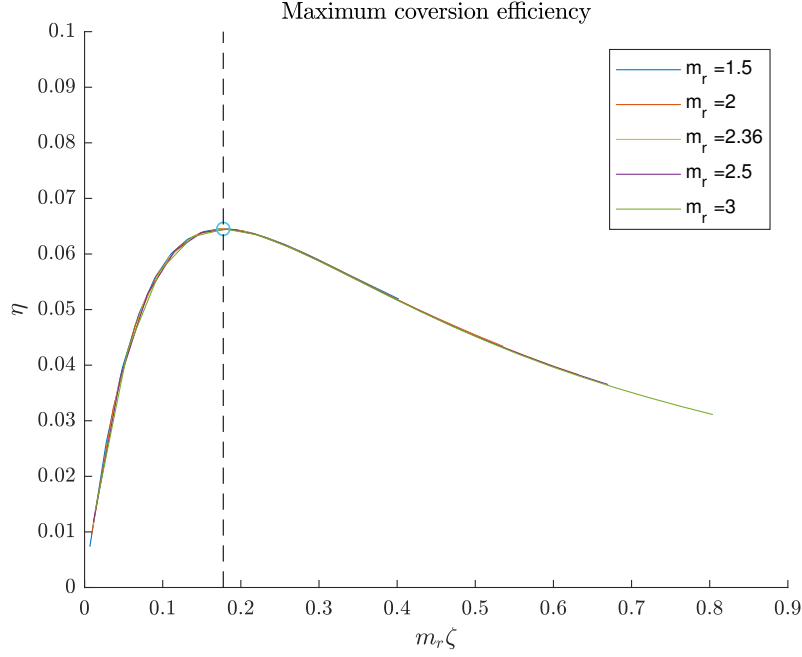


Figure 4.23: Maximum efficiency of conversion versus mass-damping parameter  $m^* \zeta$

## 4.5 Dimensional parameters design

In the scope of energy harvesting through VIVs, about reduced mass, "less is more" (to paraphrase a famous motto). A low value of  $m^*$  is easily achievable in case of water as energy carrier, since is more dense than air.

According to the previous dimensionless analysis a reduced mass  $m^* = 2.5$  has been chosen. The maximum value of efficiency of conversion is obtained for a mass-damping parameter equal to  $m^* \zeta$  so damping ratio is given.

The next step in dimensional design is to determine diameter  $D$  and natural frequency of the structure  $f_n$  through the selection of the reduced velocity on-design. As reported in theory paragraphs a VIV-based system is able to catch the bulk of energy in the synchronization range, in particular close to the condition of resonance, here corresponding to  $U_r = 5.2$  that is the on-design reduced velocity.

Initially amplitude and efficiency are summarized in Figs.4.24 and 4.25.

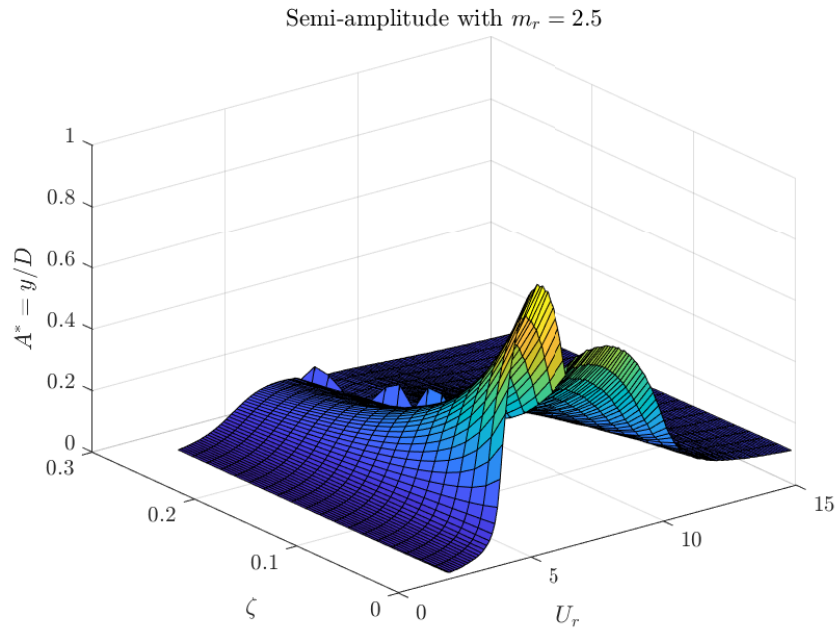


Figure 4.24: 3D plot of  $A^*$  for  $m^* = 2.5$

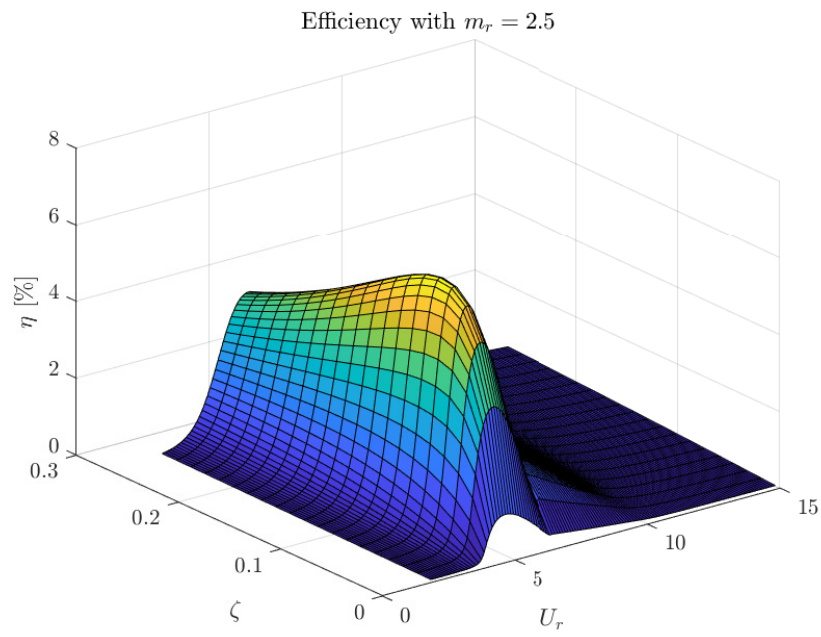


Figure 4.25: 3D plot of  $\eta$  for  $m^* = 2.5$

### 4.5.1 Case study

In this section the case study of Pantelleria is presented with the aim of identifying the design current velocity for the VIVs-based energy harvester.

Data collected and exposed concern the system AWAC (Acoustic Doppler Wave & Current Profiler, in Fig.4.27), an hydroacoustic current meter placed in the island of Pantelleria as shown in Fig.4.26, at coordinates GPS (DMS)  $36^{\circ} 49' 54''$  N,  $11^{\circ} 55' 13''$  E.

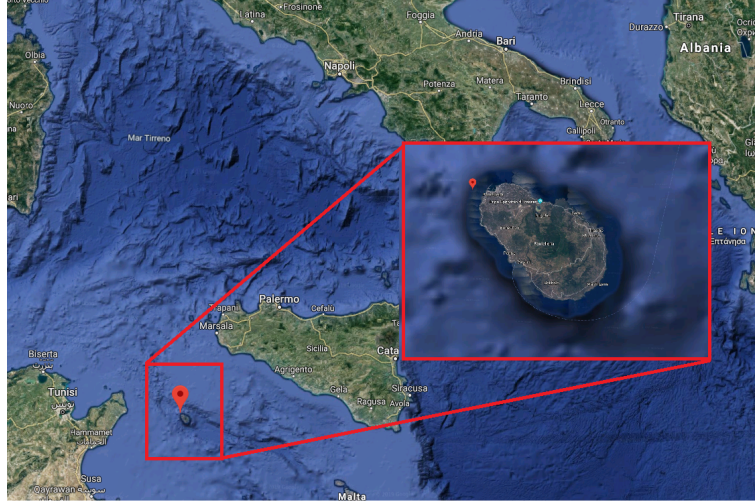


Figure 4.26: AWAC position in the island of Pantelleria

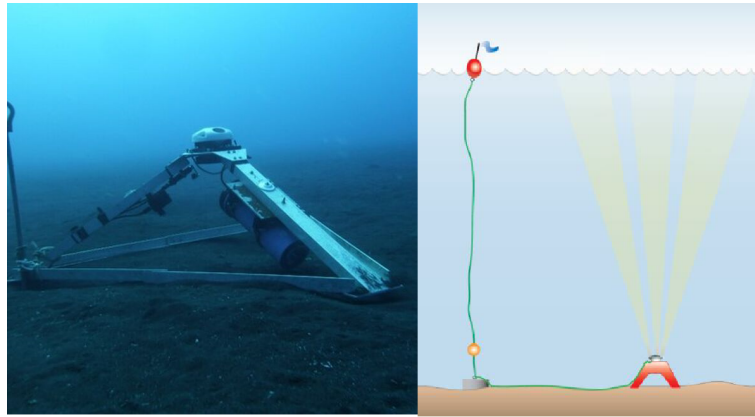


Figure 4.27: AWAC system

Starting from raw data, supplied by kind permission of ISWEC research team, a post-processing has been conducted to analyze the site in terms of current speed. The best practice about the evaluation of wind and sea site is to organize data into

charts and histograms containing respectively the current speed and its direction during the observed period. Measures refer to the maximum current speed at  $2.5m$  below the water line. Both of diagrams are separately shown in Figs.4.28 and 4.29.

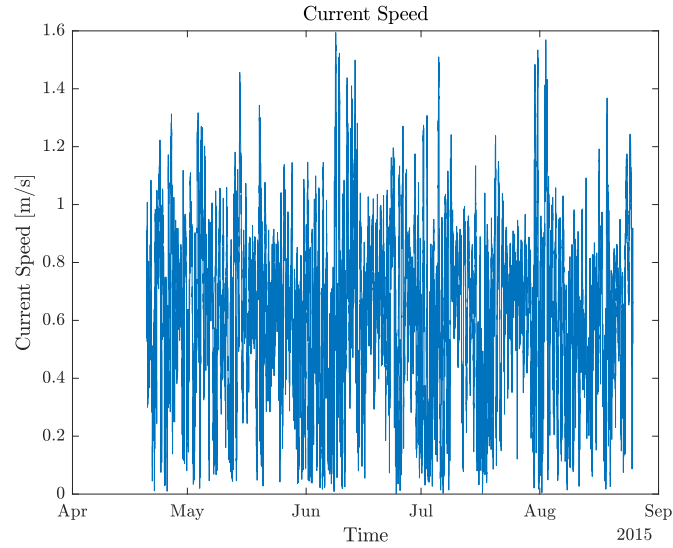


Figure 4.28: Sea-current speed

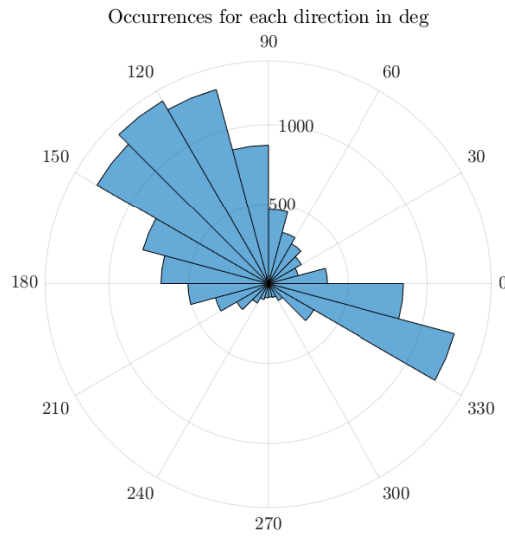


Figure 4.29: Sea-current direction occurrences

Next step is the evaluation of the sea-current distribution and a statistical probability analysis. The current speed distribution is thus replaced by a Weibull distribution, as usually done in weather forecasting. It consist in a continuous probability distribution in which the random variable  $x$  is function of two parameters, in this case both equal to 1:

$$f(x|\lambda, k) = \begin{cases} \frac{k}{\lambda} \left(\frac{x}{\lambda}\right)^{k-1} e^{-x/\lambda^k} & x \geq 0 \\ 0 & x < 0 \end{cases} \quad (4.16)$$

Results of probability analysis are reported in Fig.4.30.

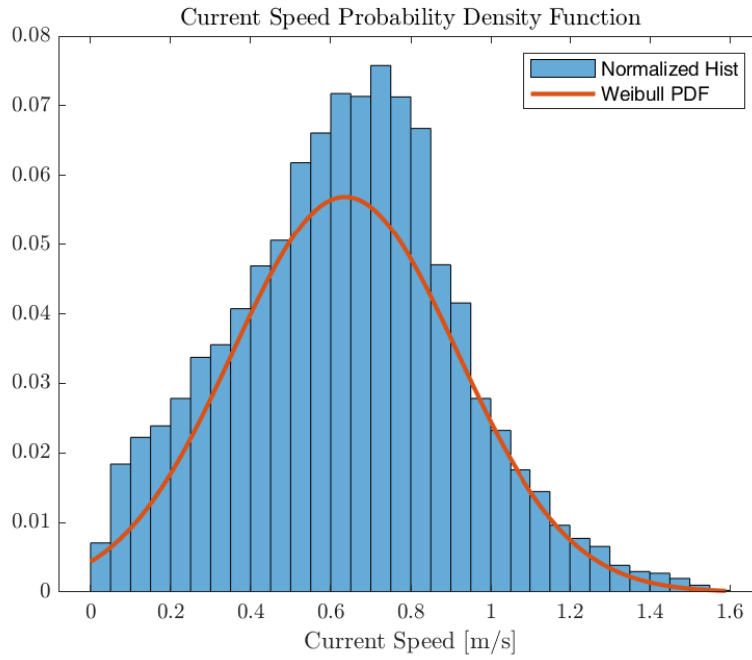


Figure 4.30: Sea-current probability and Weibull PDF

Finally it is possible to evaluate a design speed  $U = 0.57 \text{ m/s}$  that represents the most probable value during the sampled period. Once the design speed is defined, the natural frequency multiplied by diameter  $D$  is given by definition of reduced speed:

$$f_n D = \frac{U_{design}}{U_r} \quad (4.17)$$

For small values of diameter of the cylinder it is expected a small amount of power due to the smaller swept area, but an higher value of power density compared with an bigger cylinder. Since designer assigns the diameter  $D$  it is possible to evaluate total mass  $m$  of a hollow cylinder with thickness  $t_c$ , frequency from previous

equation and therefore the optimal value of stiffness:

$$m = m_s + m_a = \pi D^2 \left( \frac{t_c}{D} \rho_m + \frac{1}{4} \rho_w \right) \quad (4.18)$$

$$f_n = \frac{U_{design}}{U_r D} \quad (4.19)$$

$$k_{opt} = \omega_n^2 m L = (2\pi f_n)^2 m L \quad (4.20)$$

where  $\rho_m$  is the density of cylinder's material,  $\rho_w$  density of seawater,  $U$  is the design current speed,  $L$  is the cylinder's length. The calculation of damping factor is done through the *optimal mass-damping*  $(m^*\zeta)_{opt}$ , ie. the value for which the efficiency is maximized, as found in Fig.4.21.

For each value diameter  $D$  as a free parameter from 0.01 to 0.17, this maximum value allows to dealing with moderate low aspect ratio  $L/D$ , and a step of 0.02, assuming a unit length, the amplitude response is computed and shown in Fig4.31. All the next charts plot the quantity under examination as function of the flow velocity:

$$U = U_{r_{opt}} f D \quad \text{where} \quad f = \frac{U_{design}}{U_{r_{opt}} D} \quad (4.21)$$

The quantity  $U_{r_{opt}}$  is the reduced velocity in correspondence of maximum efficiency  $\eta$ . It is obvious that a larger diameter provides to higher amplitude response. So, in order to achieve a better design, considerations and calculations about power are needed.

Starting from the definition of efficiency  $\eta$  in Eq.4.15, such efficiency represents the ratio between the power absorbed by the system and the one available from the fluid flow:

$$P_E = \eta P_A = \eta \frac{1}{2} \rho U^3 (2y + D) L \quad (4.22)$$

where the subscripts  $E$  and  $A$  are respectively *extracted* and *available*. Results are shown in Fig.4.32 below. Considering a mechanical damping, basically due to the friction of a gears-based system, equal to  $\zeta_m = 0.002$  with regards to similar structures in literature, it is possible to write the actual power converted into electricity:

$$P_{el} = \frac{\zeta - \zeta_m}{\zeta} \eta \frac{1}{2} \rho U^3 (2y + D) L \quad (4.23)$$

The outcomes in terms of the electrical power  $P_{el}$  are shown in Fig.4.23. Similar but opposite trends could be observed in terms of power density. Therefore two quantities are defined:

$$PD_{str} = \frac{\text{Power extracted}}{\text{Stroke}} \quad (4.24)$$

$$PD_{surf} = \frac{\text{Power extracted}}{\text{Swept area}} \quad (4.25)$$



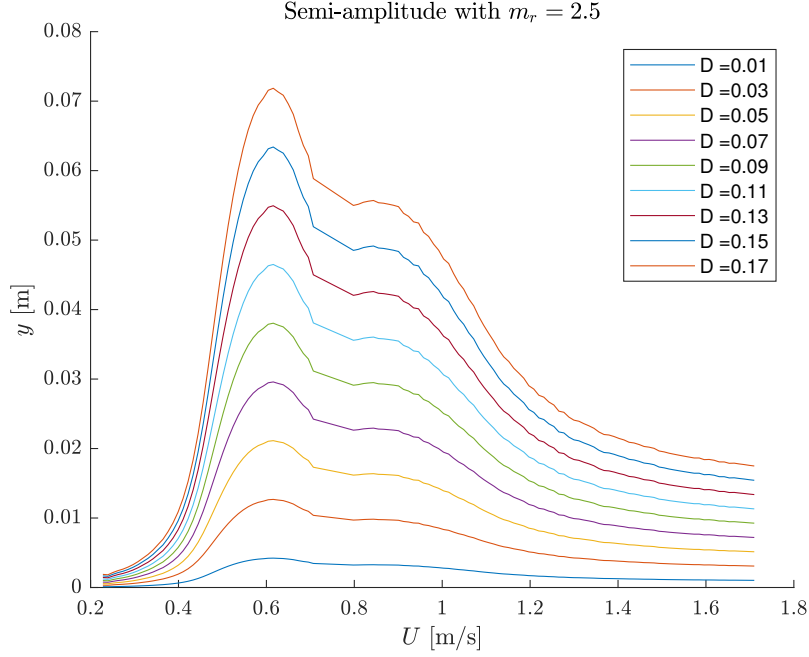


Figure 4.31: Amplitude response for each diameter  $D$  considered in the dimensional analysis and design

where  $\text{stroke} = 2y + D$  and the swept area is equal to  $\pi/4 \cdot \text{stroke}^2$ . Referring to these specifications the results are shown in figures below, Fig.4.34 and Fig.4.35.

## 4.6 Tuned system

To aim a full operative system a continuous control of stiffness and damping is thinkable. Such a regulation has to be made to keep the system in optimal range for every velocity, ie. having always:

$$U_r = U_{r_{opt}} \quad (4.26)$$

so the equation above are correct, considering the natural frequency as variable.

In such a case the power extracted increase increasing the flow speed  $U$ , so not following the typical bell-shape already seen since the theory chapter. Results are reported in Figs.4.36 and 4.37.

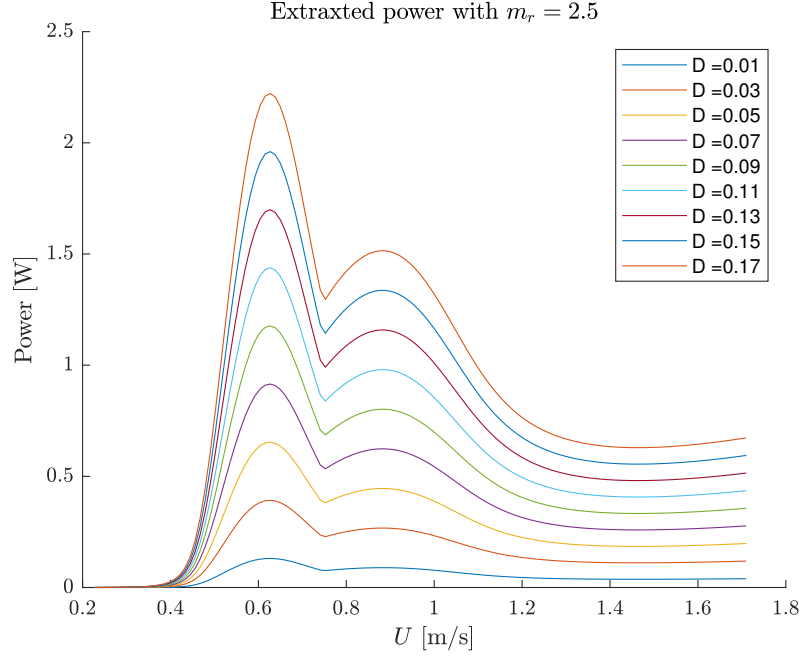


Figure 4.32: Power extracted before conversion to electrical power for each diameter

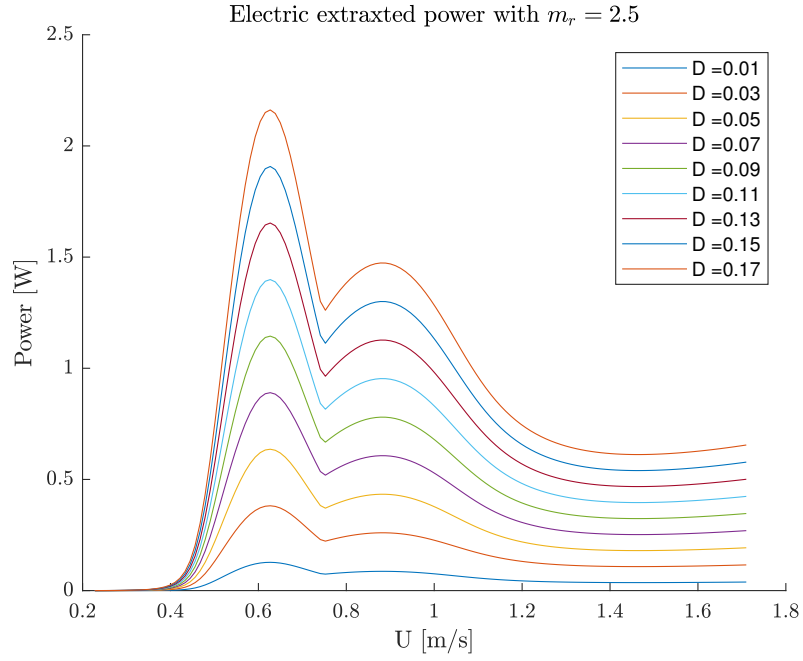


Figure 4.33: Electrical power extracted for each diameter

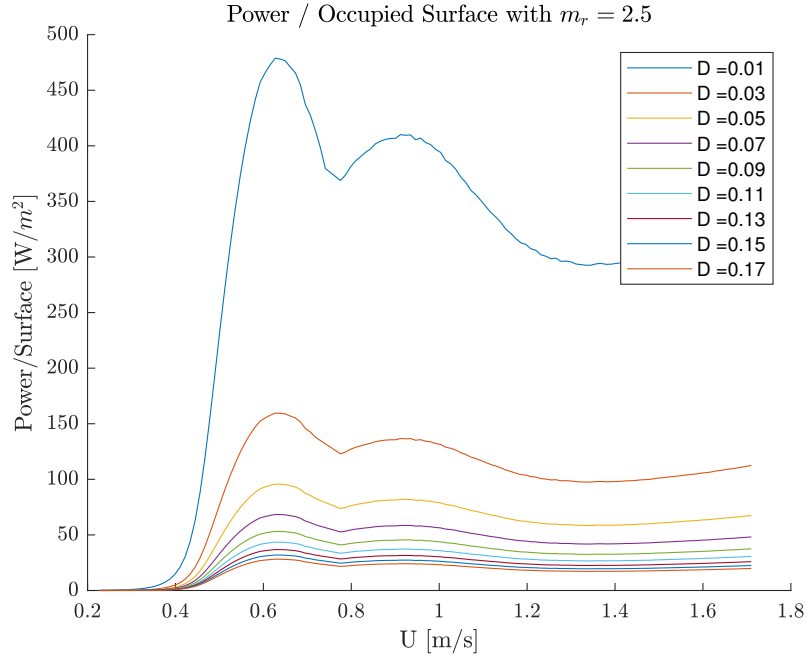


Figure 4.34: Power density referred to the stroke of cylinder

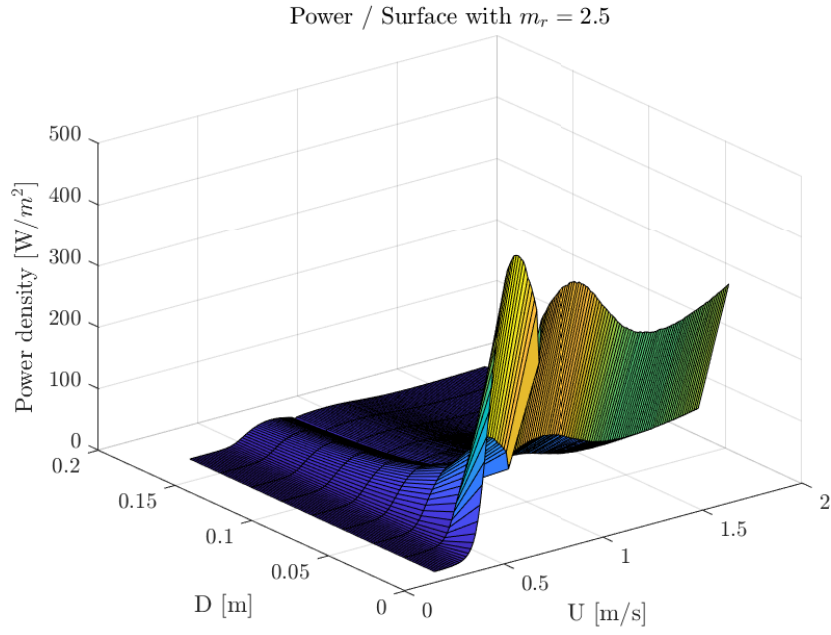


Figure 4.35: Power density referred to occupied surface

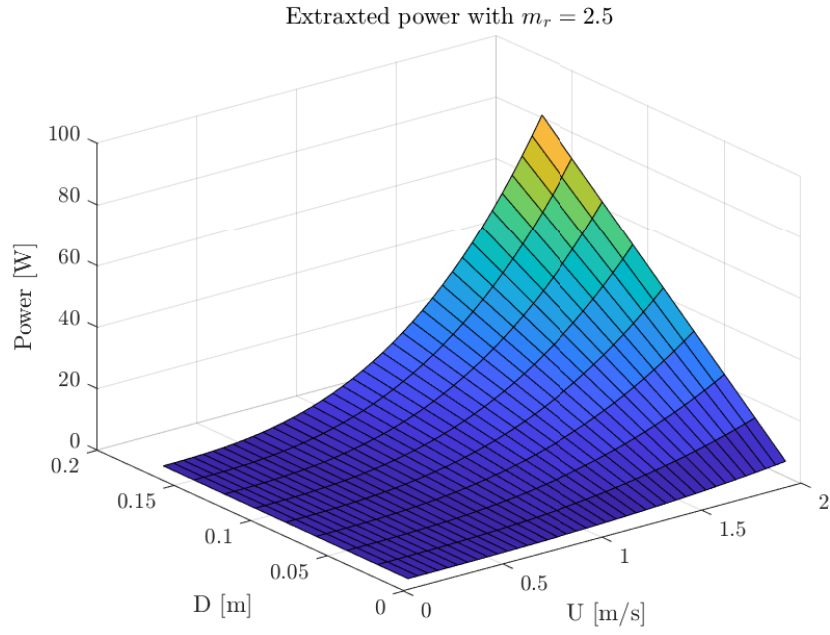


Figure 4.36: 3D plot of power extracted in tuned system for different diameters

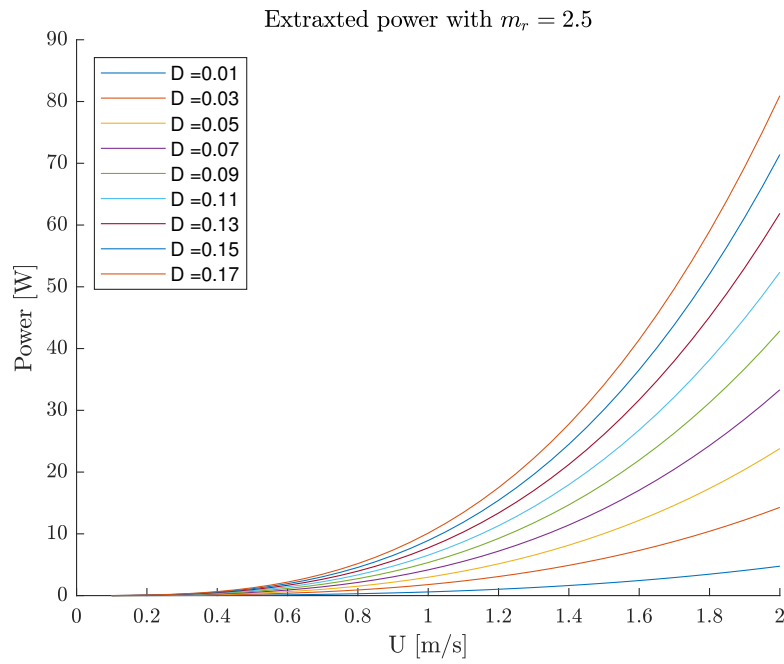


Figure 4.37: Power extracted in tuned system for different diameters



## Chapter 5

# Computational Fluid Dynamics analysis

Nowadays the comprehension of a fluid dynamics phenomenon cannot be achieved only through experiments, but thanks above all to the growth of computational power, simulations and numerical modeling are powerful tools both in academic and industrial scopes. Computational Fluid Dynamics, commonly abbreviated CFD, is a computer based approach born to analyze and solve problems where fluid flows are involved; it is also related to heat transfer and chemical reactions. Thus making clear that CFD cannot be considered as a replacement of experiments, rather experiments are necessary to tune numerical models.

That said, the advantages of CFD are quite evident:

- No capacity or model scale limits
- No instrumentation and facilities
- Unlimited detail level of results

The list could continue straightforwardly. On the other hand, the costs recovered from the absence of instruments and laboratories are replaced by computing tools, from a basic CPU to the High Performance Computing (HPC) solutions, both in terms of purchase and maintenance due to usage time. Furthermore, as said, CFD is not yet at the level where it can be blindly used without experimental-based tuning and despite the increasing speed of computation available (as established by the famous Moore Law) CFD has not yet matured to a level where it can be used for real time computation. Numerical analyses require significant time to be set up and performed.

Taking into account these pros and cons, CFD techniques are now essential to the achievement of fluid dynamics.

## 5.1 Methodology of CFD

In this section a brief introduction to CFD and its numerical method is presented, starting from the governing equation, through the methods used to obtain the solution of N-S equations, until the discretization aspects.

### 5.1.1 Governing equations

The CFD soul stated in a of mathematical equations and their solution in a numerical way. These equations are named Navier-Stokes equations and describe the motion of fluids in a macroscopic manner due to the hypothesis of continuum. Despite their physics meaning and engineering uses, they are of great interest in a purely mathematical sense: it has not yet been proven whether solutions always exist and, if they do exist, whether they are smooth, the reason why the CMI have included them in the Millennium Prize Problems.

**Continuity Equation** Starting from fundamental laws of Newtonian mechanics, which states the conservation of mass in an arbitrary material control volume varying in time and fixed in space, the first governing equation states:

$$\frac{\partial \rho}{\partial t} + \nabla \cdot (\rho \mathbf{u}) = 0 \quad (5.1)$$

or better, in Einstein notation:

$$\frac{\partial \rho}{\partial t} + \frac{\partial}{\partial x_i} [\rho u_i] = 0 \quad (5.2)$$

where  $\rho$  is the fluid density and  $u$  the velocity vector. For an incompressible fluid the change rate of density is nil so:

$$\nabla \cdot \mathbf{u} = 0 \quad (5.3)$$

**Momentum equations or Navier-Stokes equations** The second equation of governing set states the conservation of momentum, so is a sub-set of 3 equation in a 3D space with coordinates  $x, y, z$ . The conservation of momentum is a straightforward consequence of Newton's second Law, hence the balance between forces and mass time acceleration is applied for each fluid particle or, better, for a closed system, the total momentum will not change as long as there are no external forces. Defined the stresses  $p$  pressure, ie. a normal stress, and  $\tau$  the viscous stresses coming from Stokes relations and stress tensor, in Einstein notation:

$$\frac{\partial}{\partial t} (\rho u_i) + \frac{\partial}{\partial x_j} [\rho u_i u_j + p \delta_{ij} - \tau_{ji}] = 0 \quad (5.4)$$

For incompressible fluid, so  $\nabla \cdot \mathbf{u}$  is valid, under the acting of an external force, for instance gravity  $\mathbf{g}$ , equations 5.4 become:

$$\rho \frac{Du_i}{Dt} = -\nabla p + \rho \mathbf{g} + \mu \nabla^2 \mathbf{u} \quad (5.5)$$

where  $D/Dt$  is the material derivative in time,  $\mu$  is the dynamic viscosity of the fluid and  $\nabla^2 u_i$  the Laplasian of velocity vector component  $u_i$ . Many authors prefer to report another form of N-S equation for incompressible fluid, where incompressibility is better visualized by dividing for the density:

$$\frac{\partial \mathbf{u}}{\partial t} + (\mathbf{u} \cdot \nabla) \mathbf{u} - \nu \nabla^2 \mathbf{u} = -\frac{\nabla p}{\rho} + \mathbf{g} \quad (5.6)$$

where  $\nu$  is cinematic viscosity  $\mu/\rho$ .

**Energy Balance** Last equation consists in the simple physical principle that states the conservation of energy expressed by the First Principle of Thermodynamics. So the rate of change of total energy in a control volume is equal to the sum of net heat flux towards the control volume and the work done per unit time on the control volume by volumetric and surface forces. In a mathematical form:

$$\rho \frac{D}{Dt} \left( e + \frac{1}{2} |\mathbf{u}|^2 \right) = \rho \dot{\xi} - \nabla \cdot \dot{\mathbf{q}} - \nabla \cdot (p \cdot \mathbf{u}) + \nabla \cdot (\bar{\tau} \cdot \mathbf{u}) + \rho \mathbf{f} \cdot \mathbf{u} \quad (5.7)$$

where  $\dot{\xi}$  is the heat absorbed per unit time and unit mass,  $\dot{\mathbf{q}}$  is heat flux due to thermal conduction depends from the temperature gradients through the Fourier's law  $\dot{\mathbf{q}} = -k \nabla T$ ,  $e$  is the internal energy per unit mass.

**Closure of governing equations** The partial differential equations presented above have general meaning and are not a closed set. To provide closure it is needed to add equations to the mathematical models and depend on fluid material under consideration and the psysical phenomenon analyzed.

### 5.1.2 Discretization FVM

The fundamental of CFD capability is to transfrom the mathematical model into a system of algebric equations, this trasformation involves discretizing in space and time. There are fundametally three methods of discretization: finite difference method (FDM), finite element method (FEM) and finite volume method (FVM). The last one is here described. Every balance equations can be manipulated in terms of generic trasport equation which consists of four parts:

$$\underbrace{\frac{d}{dt} \int_V \rho \phi dV}_{\text{Transient term}} + \underbrace{\int_S \rho \mathbf{u} \phi \cdot d\mathbf{S}}_{\text{Convective term}} = \underbrace{\int_S \Gamma \nabla \phi d\mathbf{S}}_{\text{Diffusive term}} + \underbrace{\int_V F_\phi dV}_{\text{Source term}} \quad (5.8)$$

They express respectively:



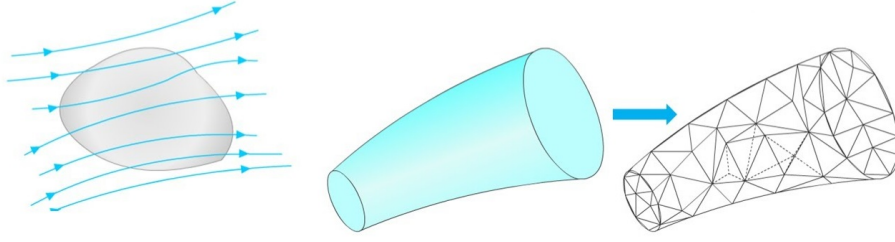


Figure 5.1: Finite Volume Method Discretization

- The time rate change of the fluid property  $\phi$  inside the control volume  $V$
- The net rate of decrease of  $\phi$  across the volume's boundaries due to convection with velocity  $\mathbf{u}$
- As convective but due to diffusion
- The generation and/or destruction of  $\phi$  inside the control volume

The surface integrals are evaluate using quadrature approximations, while the source term volume integral as the product of mean value at the cell center and its volume. Both of these approximations are second-order accurate.

The convective term is discretized using upwind schemes with limiters that involve the product of the mass flow rate at face and the value of  $\phi$  at the face.

To discretize the diffusive term of Eq.5.8 an accurate 2nd-order expression for the interior face gradient  $\nabla\phi$  is required and involves different methods of decomposition.

The transient term comes into play in transient simulations so time  $t$  is an additional coordinate. The most used methods are fundamentally Euler's implicit and explicit schemes. Below it is presented the Euler implicit scheme of 1st-order accuracy. The total time  $t$  is subdivided into time-steps  $\Delta t$  and the algorithm approximates the transient term in Eq.5.8 in the  $i$ -th cell using the solution at the current time step  $n + 1$  and the one from the previous ( $n$ ):

$$\frac{d}{dt}(\rho\phi V)_i = \frac{(\rho\phi V)_i^{n+1} - (\rho\phi V)_i^n}{\Delta t} \quad (5.9)$$

A second-order involves, for the  $n + 1$  time-step, the solutions at the current time and the previous two  $n$  and  $n - 1$ , each properly weighted.

### 5.1.3 Solver or governing equations

Fundamentally, solving the conseration equations for continuity 5.3, momentum 5.5, energy 5.7 and the closure equation, such as the state equation for ideal gases, means

the obtainment of the velocity field pressure and in general density. Therefore, the solution algorithms are commonly named Pressure-Velocity Coupled Equation Algorithm and there are essentially two types of solvers.

- Segregated Solver: the integral conservation equations of continuity and momentum are solved sequentially. The non-linearity is solved iteratively one after the other for the solution variables such as  $u_i$  and  $p$ . The pressure-velocity coupling sees the continuity equation as a constraint on velocity field that is first predicted and the corrected by the pressure. It is also called *predictor-corrector approach*.
- Coupled Solver: the governing equations and the closure ones are solved simultaneously as a vector of equations. The velocity is obtained from momentum equation, pressure from continuity and density from the equation of state.

Lastly, from a discrete and numerical point of view, it is described the integration in time that can be achieved through explicit time-stepping and implicit. In the explicit scheme the solution is obtained advancing from time  $t$  to time  $t + \Delta t$  with a  $n$ -th order Runge-Kutta scheme. The time step  $\Delta t$  has a physical meaning and it is applied uniformly to each cells in the domain.

In the implicit scheme it is used a pseudo-time for inner iterations  $\tau$ . In the general conservation law the diffusive term is making vanished through an inner iteration progress where the pseudo-t  $\tau$  is involved. When inner iteration converges the solution is updated to the next physical-meaning time-step  $\Delta t$ .

Both  $\Delta t$  in the explicit scheme and  $\Delta \tau$  in the implicit one are defined as:

$$\Delta \tau = \min \left( \frac{CFL \cdot V(\mathbf{x})}{\lambda_{max}(\mathbf{x})}, \frac{VNN \cdot \Delta x^2(\mathbf{x})}{\nu(\mathbf{x})} \right) \quad (5.10)$$

where  $CFL$  is the Courant–Friedrichs–Lewy number , a necessary condition for convergence while solving certain partial differential equations. In 1-dimension it can be written as follow:

$$CFL = \frac{u \Delta t}{\Delta x} \leq CFL_{max} \quad (5.11)$$

the max of  $CFL$  depends on whether the method is explicit or implicit, it usually equal to 1 or lesser for explicit schemes, whilst the implicit may tolerate greater values. The other values in EQ.5.11 are  $V$  the cell's volume,  $\lambda$  the eigenvalue of a relation between convective velocity, sound speed and the cell's surface area,  $VNN \approx 1$  is the VonNeumann number,  $\Delta x$  is the characteristic cell length scale and  $\nu$  the cinematic viscosity.

### 5.1.4 Turbulence

When I meet God, I am going to  
ask him two questions:  
Why relativity?  
And why turbulence?  
I really believe he will have an  
answer for the first.

---

*Werner Heisenberg*

Almost none except academic fluid flows are laminar. From an experimental point of view we define laminar flow a fluid motion in which macroscopic features, such as velocity or pressure, in every point and at any instant are fully deterministic and repeatable under the same conditions. If it does not occur, motion is said turbulent and so characterized by elements of randomness in space and time with regards to macroscopic characteristics. From the mathematical standpoint it means a chaotic behavior of Navier-Stokes equations which remain valid in general. The characteristics of turbulence can be resumed as follow:

- Unsteadyness: the macroscopic quantities, such as velocity and pressure, depend on time as well as their fluctuations, that are observed in a wide range of frequencies.
- Randomness: the equations are highly susceptible to the initial conditions and this dependency rises increasing Reynolds
- Vorticity and three-dimensionality: fluctuations of velocity become fluctuations of vorticity, described for incompressible flow by:

$$\frac{D\omega}{Dt} = (\omega \cdot \nabla)u + \nu \nabla^2 u \quad (5.12)$$

where  $\omega$  is the vorticity vector and  $u$  the velocity vector. The terms in brackets is called *stretching and tilting* term is zero under 3D since  $\nabla \cdot u = 0$ .

- Dissipation: the viscosity causes a growth of internal energy of fluid to the detriment of kinetic energy. Hence, turbulence requires a continuous supply of energy from mean motion in order to replace losses due to viscous dissipation.
- Reshuffling: all the physical quantities suffer a strong reshuffling, far superior compared to the one purely molecular.
- Wide scale range: turbulent flows involve a full range of scale both in time and space, extended up to the dimensions of the entire system.
- Continuum hypothesis are fulfilled, so N-S equation are valid.

- Turbulence is a flow's property, not of fluid.

Numerically, turbulence can be solved through three methods.

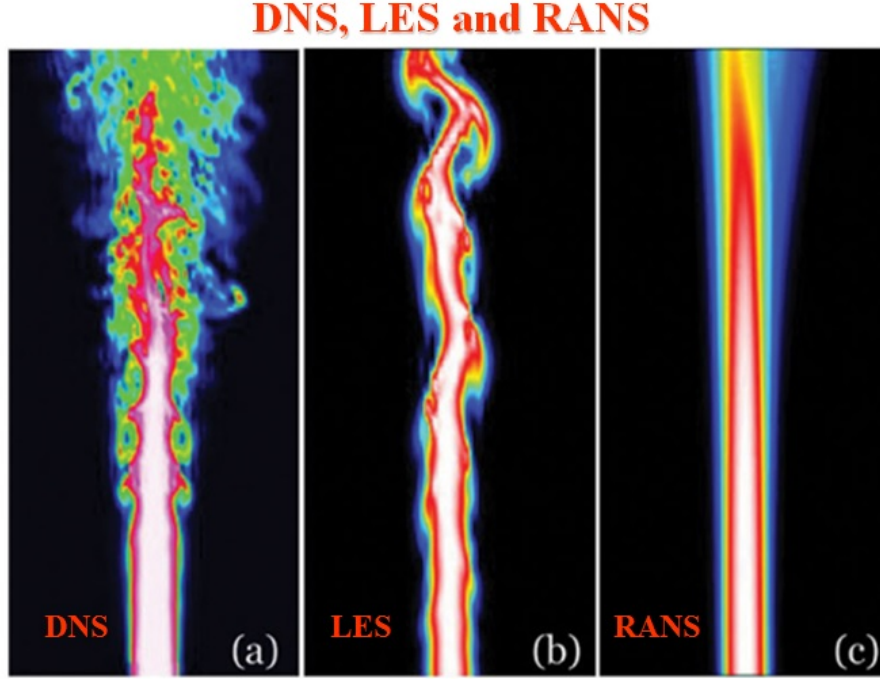


Figure 5.2: DNS (left), LES (middle) and RANS (right) predictions of a turbulent jet. - A. Maries, University of Pittsburgh

**Direct Numerical Simulation (DNS)** Since Navier-Stokes equations still remain valid, being assessed the continuum hypothesis, they can be solved directly, hence the method is so called. Such a method is surely the best in terms of accuracy, reliability of outcomes and about the understanding of physics. The great drawback is the gargantuan cost both in time and amount of data. It can be proven that the number of discretization points in space  $N_{\Delta x}$  and in time  $N_{\Delta t}$  are proportional to Reynolds, so for an industrial application, where  $Re \approx 10^6$ , the amount of data  $N$  is:

$$N = 4(N_{\Delta x})^3 N_{\Delta t} \approx 4 Re^{11/4} \approx 10^{17}$$

**Reynolds Averaged Navier-Stokes (RANS)** The generic variable can be written as the sum of its mean, or averaged, value and its fluctuation  $\phi = \bar{\phi} + \phi'$  so the governing equation of continuity 5.3 and momentum balance 5.5 can be

rewritten as:

$$\frac{\partial \rho}{\partial t} + \nabla \cdot (\rho \bar{\mathbf{u}}) = 0 \quad (5.13)$$

$$\frac{\partial}{\partial t} (\rho \bar{\mathbf{u}}) + \nabla \cdot (\rho \bar{\mathbf{u}} \otimes \bar{\mathbf{u}}) = -\nabla \cdot \bar{p} \mathbf{I} + \nabla \cdot (\mathbf{T} + \mathbf{T}_{TRANS}) + \mathbf{f}_b \quad (5.14)$$

where the over-bar indicates the averaged value,  $\mathbf{I}$  is the identity tensor,  $\mathbf{T}$  is the viscous stress tensor and  $\mathbf{f}_b$  the resultant of body forces. The new term given by  $\mathbf{T}_{TRANS}$  contains the adding terms  $\rho u_i u_j$ , arose from Reynolds decomposition into mean value and fluctuation, and the turbulent kinetic energy  $k$ . These so-called Reynolds stresses make the number of unknown variables exceeds the number of equation, so the system is open; it is known as *problem of closure of Reynolds averaged equations*. A way to close the system, ie. express the Reynolds stress tensor as a function of the mean flow velocity, is the introduction of the *eddy viscosity* starting from the analogy between molecular gradient-diffusion and turbulent motion (Boussinesq hypothesis). This formulation led to express the components of Reynolds stress tensor as :

$$\tau_{ij} = \rho(\nu + \nu_T) \left( \frac{\partial \bar{u}_i}{\partial x_j} + \frac{\partial \bar{u}_j}{\partial x_i} \right) \quad (5.15)$$

So the focus is now to define the eddy viscosity  $\nu_T$ . There are various methods to do so and the most used are briefly reported:

- Mixture Lenght Model : it is 0-th order model where  $\nu_T$  is proportional to the derivative of mean velocity with respect to the distance  $y$  through the vonKarmann constant  $\kappa = 0.41$
- $K$  Model: a 1-st order model where the eddy viscosity is proportional to the turbulent kinetic energy  $K$ :

$$\bar{K} = \frac{1}{2} u_i \bar{u}_j \quad \Rightarrow \quad \nu_T \propto \sqrt{\bar{K}}$$

- $K - \varepsilon$  Model: a 2-equation model that solves equations for  $K$  and the turbulent dissipation rate  $\varepsilon$  while this last one variable was before treated as known, given  $K$ .
- $K - \omega$  Model: like the previous is a 2-equation model, but instead of the dissipation rate  $\varepsilon$ , the second equation solves for  $\omega \propto \varepsilon/K$  the dissipation rate per unit turbulent kinetic energy, in order to obtain the eddy viscosity  $\nu_T$ .

**Large Eddy Simulation (LES)** As said a direct simulation of all scale, even the smallest (the Kolmogorov scale) is far costly and it is not practical and available for

what concerns industrial, or in general, engineering problems. Turbulence carries a wide range of scale: the largest scales' nature is convective and so dominated by high Reynolds, recalling the energy cascade, we find the intermediate scale whose are responsible for the energy transfer from largest so smallest, so these last one have dissipative nature and through the viscosity convert kinetic energy into heat. Hence smallest scale are dominated by low Reynolds, short characteristic time and decay exponentially, so the basis idea of LES is to model the smallest scale in order to obtain a simulation with the accuracy close to a DNS, solving large and medium scales, but affordable like a RANS, modeling smallest vortices, through a *spatial filter*. LES techniques are commonly used in weather forecasting.

## 5.2 Validation of CFD simulations

Within the scope of this thesis about VIVs simulation for an energy harvester, this section describes the validation of the numerical CFD model usign the commercial solver STAR-CCM+ by Siemens.

Firstly a domain and grid validation was carried for a steady case of turbulent flow around cylinder, the outcomes are the discretization errors and grid convergence plot.

Secondly a time discretization validation was assessed to obtain a stable simulation in terms of frequencies, so Strhoual, and compared to values found in literature and obtained through numerical model of the previous chapter.

In the following section the validated model is described and finally the results in the last section of this chapter are reported.

### 5.2.1 Domain determination and mesh type

The very first important step in a CFD simulation is the determination of the domain and at the same time the evaluation of grid type, according the options available in the software.

For the problem considered the best choice is surely a rectangular domain and because of the importance of the wake a refinement is needed in that zone.

### 5.2.2 Mesh quality

In this section the criteria given by STAR-CCM+ are reported in order to describe the quality of a mesh grid.

**Face validity** This feature describes the validity of a 2D mesh element in terms of an are-weighted measure. As reported in the Fig.5.3 below the normal vectors point outwards with the respect to the cell's centroid; in such a case the value is 1.

**Volume change** The volume change metric describes the ratio of the volume of a cell to that of its largest neighbor.

**Cell quality** It is a function not only of the relative geometric distribution of the cell centroids of the face neighbor cells, but also of the orientation of the cell faces. Generally, flat cells with highly non-orthogonal faces have a low cell quality.

**Skewness angle** This skewness angle  $\theta$ , according to the Fig.5.6 below, measures whether the cells on either side of a face are formed in such a way as to permit diffusion of quantities without these quantities becoming unbounded. An angle of zero indicates a perfectly orthogonal mesh and cells with a skewness angle greater than  $85^\circ$  are considered as bad. Furthermore angle greater than  $90^\circ$  cause convergence issues.

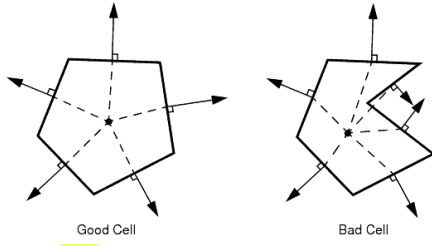


Figure 5.3: Face validity

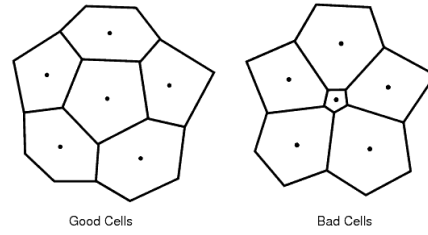


Figure 5.4: Volume change

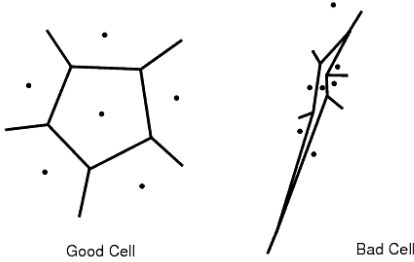


Figure 5.5: Cell quality

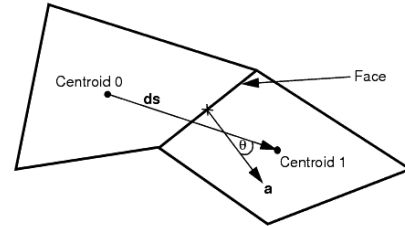


Figure 5.6: Skewness angle

In order to evaluate the best mesh type all the setups allowed by the software have been analyzed. The Figs.5.7, 5.8 and 5.9 below report the configurations considered, respectively **triangular**, **polyhedral** and **quadrilateral**. Results are obtained concerning the quality measures introduced are reported in the Tab. 5.2.2.

	TRIA		POLY		QUAD	
	MIN	MAX	MIN	MAX	MIN	MAX
SA	—	3.46E+01	—	3.86E+01	—	2.85E+01
CQ	5.24E-05	—	5.44E-05	—	5.26E-05	—
VC	4.27E-01	—	1.59E-01	—	3.19E-01	—

Table 5.1: Mesh quality measures in grid analysis

The outcomes in Tab.5.2.2 indicates respectively the skewness angle SA, the cell quality CQ and the volume change VC. The best choice is to be found in maximum between minimum values of volume change and results to be the triangular mesh.

### 5.2.3 Domain size

It has been verified that the inlet and outlet surface size does not affect the solution [33], nevertheless the good practices recommend to use a semi-height size for both inlet and outlet equal to 10 times the cylinder diameter. In the case considered coming out from the dimensional analysis it is taken into account a diameter  $D = 0.16$  m so a total height of 3.2m for inlet and outlet boundaries. The same reasoning is applied to the distance inlet-cylinder.

It is a slightly different case for the outlet distance in which a different behavior arises varying the space between cylinder and outlet. In order to achieve a best compromise to avoid a huge domain a simulation at low Reynolds has been conducted and Strouhal number evaluated to select the minimum stable distance between cylinder and outlet. The vortex shedding was analyzed and the following example Fig.5.11 shows the vorticity at  $Re = 75$ . Five simulation, varying the length cylinder-outlet, have been conducted to evaluate the Strouhal number obtaining the frequency from the coefficient of lift  $C_L$  time history, an example is shown in Fig.5.12. The distance varies from 7 times the diameter up to 40 and results in terms of Strouhal number are reported in the following Tab.5.2.3. Where the percentage error in the third column is evaluated considering the Strouhal difference with respect to the previous case and normalized on the case considered. It is noteworthy the absence of shedding phenomenon in the case 7D, ie. a distance cylinder-outlet equal to 1.12m; in such a case a prevalent frequency is not observable so the Strouhal cannot be evaluated. According to the results in Tab.5.2.3, as best result the case **30D** was chosen.



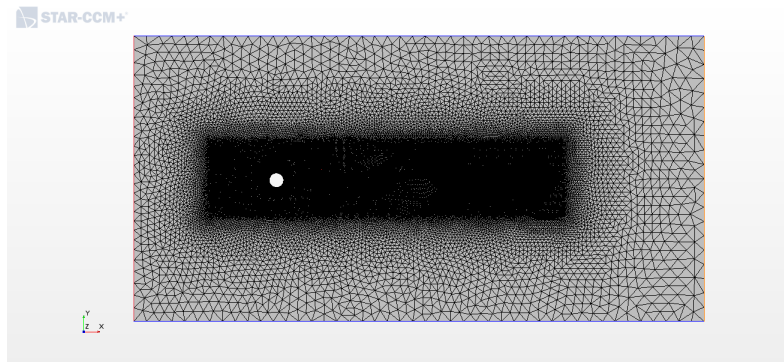


Figure 5.7: Triangular Mesh

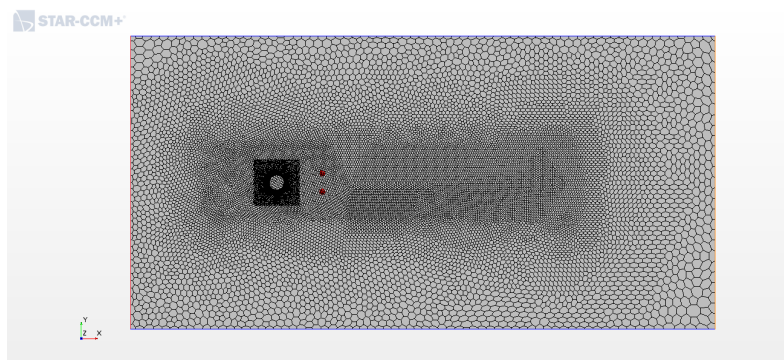


Figure 5.8: Polyhedral Mesh

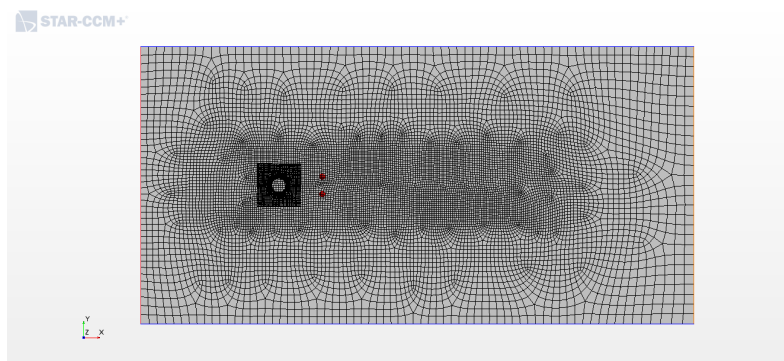


Figure 5.9: Quadrilateral mesh

Figure 5.10: Mesh setups in grid quality analysis

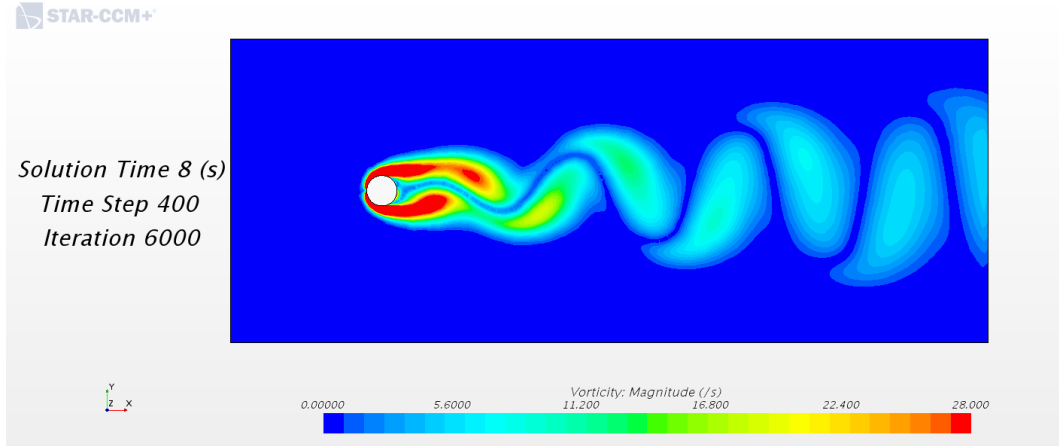


Figure 5.11: Simulation at low Reynolds number  $Re = 75$  to observe vortex shedding for the evaluation of Sthroual and distance between cylinder and outlet

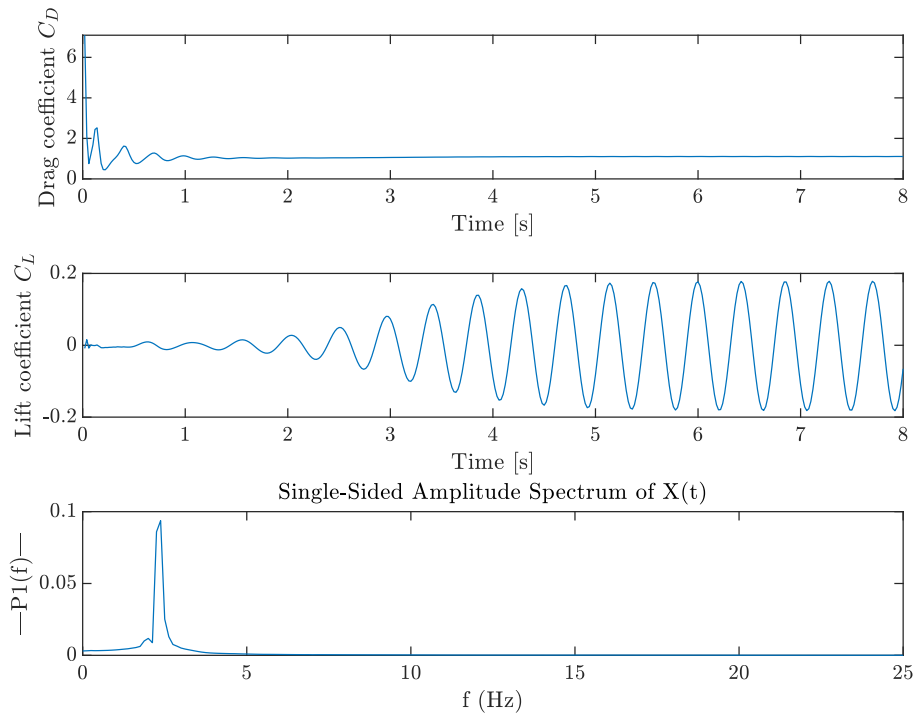


Figure 5.12: Drag and Lift coefficient at low Re  $Re = 75$  in domain size analysis and frequency analysis through Fast Fourier Transformation FFT.

Case	$St$	Err%
7D	—	—
10D	0.16985	—
25D	1.1715	85.501%
30D	1.17299	0.1267%
40D	1.17365	0.0564%

Table 5.2: Strouhal number at low Reynolds  $Re$  to evaluate the distance between cylinder and outlet face.

The outcome of the domain size analysis is the geometry in Fig.5.13 where the origin coincides with the center of cylinder of diameter  $D = 0.16\text{m}$ , both inlet and outlet heights are  $1.6\text{m}$ , the distance inlet-diameter is 10 times the diameter and the gap cylinder-outlet equal to 30 times the diameter  $4.8\text{m}$ .

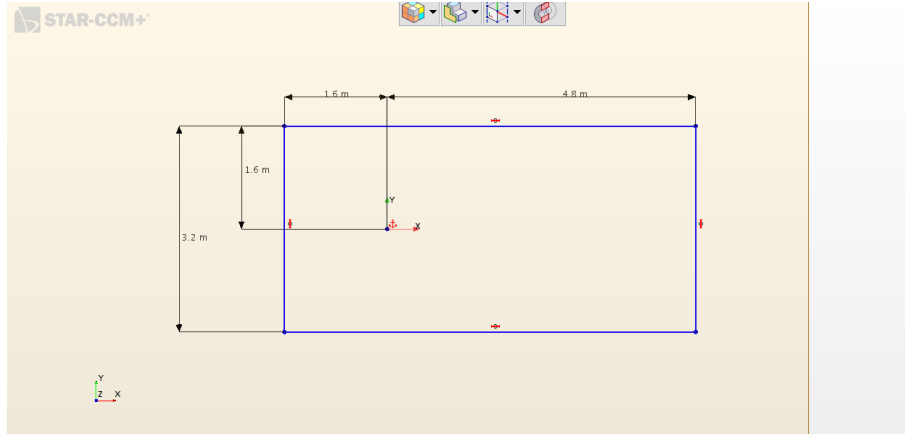


Figure 5.13: Domain geometry in CAD environment.

#### 5.2.4 Number of cells

Given the mesh type by quality measures and the domain size by a frequency analysis of vortex shedding at low  $Re$ , a grid study in terms of cell number was conducted. Starting from a coarse grid a refinement was carried on until the finest mesh permitted by the RAM available. In detail, maintaining unchanged all over the mesh parameter fixed by the analysis above and fixed the domain dimensions, the refinement was achieved varying the so-called *Base Size*. Citing [24] "The Base Size is a characteristic dimension of the model that you set before using any relative values. As general examples, you can set the base size to the diameter of an inlet, the length of the fluid volume, or a size that is convenient for scaling other values". This feature allows to keep the consistency of the mesh, so not varying all the other parameters resumed as follows.

Part	Parameter	Value	Description
Domain	Base Size	Varying	Reference length for all relative size controls
	Target Size	100%	Face size that mesher aims to achieve
	Minimum Size	25%	Remove mesh edges below this size where feasible
	Curvature	36	Number of points per circle
	Growth Rate	1.1	Maximum size ratio of connected edges
Refinement	Size	7.5%	Volumetric control of refinement size
Cylinder	Target Size	7.5%	Size aimed around cylinder
	Minimum Size	3%	Minimum face size where feasible
	Growth Rate	1.05	Size ratio of connected edges

Table 5.3: 2D triangular mesher parameters.

In this analysis' stage a same 2D simulation at low Reynolds was carried out and the convergence was achieved in terms of the drag coefficient  $C_D$ . Varying *Base Size* from a greater to a smaller value means to increase the number of cell; for each simulation the coefficient was obtained as reported below both in tabular and chart form.

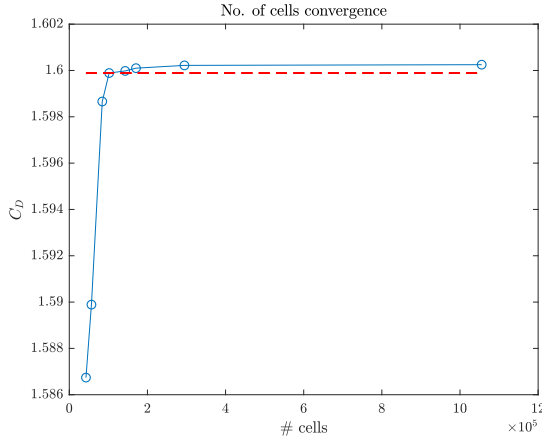


Figure 5.14: No. cells convergence

Base size		No.cells	CD
m	%	#	—
0.240	150	42714	1.58674
0.200	125	56716	1.58989
0.160	100	84410	1.59866
0.140	87.5	102062	1.59989
0.120	75	143064	1.59998
0.100	62.5	170728	1.60001
0.080	50	294750	1.60022
0.040	25	1055488	1.60025

Table 5.4: Convergence data

According to the analysis and results in Fig.5.14 and Tab.5.4 the minimum number of element to obtain an accurate solution is about 100k corresponding to a base size of 85% with respect of cylinder diameter  $D = 0.16m$ .

### 5.2.5 Discretization Error

A further analysis could be done estimating the discretization error using the Grid Convergence Index **GCI** due to Roache [21] based the extrapolation by Richardson. The GCI is a measure of the difference between the quantity calculated and the numerical asymptotic value obtainable from a negligible spacing grid. A consistent numerical analysis will provide a result which approaches the actual result as the grid resolution approaches zero. It is an alternative way respect the traditional convergence analysis, where rigorously the exact solution must be considered; in fact in most practical problems the exact solution is unknown.

Defining  $h$  the grid discretization parameter, in our case the minimum cell size, three grids from a coarsest to a finest are considered, so  $h_1 < h_2 < h_3$ . The grid refinement is defined as:

$$r_{ij} = \frac{h_j}{h_i} \quad (5.16)$$

The solution is done for all the three cases and it is  $f_i$  for the  $i$ -th case. So the *order of convergence*  $p$  is:

$$p = \frac{\ln \left( \frac{f_3 - f_2}{f_2 - f_1} \right)}{\ln r} \quad (5.17)$$

The Richardson Extrapolation let to write the exact quantity  $f_{ex}$  as :

$$f_{ex} \approx f_1 - \frac{f_2 - f_1}{r_{21}^p - 1} \quad (5.18)$$

Where the grid refinement  $r_{21}$  is considered as the ratio between the mesh case 2 over the 1. From the Eq.5.18 it is possible to define the relative error between two finest grids by:

$$e_{21} = \left| \frac{f_2 - f_1}{f_1} \right| \quad (5.19)$$

Rewriting the equations three time for all the cases the following system of equation is reached:

$$\begin{cases} p &= \frac{\ln(f_{32}/f_{21}) + q(p)}{\ln r_{21}} \\ q(p) &= \ln \frac{r_{21}^p - s}{r_{32}^p - s} \\ s &= \text{sign} \frac{f_{32}}{f_{21}} \end{cases} \quad (5.20)$$

where  $f_{ij} = f_i - f_j$  and the iterative equation is resolved starting from the initial guess  $q(p) = 0$ . Finally the **GCI** is given by:

$$\mathbf{GCI}_{21} = F_s \frac{e_{21}}{r_{21}^p - 1} \quad (5.21)$$

Where  $F_s = 1.25$  is a *safety factor* and is based on experience applying GCI in many situation by Roache[21].

Such a method is applied for the case at base size equal to 87.5% in Tab.5.4 and the outcomes are reported in the report output 5.2.5. The computation was performed through a Fortran90 code available from NASA website [29].

```

—— VERIFY: Performs verification calculations ——

Number of data sets read =                3

Grid Size      Quantity
0.120000      1.599980
0.140000      1.599890
0.160000      1.598660

Order of convergence using first three finest grid
and assuming constant grid refinement (Eqn. 5.10.6.1)
Order of Convergence, p =      1.6963443

Richardson Extrapolation: Use above order of convergence
and first and second finest grids (Eqn. 5.4.1)
Estimate to zero grid value, f\_exact =      1.59998715

Grid Convergence Index on fine grids. Uses p from above.
Factor of Safety =      1.25000000

Grid      Refinement
Step      Ratio, r      GCI(%)
1  2      1.166667      0.000555
2  3      1.142857      0.011132

Checking for asymptotic range using Eqn. 5.10.5.2.
A ratio of 1.0 indicates asymptotic range.

Grid Range      Ratio
12 23           0.681505

—— End of VERIFY ——

```

The GCI index results to be fine, with respect to the coarser grid is about 0.011%, while respecting the finer one is really negligible and equal to 0.0005%. Hence a further thickening of the mesh grid is not required.

## 5.3 Simulations

In this section the 2D simulation of vortex induced vibration concerning the cylinder carried out from the dimensional analysis and design of the pertinent chapter, are reported. Since the huge amount of data and computational costs in terms of time, 5 cases were analyzed in order to compare amplitude ratio with the outcomes of numerical model.

Case	S1	S2	S3	S4	S5
Reduced Velocity	2.5	4.0	5.2	6.5	8.0

Table 5.5: Cases analyzed

### 5.3.1 Domain and Mesh

Domain dimensions analyzed in the grid convergence and size design section are shown in the following Fig.5.15 and for the sake of clarity the dimensions are summarized in Tab.5.6.

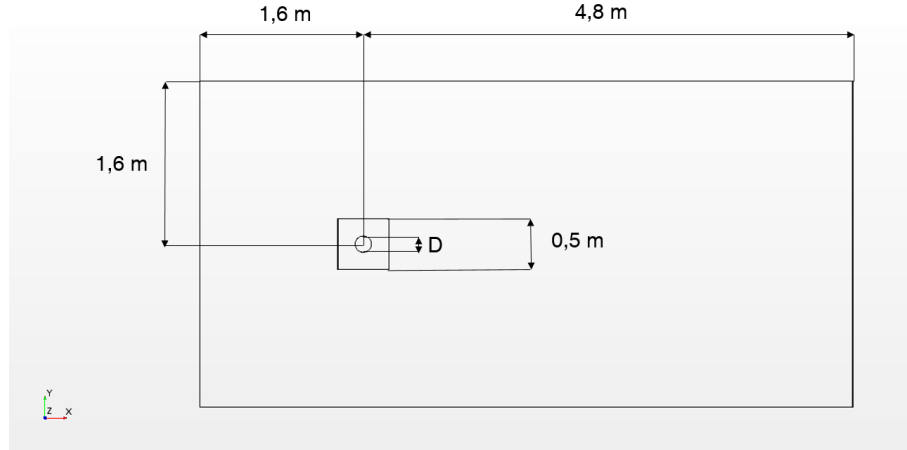


Figure 5.15: Domain sizes in VIVs simulation

Cylinder Diameter $D$	0.16m
Inlet-cylinder distance	1.6m
Cylinder-Outlet distance	4.8m
Inlet/Outlet height	3.2m
Overset square side	0.5m

Table 5.6: Domain geometric characteristics

The triangular mesher in CAE enviroment STAR-CCM+ was chosen after the considerations in the previous step through the mesh quality measures. In the following Fig.5.16 three regions are indicated: *Domain*, *Refinement* and *Overset*. The second one allow to refine gradually the mesh size in order to avoid a growth rate too high and so allows a better accuracy without placing too much in terms of number of cells. This Refinement in wake region has a total length equal to 4.0m and height of 0.9m. The mesh size in this region are imposed as a volumetric control and its value is equal to 7.5% of the base size equal to 85% of cylinder diameter.

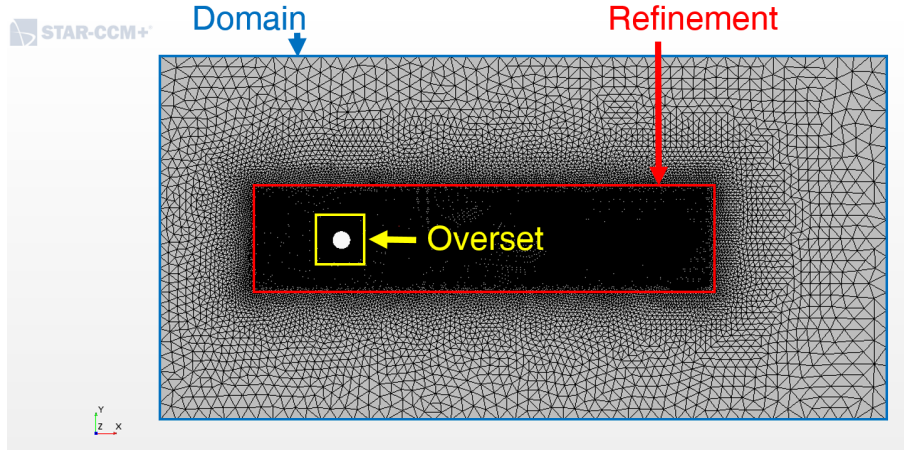


Figure 5.16: Mesh regions in VIVs simulation

### 5.3.2 Overset Mesh

Overset meshes are also known as Chimera or overlapping meshes. An overset mesh typically containing a body of interest such as a boat or a gear is superimposed on a background mesh containing the surrounding geometry and data is interpolated between the two. This approach allows complex motions without remeshing techniques that would involve the whole domain, so reducing solving time.

Overset meshes typically involve a background mesh adapted to the environment and one or more overset grids attached to bodies, overlapping with the background mesh. In the Fig.5.17 is represented the data transfer between overset mesh (red) and background mesh (blue). Acceptor cells (dotted line) provide information for the calculation of active cell center values (orange and blue). For each acceptor cell, donor cells must be found and this set depends on the interpolation method and on the number of active cells in the donor region around the acceptor cell centroid. Active cells are those ones in which discretizing governing equations are solved. In the simulations conducted and exposed in this thesis a least square interpolation



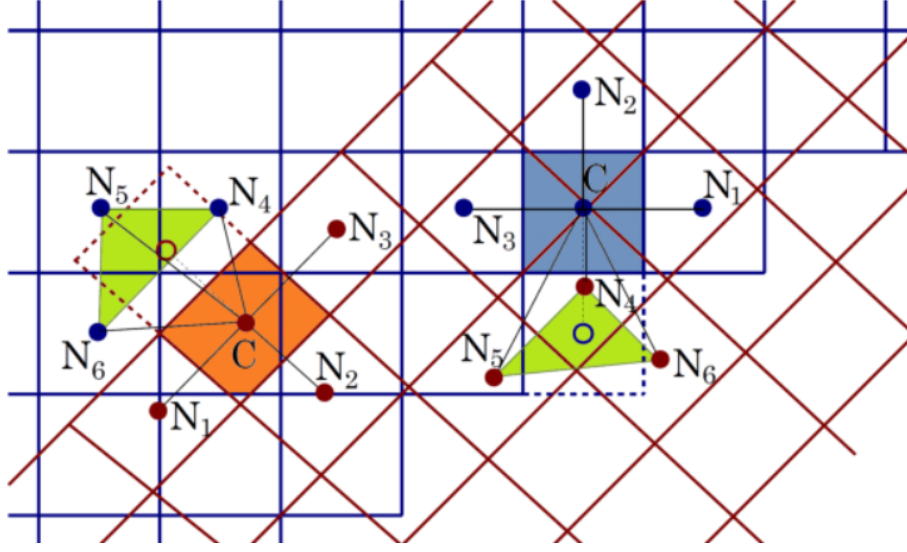


Figure 5.17: Data transfer between overset mesh and background

was chosen and the following Fig.5.18 indicate the overset cell type, ie. the blue ones are the donor cells and the red cells are the acceptors, the contour indicates that all cells are active.

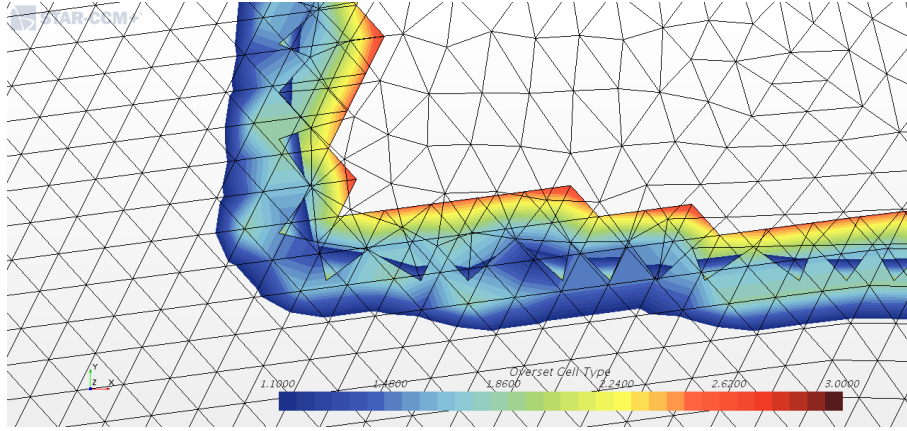


Figure 5.18: Overset Cell Status

### 5.3.3 DFBI Solver

The **DFBI** (Dynamic Fluid Body Interaction) is the module to simulate motion of a rigid body, ie. an object in which the relative distance between internal points does not change, in response to forces exerted by physics continuum and any additional forces and couplings defined by the user. It is a 6DoF solver, but in our

case, conducting 2D simulations the degree of freedom are naturally limited to the translation along cross direction  $y$ .

The effect of the motion of the cylinder on the fluid is accounted for by moving the entire fluid mesh rigidly using the overset technique above.

Since the cylinder is physically connected to a spring a body coupling is requested, so the body is connected to the domain through a linear spring which an elastic force tends to restore the equilibrium state or in this case the resonance induced by vortices. the Fig.5.19 below shows the linear spring coupling implemented. As regards the damping obtained by the numerical analysis in previous chapter a

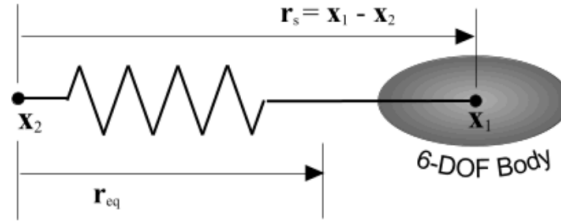


Figure 5.19: Linear spring coupling

**damping force** proportional to the body's velocity was defined in DFBI setup as an external force acting with respect to the center of mass of the body.

### 5.3.4 Model Setup

Once the mesh operations were completed, the model setup followed starting from the definition of the **boundary conditions** considering the turbulence specification for a  $K - \varepsilon$  model:

- Domain Region:

Inlet: the velocity is specified in components  $\mathbf{V} = u\mathbf{i} + v\mathbf{j}$  where, since the flow is uniform and totally directed along the x-axis  $v = 0$ . Regarding turbulence the specification are implemented specifying **Intensity** and **Length Scale**. Best practices and theory state to use the 7% of the inlet size for the Length Scale and the Turbulence Intensity  $I$  was calculated as follow:

$$I = \sqrt{\frac{1.5v_t^2}{U^2}} \quad (5.22)$$

where  $v_t$  is the turbulent velocity scale equal to the 10% of the free-stream velocity  $U$ .

Outlet: pressure boundary defined in Pa

Top and Bottom walls: symmetry planes with zero shear.

- Overset Region:

Boundaries: is the overlap region in which acceptors and donors are defined.

Cylinder: smooth wall with a dynamic overset behaviour and a no-slip shear stress specification. The boundary layer is modeled through the Prism Layer Mesh in order to obtain a low  $y+$  with 10 number of layers, a near wall thickness of about  $y_w = 4.08 \cdot 10^{-5}\text{m}$  and a total thickness of 1cm. The estimation was conducted considering the boundary layer theory [23] using the force coefficient expression  $c_f = 0.058 \cdot Re^{-0.2}$ ; and a target  $y$ -plus equal to 1.

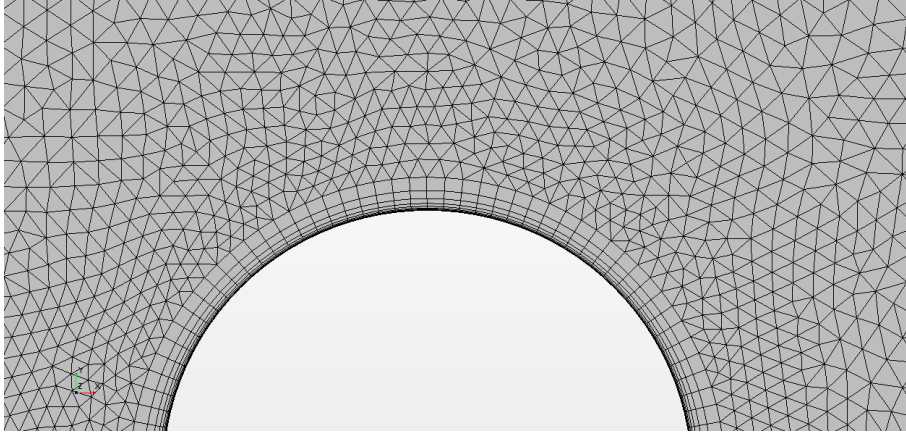


Figure 5.20: Prism Layer Mesh

As regard the **DFBI** module the cylinder is implemented as a rigid body, being 2D the motion is 1DoF translating in  $y$ -direction. The center of mass coincide with the global coordinate system origin and the mass of cylinder is equal to 51.57kg. Damping force and spring constant are respectively 35.52Ns/m and 955.61N/m. In order to a stable solution it was set a delay time of 0.1s before calculation of body motion begins. This so-called release time allows some time for the fluid flow to initialize. Furthermore a ramp time of 1s was imposed because at release time, force and moments are applied to the body can cause a shock effect.

### Solver properties

Time marching model selected is the **Implicit Unsteady**. Firstly an adaptive time stepping was used in order to obtain a relatively small CFL, it was noticed that, even for an implicit time marching, the solution does not converge if the physical time step value is high. After the first simulations a fixed time step equal to 0.001s was selected for the sake of clarity during post-processing and analysis of results. Temporal discretization is a 1-st order accuracy.

The **6DoF solver** was set to 10 maximum number of iteration within a time-step. The governing equations are solved in a coupled manner selecting the **Coupled Solver** with a 2nd order discretization accuracy with first a low value for the Courant number, then increased to 50 as suggested by user guides.

Turbulence is modeled through the **Realizable  $K - \varepsilon$**  that contains a different form of the  $\varepsilon$  turbulent dissipation rate equation. This model is recommended for high Reynolds simulations.

Finally about fluid a constant density, so incompressible flow, were set up considering **seawater** with density  $\rho = 1026\text{kg/m}^3$  and dynamic viscosity  $\mu = 0.00123\text{Pa.s}$ .

## 5.4 Results

For each simulation from the smallest reduced velocity to the largest, results are reported in terms of scalar scenes e plots. In a next step the outcomes are post-processed in order to be compared to numerical Matlab model presented in the 4th chapter.

Furthermore two probes have been included in the simulation in order to evaluate shedding at cylinder downstream.

### 5.4.1 Simulation at $U_r = 2.5$

A first simulation is conducted for a reduced velocity  $U_r = 2.5$ . So the boundary conditions for the velocity inlet are the following:

$U_r$	$U$	$v_t$	$I$
2.5	0.2740	0.0274	0.1224

Table 5.7: Velocity inlet BC for  $U_r = 2.5$

This first case considered carried out come problems inherent to the initial transitory Fig.5.24. Strong oscillations occurred are reported in the charts below. It should be noted that transitory oscillations led to a bad computation od drag coefficient in Fig.5.26.

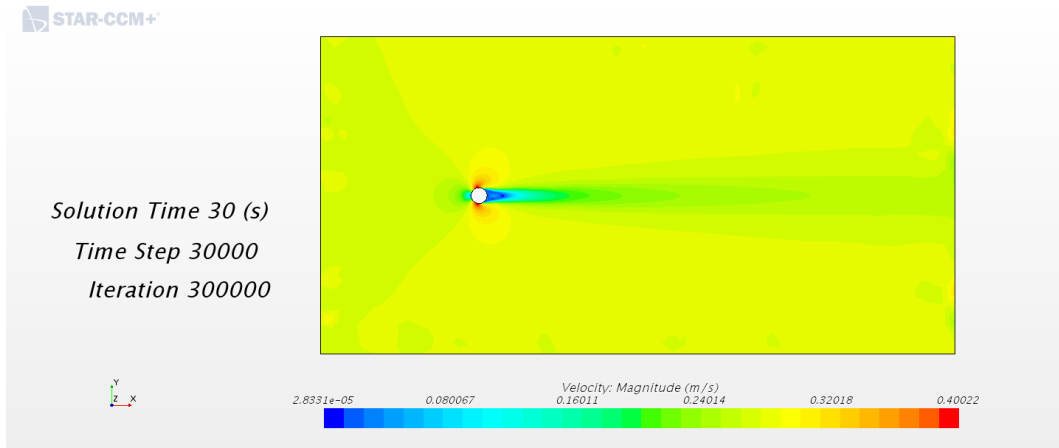


Figure 5.21: Velocity Magnitude scene for  $U_r = 2.5$

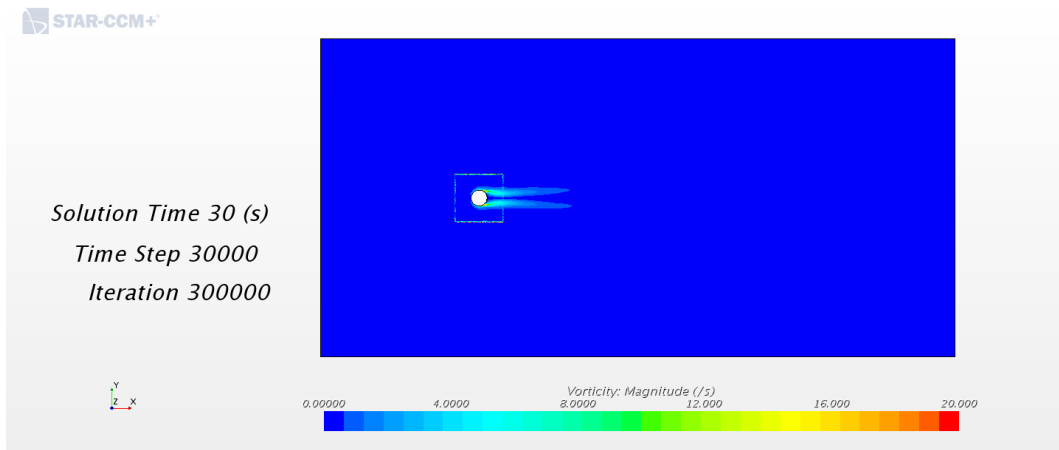


Figure 5.22: Vorticity Magnitude scene for  $U_r = 2.5$

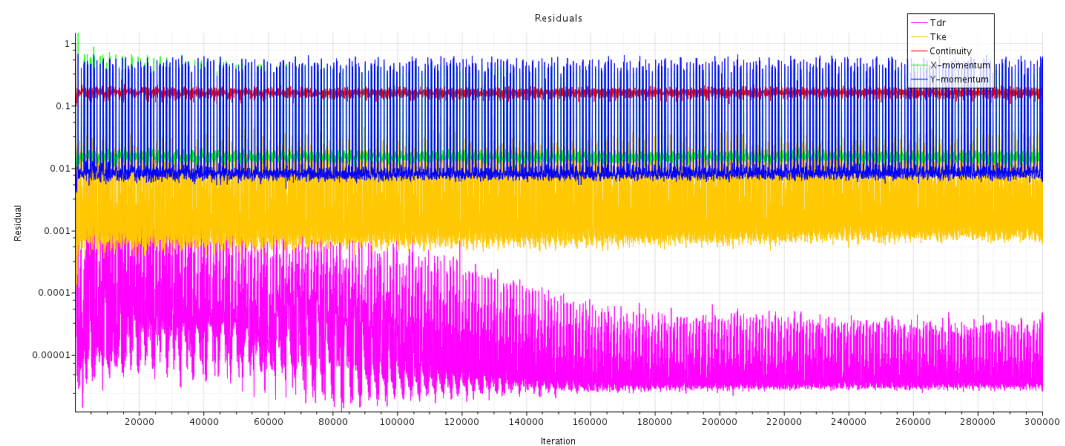
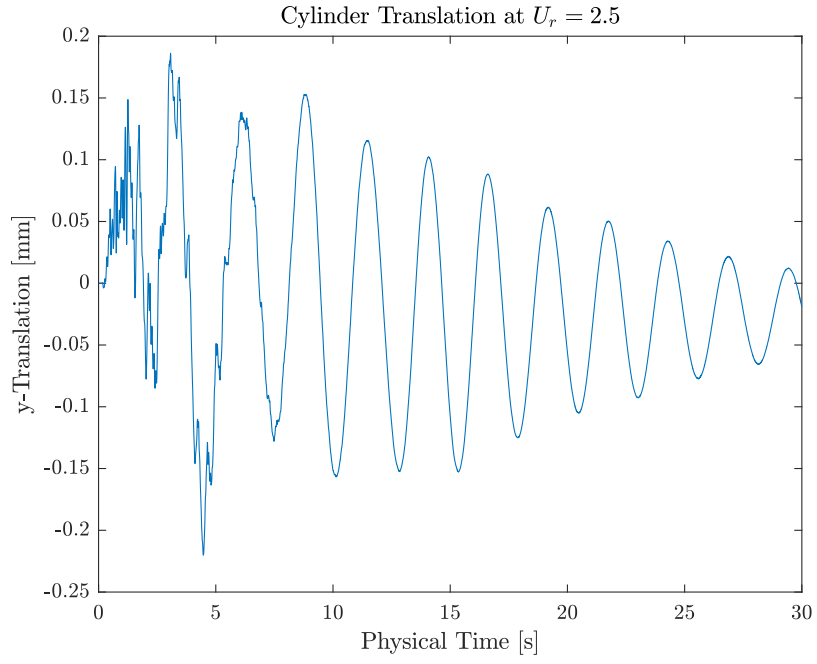
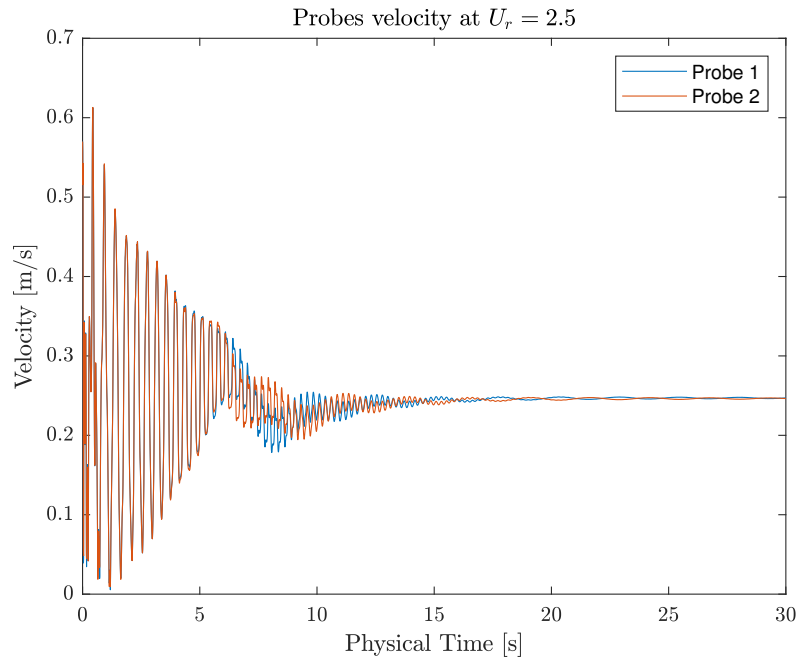


Figure 5.23: Residuals for  $U_r = 2.5$

Figure 5.24: Translation plot for  $U_r = 2.5$ Figure 5.25: Probes Velocity for  $U_r = 2.5$

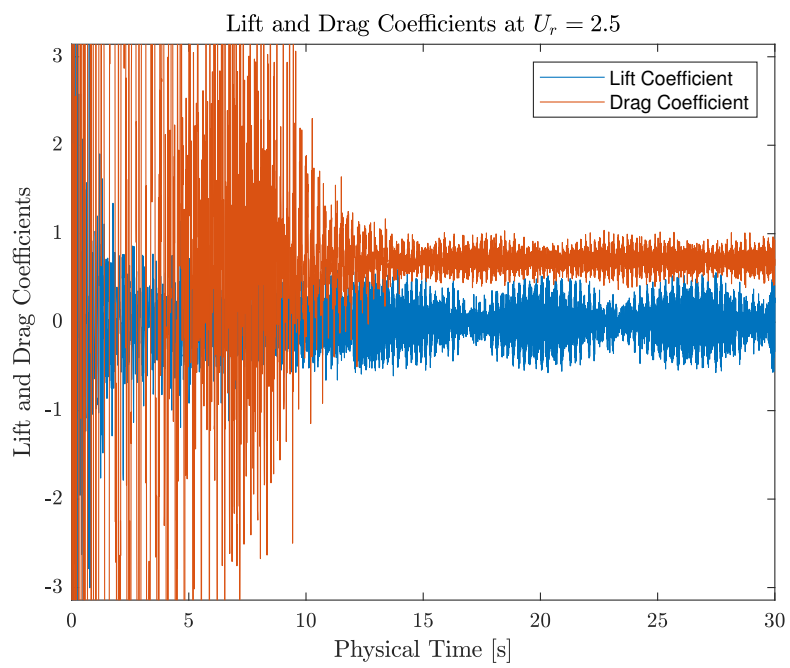


Figure 5.26: Lift and Drag Coefficients for  $U_r = 2.5$

### 5.4.2 Simulation at $U_r = 4.0$

The second simulation  $S2$  were conducted at the reduced velocity of  $U_r = 4.0$ .

$U_r$	$U$	$v_t$	$I$
4	0.4384	0.0438	0.1224

Table 5.8: Velocity inlet BC for  $U_r = 4.0$

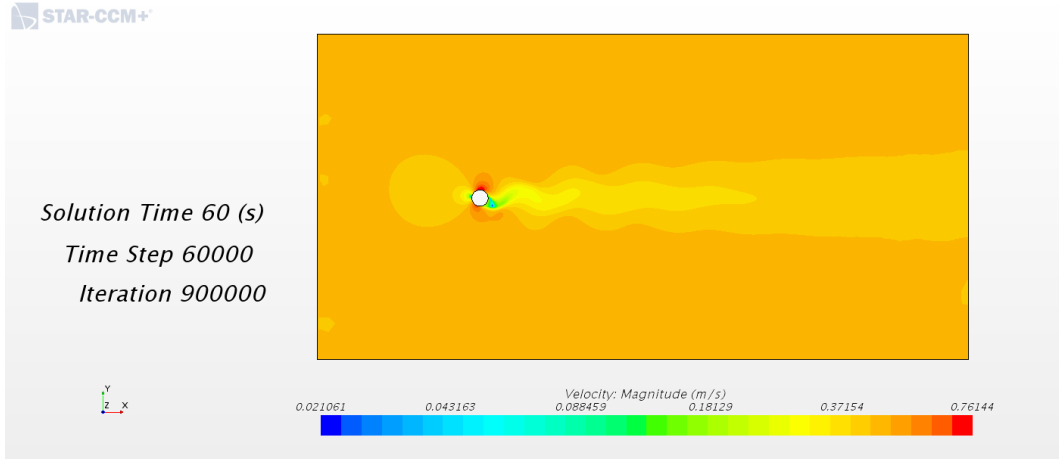


Figure 5.27: Velocity Magnitude scene for  $U_r = 4.0$

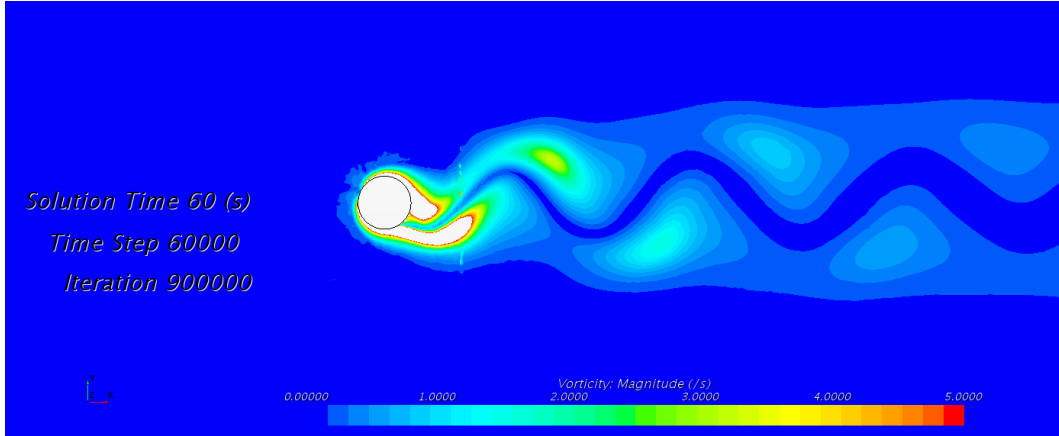


Figure 5.28: Vorticity Magnitude scene for  $U_r = 4.0$

In this case the VIV phenomenon starts to rise, vortex shedding is evident with respect to probes measures in Fig.5.33. Lift coefficient oscillates around zero and drag rises as expected. Performing an FFT analysis about translation a frequency equal to 7.4Hz was calculated as plotted in Fig.5.32.



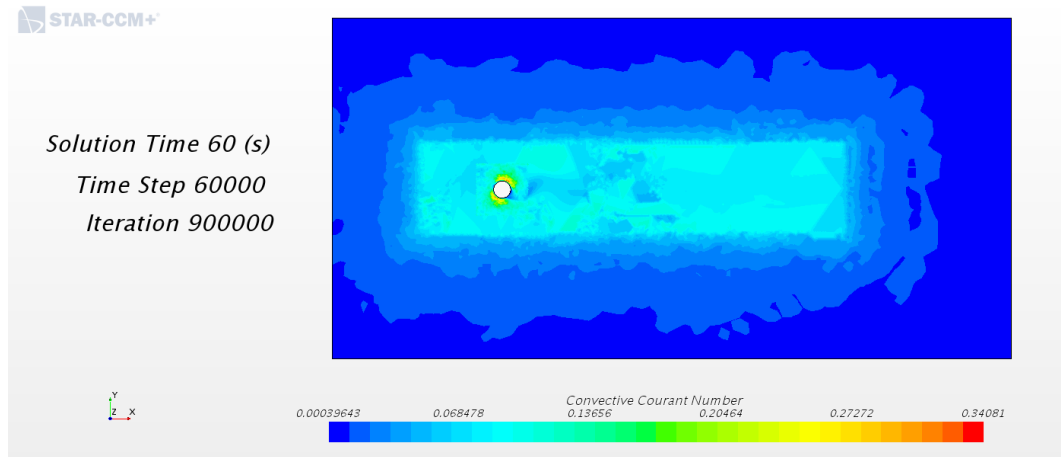


Figure 5.29: CFL scene for  $U_r = 4.0$

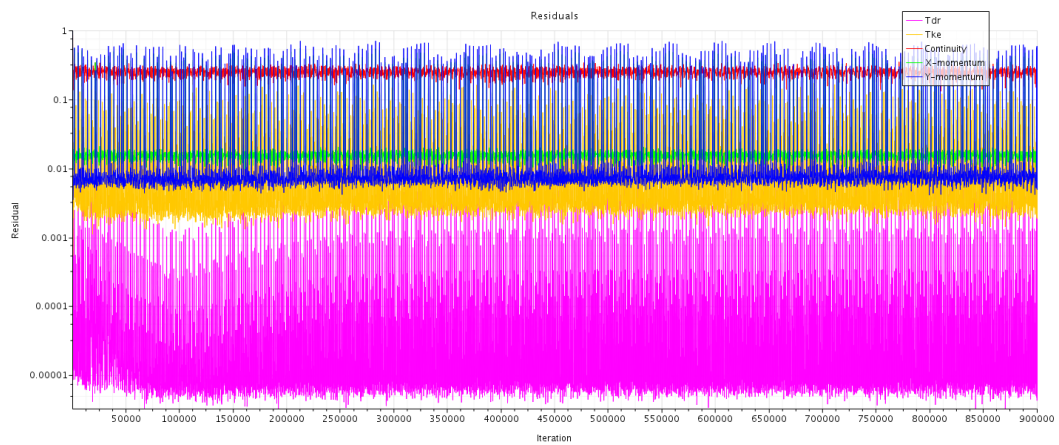


Figure 5.30: Residuals for  $U_r = 4.0$

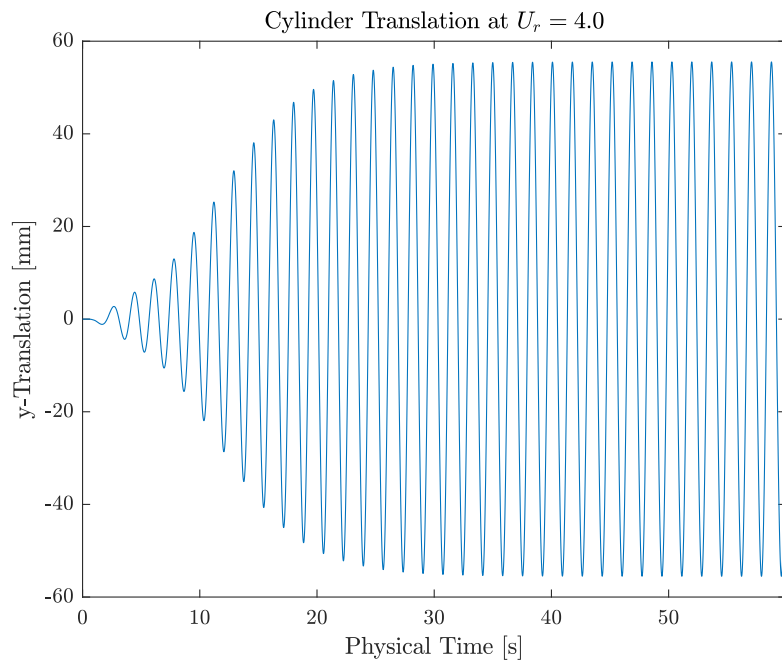


Figure 5.31: Translation plot for  $U_r = 4.0$

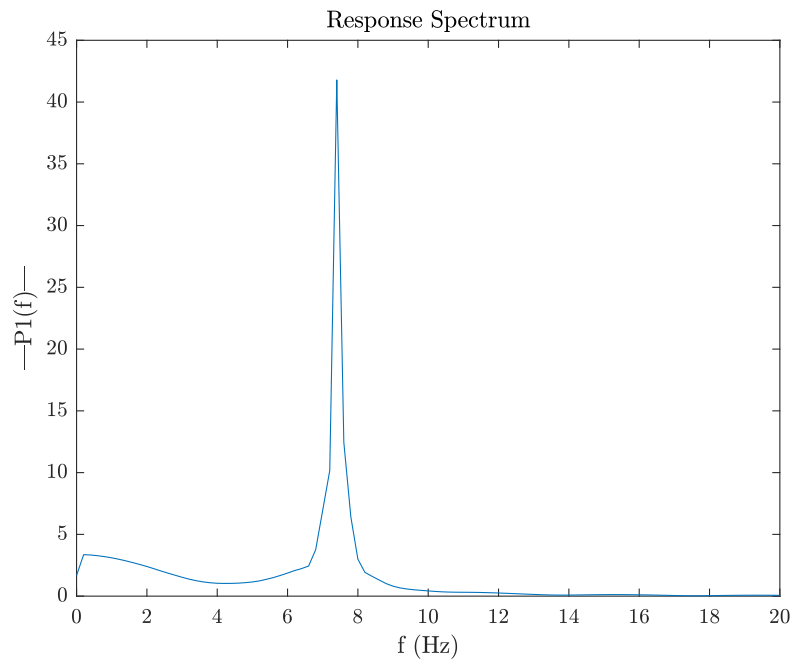


Figure 5.32: Response spectrum for  $U_r = 4.0$

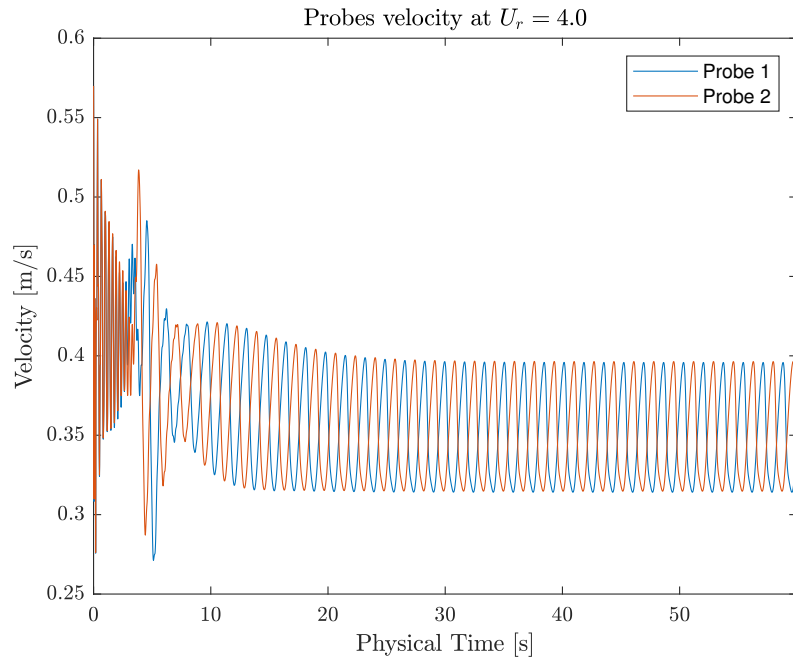


Figure 5.33: Probes Velocity for  $U_r = 4.0$

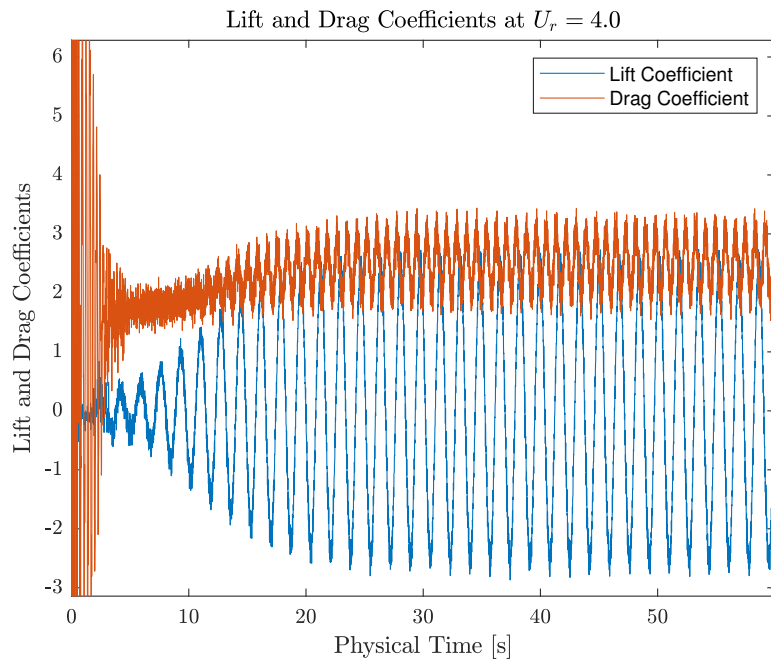


Figure 5.34: Lift and Drag Coefficients for  $U_r = 4.0$

### 5.4.3 Simulation at $U_r = 5.2$

In this simulation the **design reduced speed** equal to 5.2 was set.

$U_r$	$U$	$v_t$	$I$
5.2	0.57	0.057	0.1224

Table 5.9: Velocity inlet BC for  $U_r = 5.2$

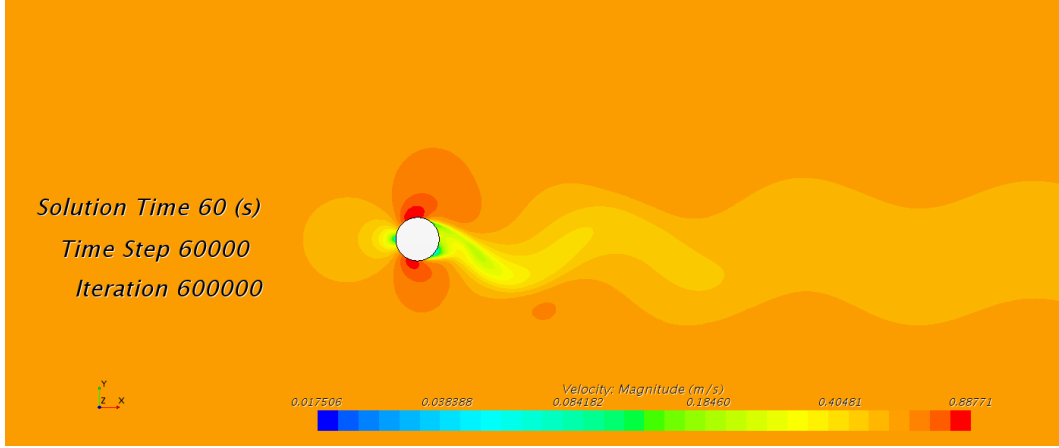


Figure 5.35: Velocity Magnitude scene for  $U_r = 5.2$

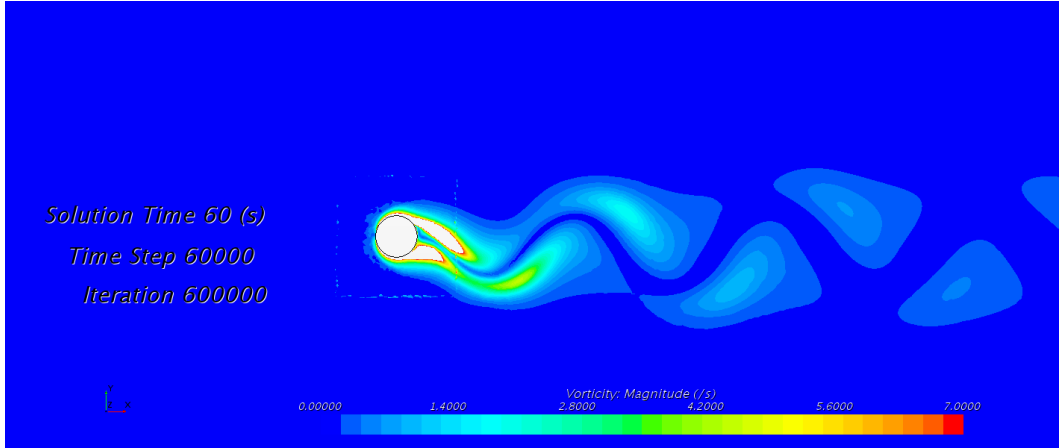


Figure 5.36: Vorticity Magnitude scene for  $U_r = 5.2$

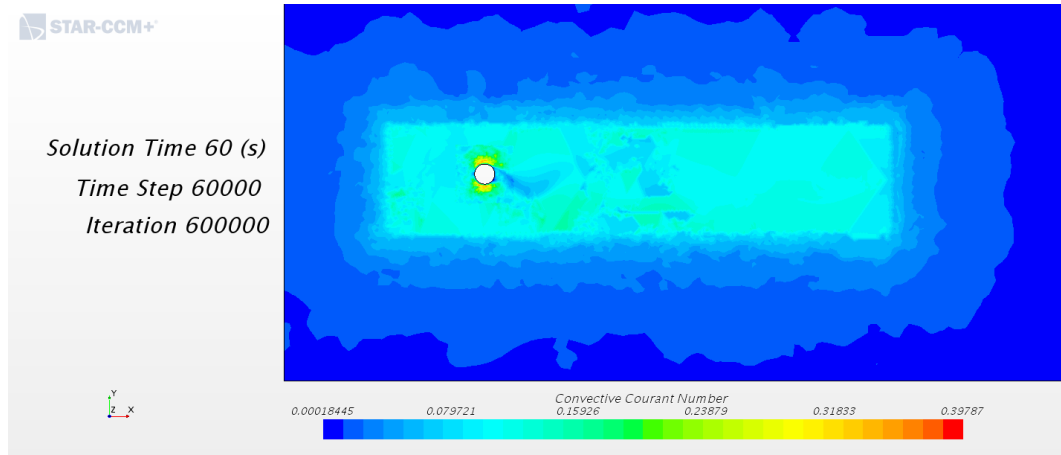


Figure 5.37: CFL scene for  $U_r = 5.2$

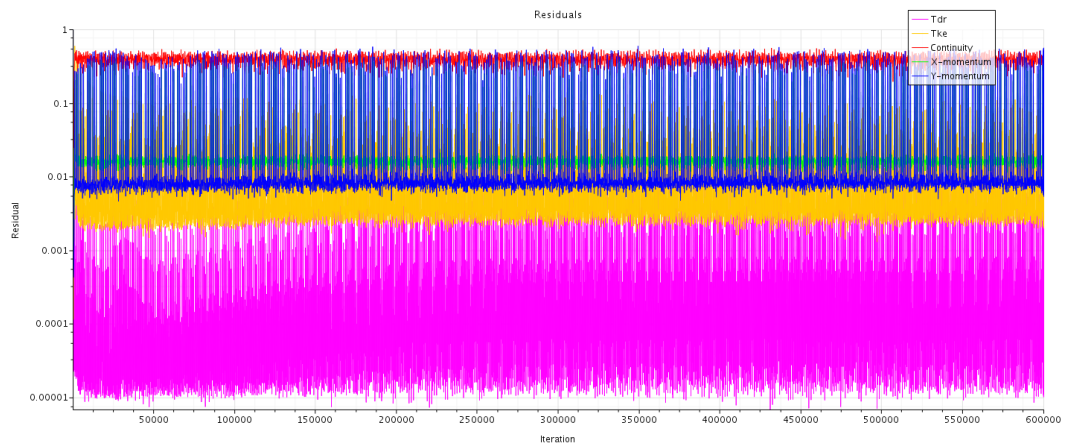


Figure 5.38: Residuals for  $U_r = 5.2$

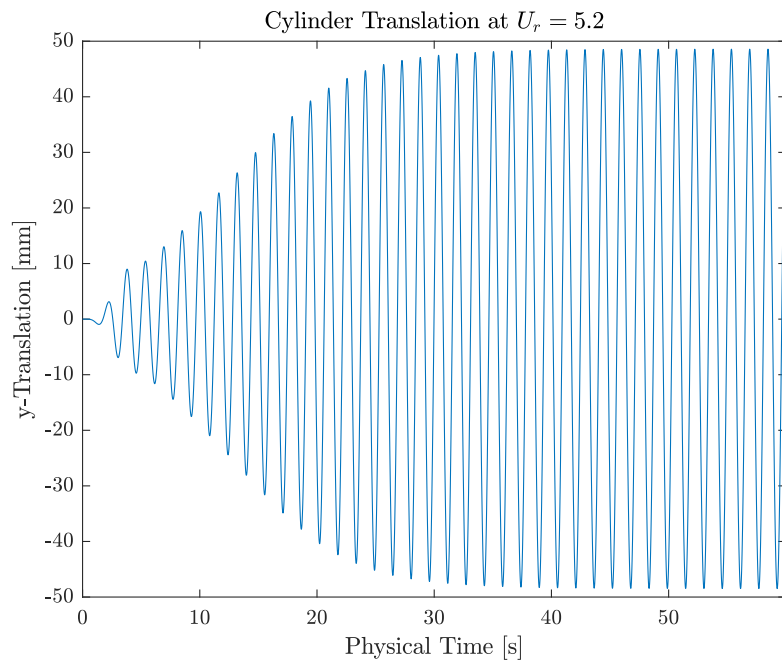


Figure 5.39: Translation plot for  $U_r = 5.2$

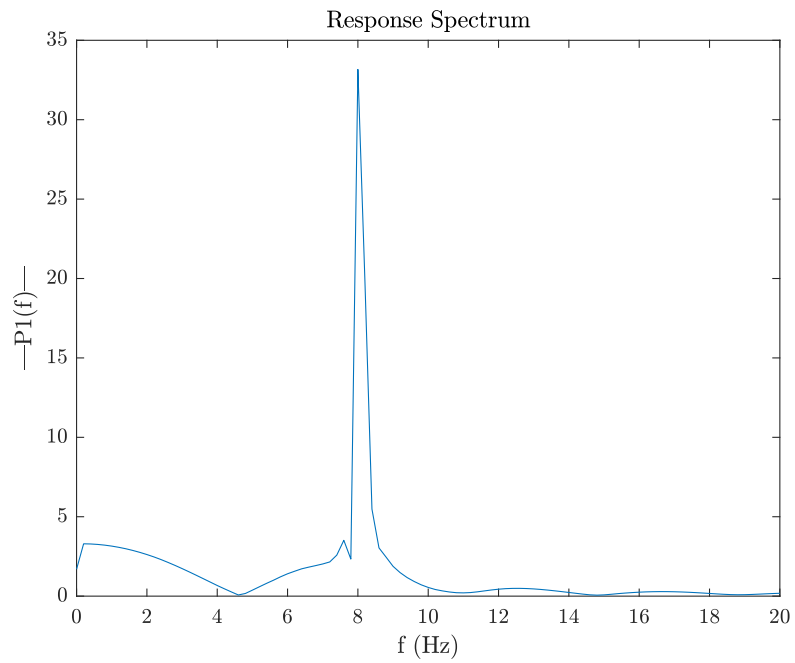


Figure 5.40: Response spectrum for  $U_r = 5.2$

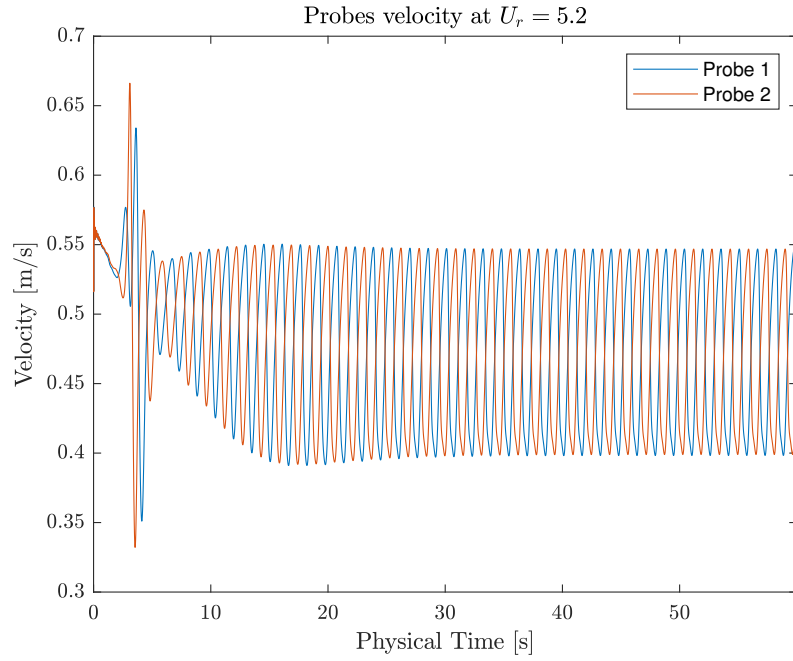


Figure 5.41: Probes Velocity for  $U_r = 5.2$

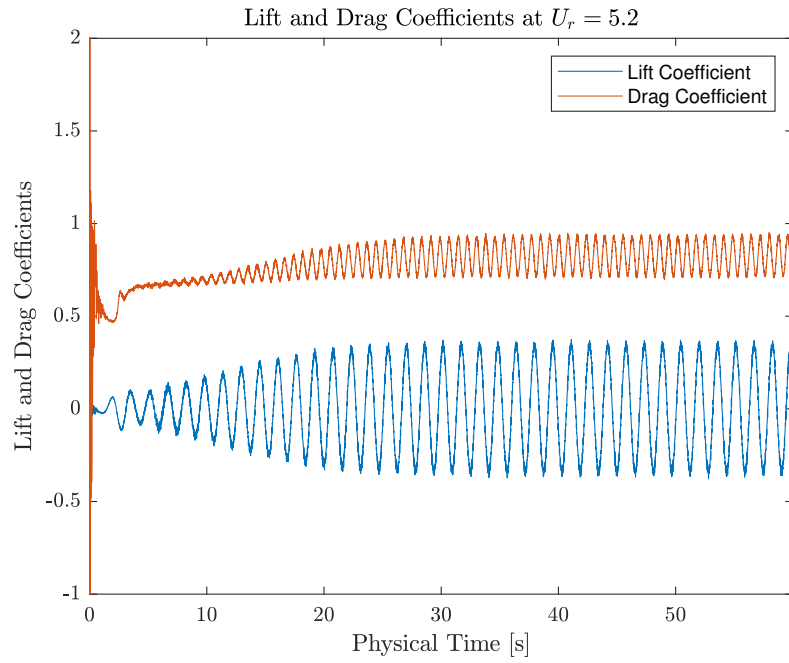


Figure 5.42: Lift and Drag Coefficients for  $U_r = 5.2$

#### 5.4.4 Simulation at $U_r = 6.5$

In this simulation the reduced velocity was increased to  $U_r = 6.5$ . It was expected a termination of VIV phenomenon, expectation that is confirmed by results below. Vortex shedding still occurs but gradually fades over time, as well as the translation response.

$U_r$	$U$	$v_t$	$I$
6.5	0.7125	0.0712	0.1224

Table 5.10: Velocity inlet BC for  $U_r = 6.5$

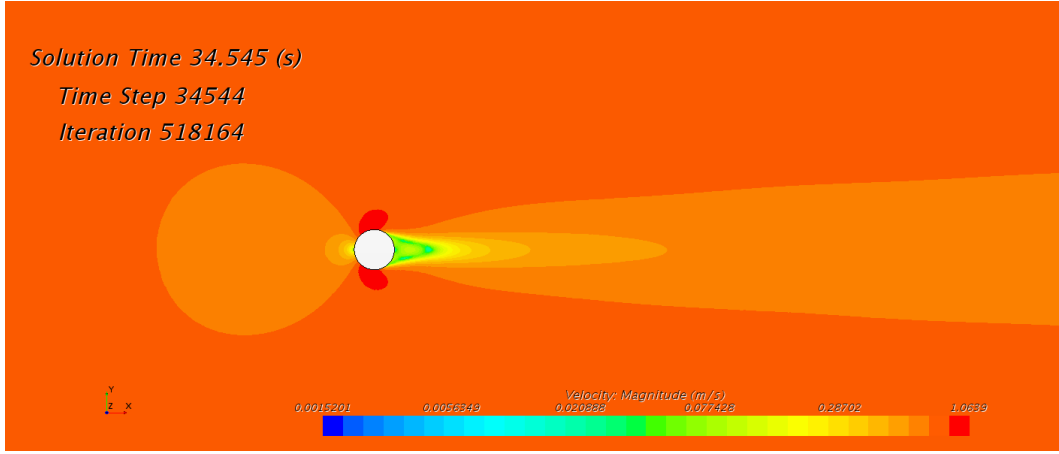


Figure 5.43: Velocity Magnitude scene for  $U_r = 6.5$

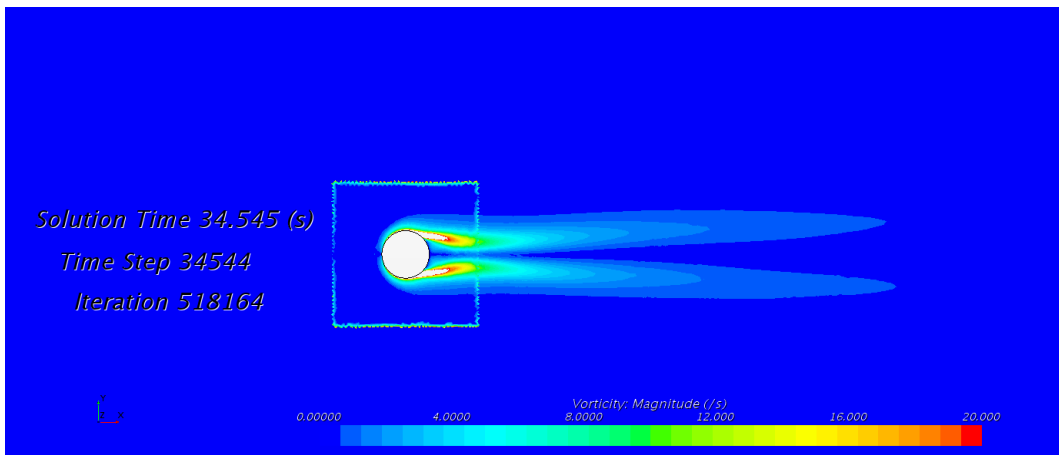


Figure 5.44: Vorticity Magnitude scene for  $U_r = 6.5$



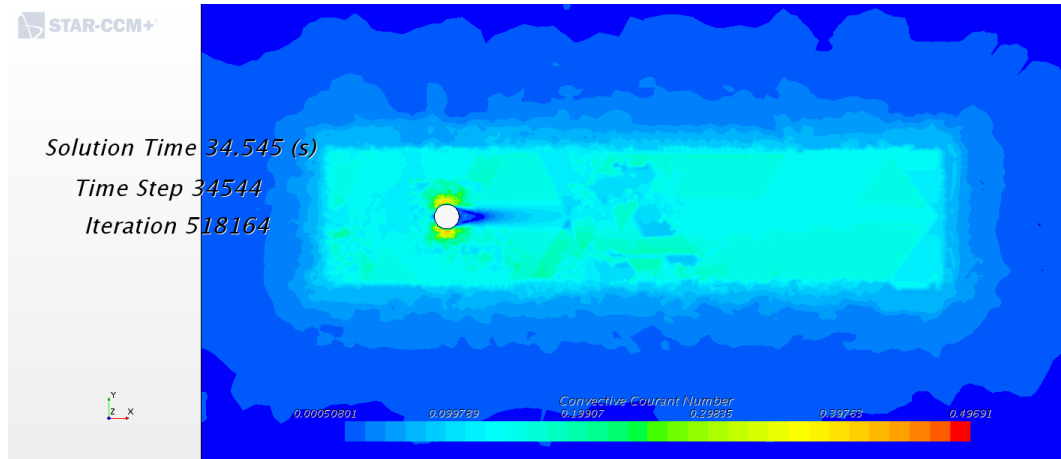


Figure 5.45: CFL scene for  $U_r = 6.5$

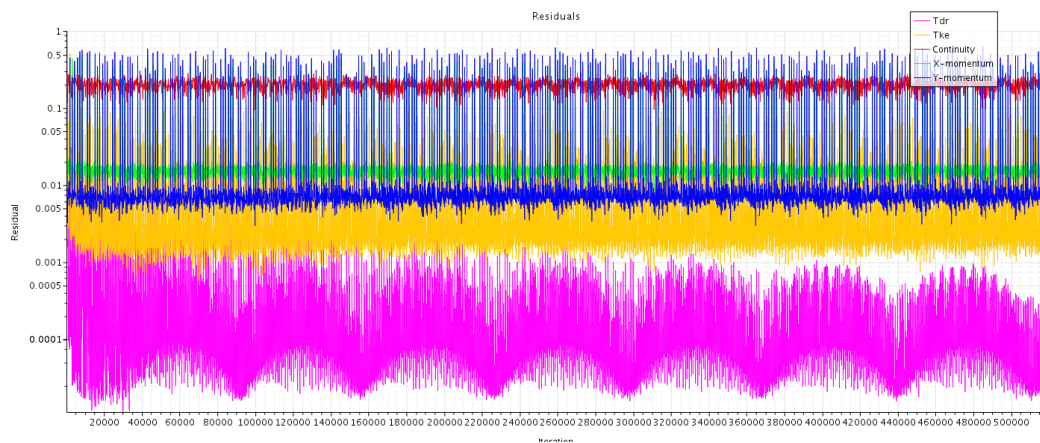


Figure 5.46: Residuals for  $U_r = 6.5$

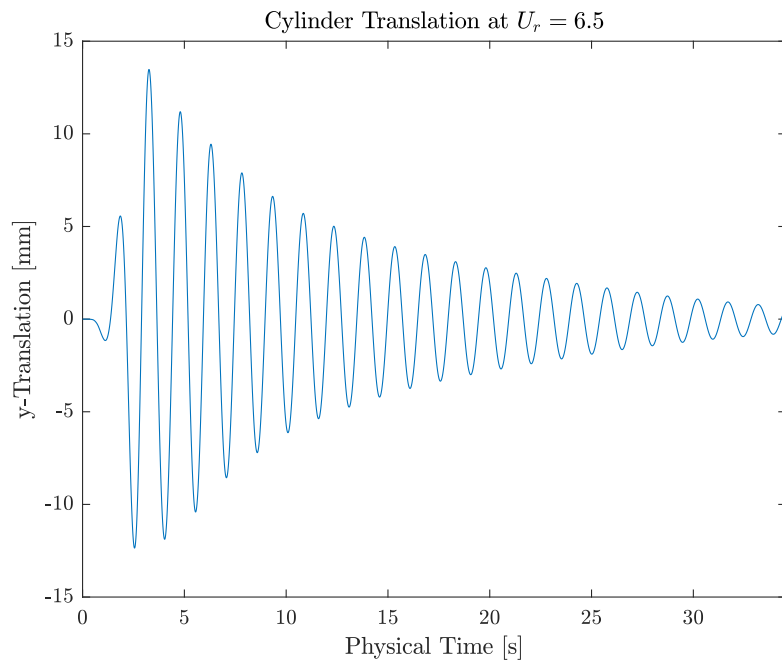


Figure 5.47: Translation plot for  $U_r = 6.5$

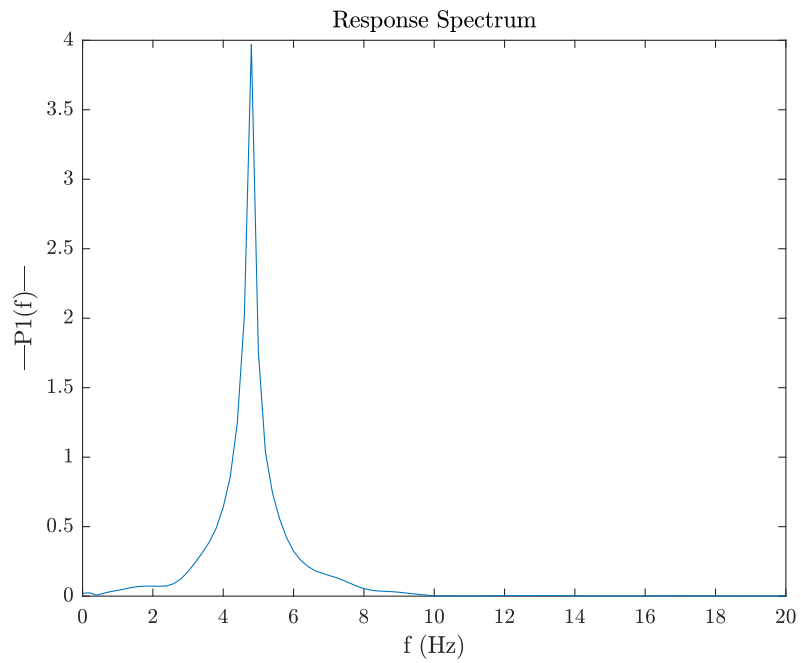


Figure 5.48: Response spectrum for  $U_r = 6.5$

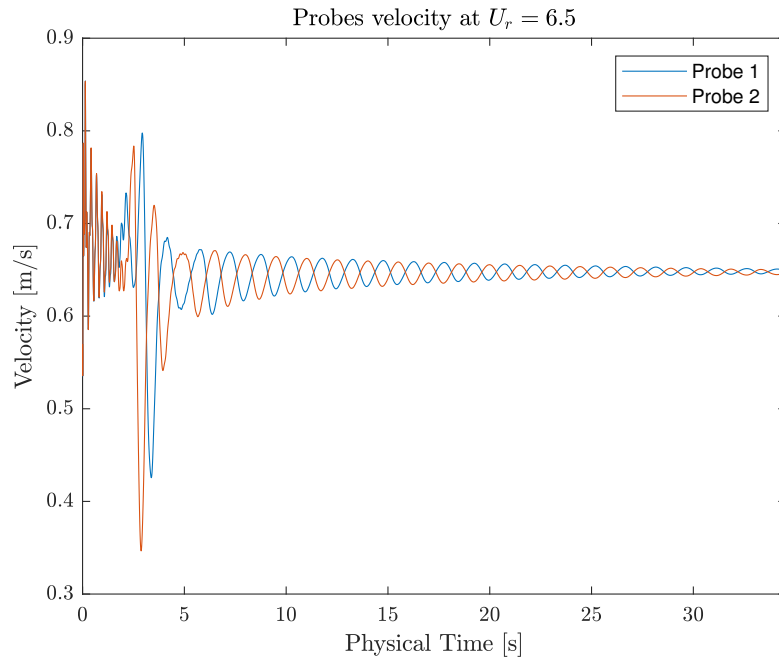


Figure 5.49: Probes Velocity for  $U_r = 6.5$

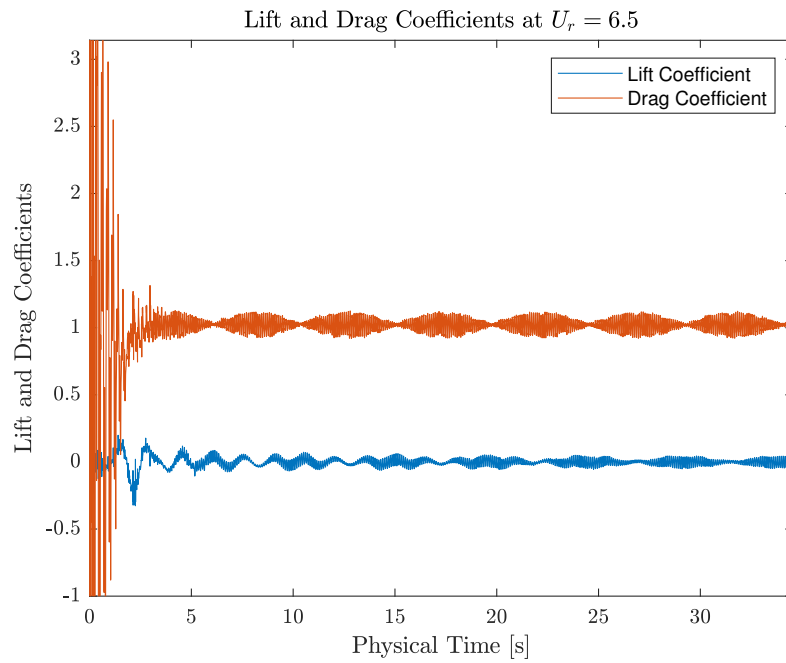


Figure 5.50: Lift and Drag Coefficients for  $U_r = 6.5$

#### 5.4.5 Simulation at $U_r = 8.0$

$U_r$	$U$	$v_t$	$I$
8	0.8769	0.0876	0.1224

Table 5.11: Velocity inlet BC for  $U_r = 8.0$

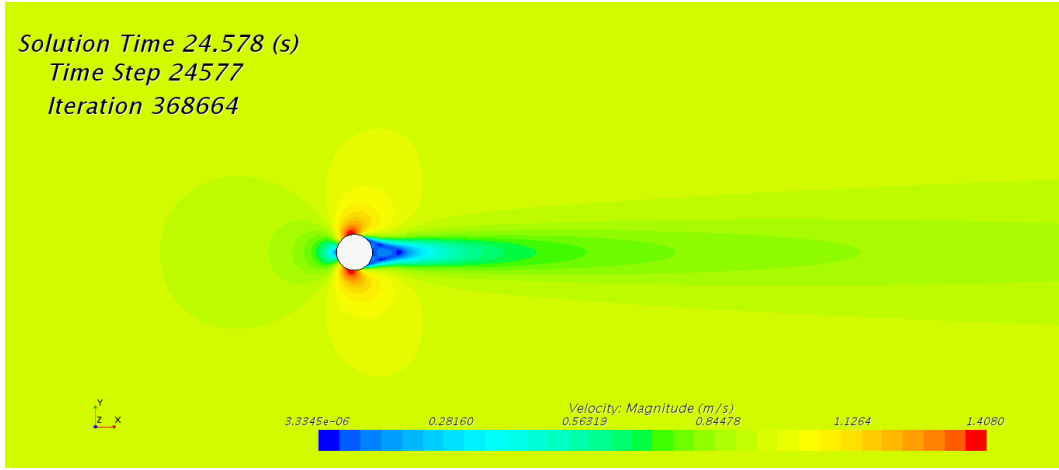


Figure 5.51: Velocity Magnitude scene for  $U_r = 8.0$

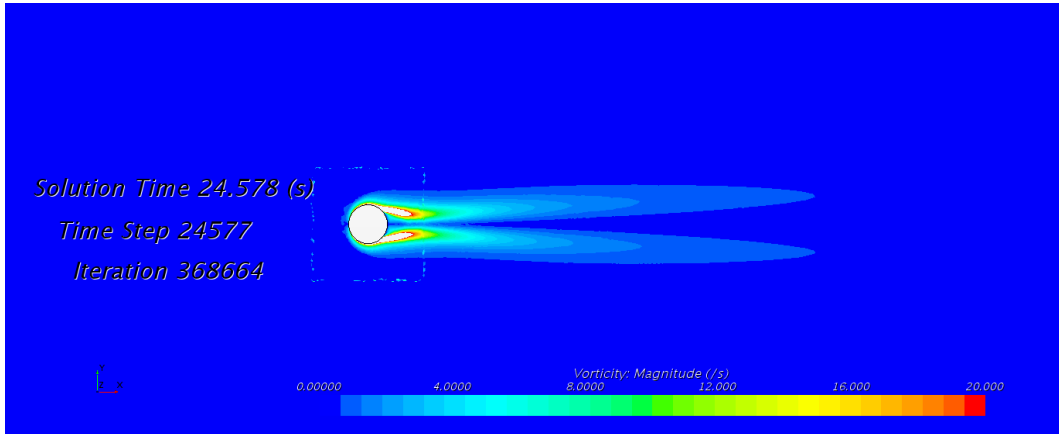


Figure 5.52: Vorticity Magnitude scene for  $U_r = 8.0$

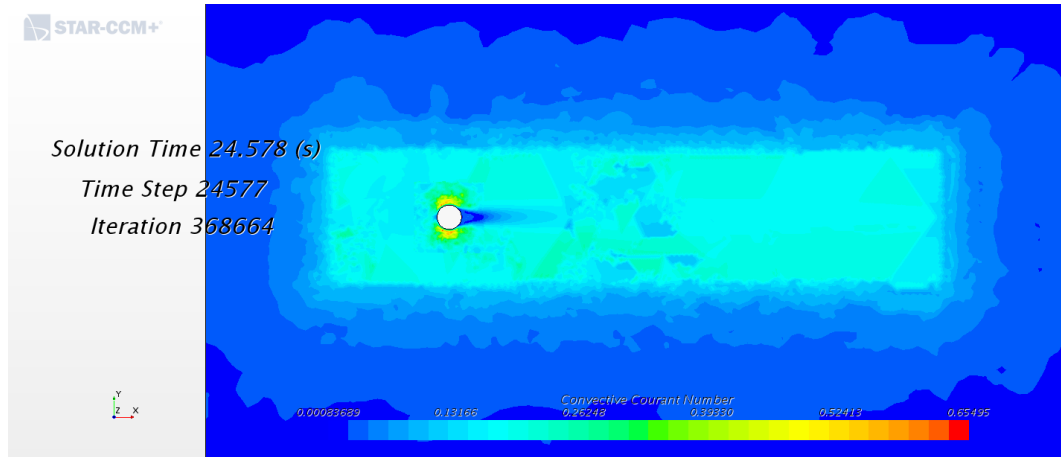


Figure 5.53: CFL scene for  $U_r = 8.0$

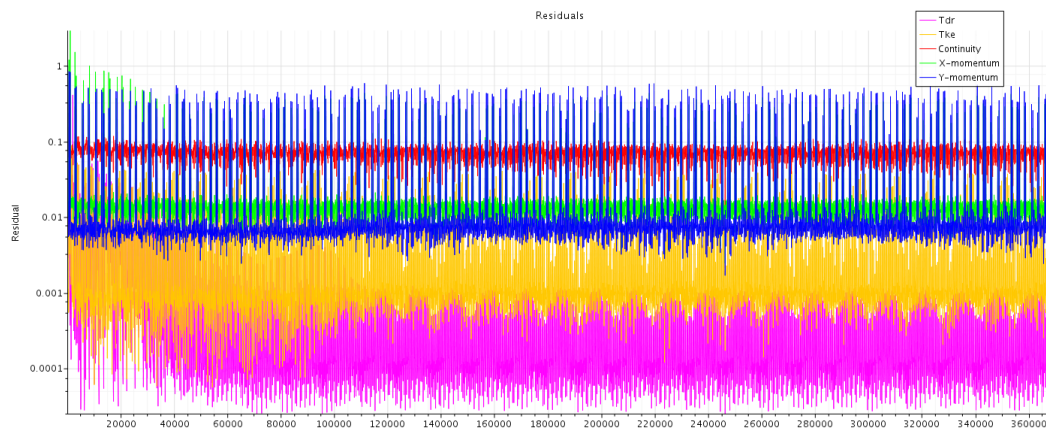


Figure 5.54: Residuals for  $U_r = 8.0$

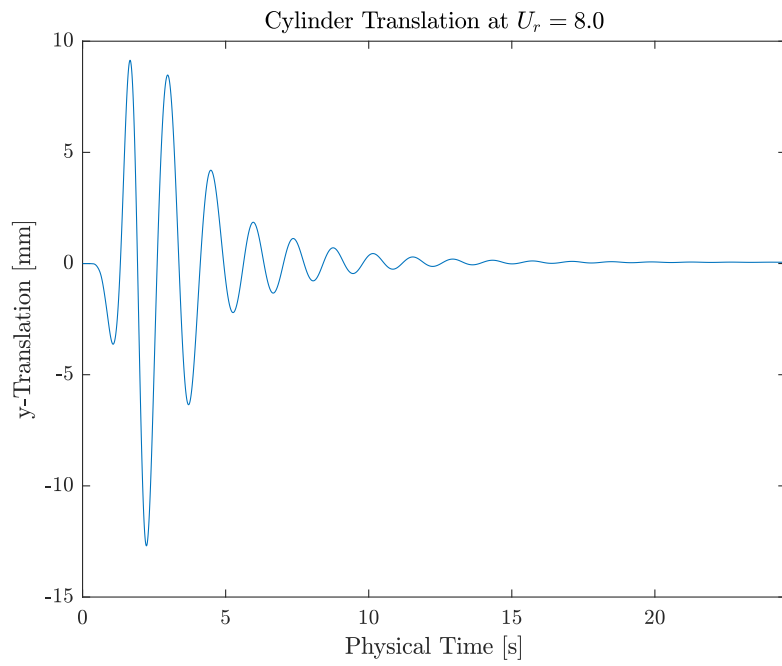


Figure 5.55: Translation plot for  $U_r = 8.0$

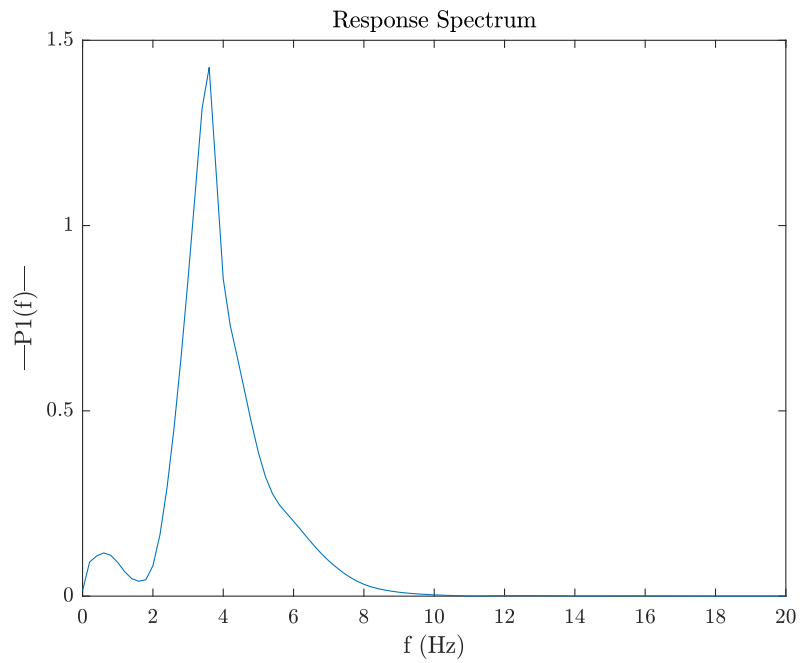


Figure 5.56: Response spectrum for  $U_r = 8.0$

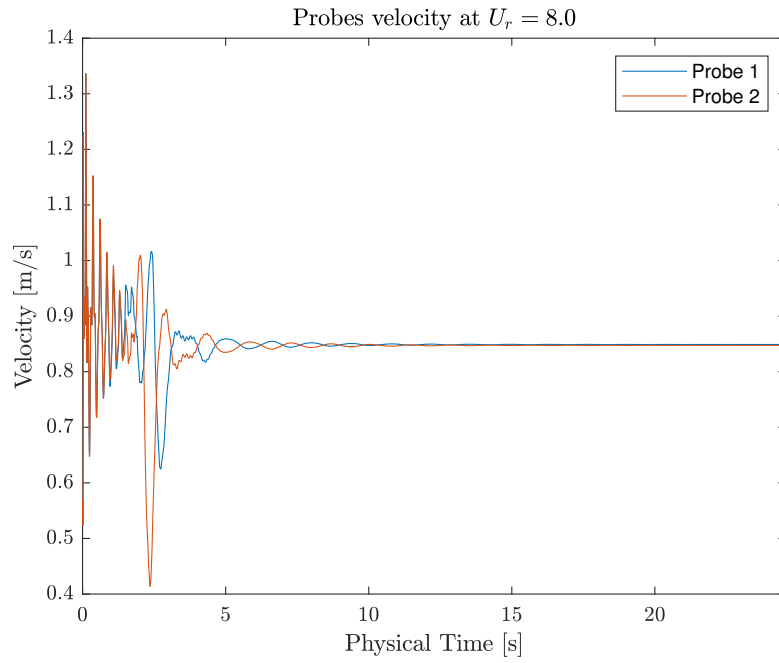


Figure 5.57: Probes Velocity for  $U_r = 8.0$

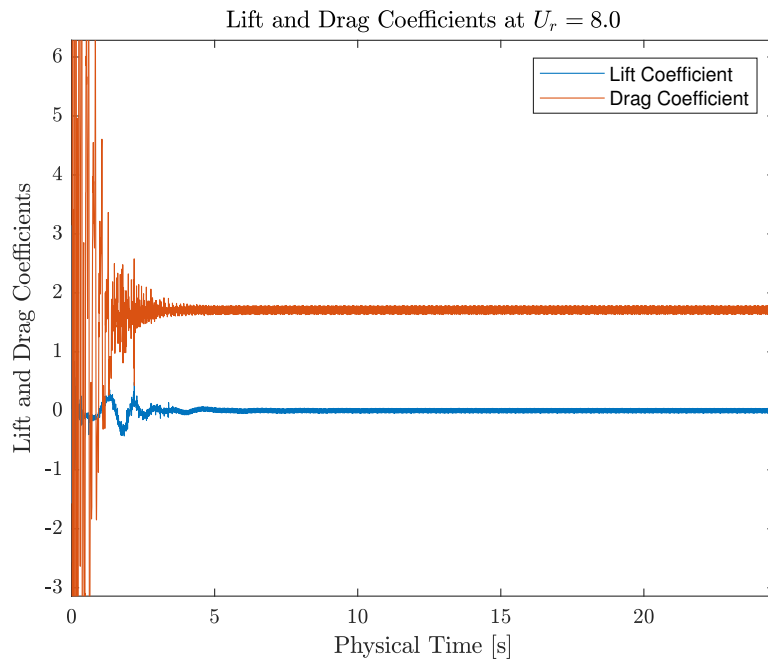


Figure 5.58: Lift and Drag Coefficients for  $U_r = 8.0$

# Acknowledgements





# Contents

<b>1</b>	<b>Introduction</b>	<b>2</b>
<b>2</b>	<b>State of the art</b>	<b>7</b>
2.1	The Saphonian . . . . .	7
2.2	O-Wind . . . . .	8
2.3	Vortex Bladeless . . . . .	8
2.4	VIVACE . . . . .	10
<b>3</b>	<b>Vortex Induced Vibrations</b>	<b>13</b>
3.1	Flow around cyliders and vortex shedding . . . . .	15
3.2	Lock-in . . . . .	17
3.3	Pattern of vortex shedding . . . . .	18
3.4	VIVs first harmonic model . . . . .	20
3.5	Dimensionless Parameters . . . . .	22
3.6	Classification of models . . . . .	27
<b>4</b>	<b>Numerical model and analysis</b>	<b>31</b>
4.1	Wake oscillator model . . . . .	31
4.1.1	Tuning parameters . . . . .	34
4.2	Numerical solution procedure . . . . .	39
4.3	Energy efficiency performances . . . . .	39
4.4	Dimensionless analysis and results . . . . .	40
4.5	Dimensional parameters design . . . . .	44
4.5.1	Case study . . . . .	46
4.6	Tuned system . . . . .	50
<b>5</b>	<b>Computational Fluid Dynamics analysis</b>	<b>55</b>
5.1	Methodology of CFD . . . . .	56
5.1.1	Governing equations . . . . .	56
5.1.2	Discretization FVM . . . . .	57
5.1.3	Solver or governing equations . . . . .	58
5.1.4	Turbulence . . . . .	60

5.2	Validation of CFD simulations . . . . .	63
5.2.1	Domain determination and mesh type . . . . .	63
5.2.2	Mesh quality . . . . .	63
5.2.3	Domain size . . . . .	65
5.2.4	Number of cells . . . . .	68
5.2.5	Discretization Error . . . . .	70
5.3	Simulations . . . . .	72
5.3.1	Domain and Mesh . . . . .	72
5.3.2	Overset Mesh . . . . .	73
5.3.3	DFBI Solver . . . . .	74
5.3.4	Model Setup . . . . .	75
5.4	Results . . . . .	77
5.4.1	Simulation at $U_r = 2.5$ . . . . .	77
5.4.2	Simulation at $U_r = 4.0$ . . . . .	81
5.4.3	Simulation at $U_r = 5.2$ . . . . .	85
5.4.4	Simulation at $U_r = 6.5$ . . . . .	89
<b>List of Tables</b>		97
<b>List of Figures</b>		99

# List of Tables

3.1	Dimensioless paramenters . . . . .	22
3.2	Data of experiments by Feng [11] and Khalak-Williamson [14] . . .	23
4.1	Values of tuning analysis . . . . .	35
4.2	Values of semi-empirical parameters in tuning analysis . . . . .	36
4.3	Initial condition for the first iteration . . . . .	39
4.4	Mass ratio and damping values for the dimensionless analysis . . . .	40
5.1	Mesh quality measures in grid analysis . . . . .	65
5.2	Strhoual numbr at low Reynolds $Re$ to evaluate the distance between cylinder and outlet face. . . . .	67
5.3	2D triangular mesher parameters. . . . .	69
5.4	Convergence data . . . . .	69
5.5	Cases analyzed . . . . .	72
5.6	Domain geometric characteristics . . . . .	72
5.7	Velocity inlet BC for $U_r = 2.5$ . . . . .	77
5.8	Velocity inlet BC for $U_r = 4.0$ . . . . .	81
5.9	Velocity inlet BC for $U_r = 5.2$ . . . . .	85
5.10	Velocity inlet BC for $U_r = 6.5$ . . . . .	89



# List of Figures

1.1	Actuator disc model of airstream flow through turbine . . . . .	3
1.2	Size growth of wind turbines over time [9] . . . . .	5
2.1	The Saphonian . . . . .	7
2.2	O-Wind Turbine . . . . .	8
2.3	Vortex Bladeless . . . . .	9
2.4	Scheme of omnidirectional piezoelectric energy converter . . . . .	9
2.5	VIVACE . . . . .	11
3.1	Feedback between fluid and structure . . . . .	13
3.2	A classification of flow induced vibrations . . . . .	14
3.3	Flow around cylinder varying $Re$ [26] . . . . .	15
3.4	Flow in the near wake of a cylinder starting from rest [20] . . . . .	16
3.5	Frequency response in air (a) and water (b) with regard to cross-flow vibrations [26] . . . . .	17
3.6	Map of vortex synchronization regions . . . . .	18
3.7	2S Mode . . . . .	19
3.8	2P Mode . . . . .	19
3.9	P+S Mode . . . . .	19
3.10	Scheme of cylinder elastically mounted . . . . .	20
3.11	Feng's experimental data at high mass ratio . . . . .	23
3.12	Khalak and Williamson's experimental data at small mass ratio . . . . .	23
3.13	Response of low $m^*\zeta$ system . . . . .	24
3.14	Griffin Plot . . . . .	25
3.15	Effect of mass-damping parameter on the range of lock-in in terms of reduced velocity $U_r$ . . . . .	26
3.16	Combined effect of reduced velocity-Strouhal number and mass-damping parameter on amplitude ratio of motion of an elastically mounted cylinder due to VIV . . . . .	27
3.17	Classification of VIV models . . . . .	28
4.1	1DoF model of coupled structure and wake oscillator . . . . .	32
4.2	Khalak & Williamson experimental data (1997) [13] . . . . .	35
4.3	Effect of threshold of reduced velocity which separates Upper Branch from Lower . . . . .	36

4.4	(a) $A$ in LB . . . . .	37
4.5	(b) $\varepsilon$ in LB . . . . .	37
4.6	(c) $A$ in UB . . . . .	37
4.7	(d) $\varepsilon$ in UB . . . . .	37
4.8	Dependency of semi-empirical parameters $A$ and $\varepsilon$ on amplitude ratio - reduced velocity chart. . . . .	37
4.9	Some of tests conducted in order to calibrate model on Khalak & Williamson experimental data at very low mass ratio . . . . .	38
4.10	$A^*$ for $m^* = 1.5$ . . . . .	41
4.11	$A^*$ for $m^* = 2$ . . . . .	41
4.12	$A^*$ for $m^* = 2.36$ . . . . .	41
4.13	$A^*$ for $m^* = 2.5$ . . . . .	41
4.14	$A^*$ for $m^* = 3$ . . . . .	41
4.15	Trend of max amplitude ratio versus mass ratio for $\zeta = 0.0045$ . . .	41
4.16	$A^*$ for $\zeta = 0.0045$ . . . . .	42
4.17	$A^*$ for $\zeta = 0.0877$ . . . . .	42
4.18	$A^*$ for $\zeta = 0.1293$ . . . . .	42
4.19	$A^*$ for $\zeta = 0.1709$ . . . . .	42
4.20	$A^*$ for $\zeta = 0.2541$ . . . . .	42
4.21	Trend of max amplitude ratio versus damping for $m^* = 2.36$ . . . .	42
4.22	Maximum efficiency $\eta$ versus damping factor $\zeta$ for each mass ratio $m^*$	43
4.23	Maximum efficiency of conversion versus mass-damping parameter $m^*\zeta$ . . . . .	44
4.24	3D plot of $A^*$ for $m^* = 2.5$ . . . . .	45
4.25	3D plot of $\eta$ for $m^* = 2.5$ . . . . .	45
4.26	AWAC position in the island of Pantelleria . . . . .	46
4.27	AWAC system . . . . .	46
4.28	Sea-current speed . . . . .	47
4.29	Sea-current direction occurrences . . . . .	47
4.30	Sea-current probability and Weibull PDF . . . . .	48
4.31	Amplitude response for each diameter $D$ considered in the dimen- sional analysis and design . . . . .	50
4.32	Power extracted before conversion to electrical power for each diameter	51
4.33	Electrical power extracted for each diameter . . . . .	51
4.34	Power density referred to the stroke of cylinder . . . . .	52
4.35	Power density referred to occupied surface . . . . .	52
4.36	3D plot of power extracted in tuned system for different diameters .	53
4.37	Power extracted in tuned system for different diameters . . . . .	53
5.1	Finite Volume Method Discretization . . . . .	58
5.2	DNS (left), LES (middle) and RANS (right) predictions of a turbu- lent jet. - A. Maries, University of Pittsburgh . . . . .	61
5.3	Face validity . . . . .	64

5.4	Volume change . . . . .	64
5.5	Cell quality . . . . .	64
5.6	Skewness angle . . . . .	64
5.7	Triangular Mesh . . . . .	66
5.8	Polyhedral Mesh . . . . .	66
5.9	Quadrilateral mesh . . . . .	66
5.10	Mesh setups in grid quality analysis . . . . .	66
5.11	Simulation at low Reynolds number $Re = 75$ to observe vortex shedding for the evaluation of Sthroual and distance between cylinder and outlet . . . . .	67
5.12	Drag and Lift coefficient at low Re $Re = 75$ in domain size analysis and frequency analysis through Fast Fourier Transformation FFT. . . . .	67
5.13	Domain geometry in CAD environment. . . . .	68
5.14	No. cells convergence . . . . .	69
5.15	Domain sizes in VIVs simulation . . . . .	72
5.16	Mesh regions in VIVs simulation . . . . .	73
5.17	Data transfer between overset mesh and background . . . . .	74
5.18	Overset Cell Status . . . . .	74
5.19	Linear spring coupling . . . . .	75
5.20	Prism Layer Mesh . . . . .	76
5.21	Velocity Magnitude scene for $U_r = 2.5$ . . . . .	78
5.22	Vorticity Magnitude scene for $U_r = 2.5$ . . . . .	78
5.23	Residuals for $U_r = 2.5$ . . . . .	78
5.24	Translation plot for $U_r = 2.5$ . . . . .	79
5.25	Probes Velocity for $U_r = 2.5$ . . . . .	79
5.26	Lift and Drag Coefficients for $U_r = 2.5$ . . . . .	80
5.27	Velocity Magnitude scene for $U_r = 4.0$ . . . . .	81
5.28	Vorticity Magnitude scene for $U_r = 4.0$ . . . . .	81
5.29	CFL scene for $U_r = 4.0$ . . . . .	82
5.30	Residuals for $U_r = 4.0$ . . . . .	82
5.31	Translation plot for $U_r = 4.0$ . . . . .	83
5.32	Response spectrum for $U_r = 4.0$ . . . . .	83
5.33	Probes Velocity for $U_r = 4.0$ . . . . .	84
5.34	Lift and Drag Coefficients for $U_r = 4.0$ . . . . .	84
5.35	Velocity Magnitude scene for $U_r = 5.2$ . . . . .	85
5.36	Vorticity Magnitude scene for $U_r = 5.2$ . . . . .	85
5.37	CFL scene for $U_r = 5.2$ . . . . .	86
5.38	Residuals for $U_r = 5.2$ . . . . .	86
5.39	Translation plot for $U_r = 5.2$ . . . . .	87
5.40	Response spectrum for $U_r = 5.2$ . . . . .	87
5.41	Probes Velocity for $U_r = 5.2$ . . . . .	88
5.42	Lift and Drag Coefficients for $U_r = 5.2$ . . . . .	88



5.43	Velocity Magnitude scene for $U_r = 6.5$	89
5.44	Vorticity Magnitude scene for $U_r = 6.5$	89
5.45	CFL scene for $U_r = 6.5$	90
5.46	Residuals for $U_r = 6.5$	90
5.47	Translation plot for $U_r = 6.5$	91
5.48	Response spectrum for $U_r = 6.5$	91
5.49	Probes Velocity for $U_r = 6.5$	92
5.50	Lift and Drag Coefficients for $U_r = 6.5$	92

# Bibliography

- [1] A. Abdelkefi. «Aeroelastic energy harvesting: A review». In: *International Journal of Engineering Science* 100 (Mar. 2016), pp. 112–135.
- [2] Othmar H. Amman, Theodore von Kármán, and Glenn B. Woodruff. *The failure of the Tacoma Narrows Bridge*. Tech. rep. Caltech, 1941.
- [3] Antonio Barrero-Gil, Santiago Pindado, and Sergio Avila. «Extracting energy from vortex-induced vibrations: a parametric study». In: *Applied mathematical modelling* 36.7 (2012), pp. 3153–3160.
- [4] M.M. Bernitsas and Raghavan K. «Fluid Motion Energy Converter». In: *United States Patent and Trademark Office, Patent no. 7,493,759* (2009).
- [5] Richard Bishop et al. «The lift and drag forces on a circular cylinder oscillating in a flowing fluid». In: *277 Proceedings of the Royal Society A, London* (1964).
- [6] Robert D. Blevins. *Flow-Induced Vibration*. Krieger Publishing Company, 2001.
- [7] J.C. Cajasa et al. «SHAPE Project Vortex Bladeless: Parallel multi-code coupling for Fluid-Structure Interaction in Wind Energy Generation». In: *PRACE 4th Implementation Phase, European's commission project* (2016).
- [8] Althesys Strategic Consultant. «Il rinnovamento del parco eolico italiano». In: 2016.
- [9] European Wind Energy Association (now Wind Europe). «Wind Energy Fact-sheets». In: 2010.
- [10] Matteo Luca Facchinetti, Emmanuel De Langre, and Francis Biolley. «Coupling of structure and wake oscillators in vortex-induced vibrations». In: *Journal of Fluids and structures* 19.2 (2004), pp. 123–140.
- [11] C.C. Feng. «The measurement of vortex-induced effects in flow past stationary and oscillating circular and d-section cylinders». MA thesis. University of British Columbia, Vancouver, BC, Canada, 1968.
- [12] Ronald T Hartlen and Iain G Currie. «Lift-oscillator model of vortex-induced vibration». In: *Journal of the Engineering Mechanics Division* 96.5 (1970), pp. 577–591.

- [13] A. Khalak and Williamson CHK. «Fluid forces and dynamics of a hydroelastic structure with very low mass and damping». In: *Journal of Fluids and Structures* 11.8 (1997), pp. 973–982.
- [14] A. Khalak and C.K.H. Williamson. «Motion, forces and mode transitions in vortex-induced at low mass–damping». In: *Journal of Fluids and Structures* 13 (1999), pp. 813–851.
- [15] Steen Krenk and Søren RK Nielsen. «Energy balanced double oscillator model for vortex-induced vibrations». In: *Journal of Engineering Mechanics* 125.3 (1999), pp. 263–271.
- [16] V. Kurushina et al. «Calibration and comparison of VIV wake oscillator models for low mass ratio structures». In: *International Journal of Mechanical Sciences* (2018), pp. 142–143, 547–560.
- [17] Mannini C. Marra A. and Bartoli G. «Van der pol-type equation for modeling vortex-induced oscillations of bridge decks». In: *Journal of Wind Engineering and Industrial Aerodynamics* 99 (2011), pp. 776–785.
- [18] T.L. Morse and C.H.K. Williamson. «Prediction of vortex-induced vibration response by employing controlled motion». In: *J. Fluid Mech* 634 (2009), pp. 5–39.
- [19] Michael P. Païdoussis, Stuart J. Price, and Emmanuel de Langre. *Fluid-Structure Interactions: Cross-Flow-Induced Instabilities*. Cambridge University Press, 2010.
- [20] A. E. Perry, M. S. Chong, and T. T. Lim. «The vortex-shedding process behind two-dimensional bluff bodies». In: *Journal of Fluid Mechanics* 116 (1982), pp. 77–90.
- [21] Patrick J Roache. «Perspective: a method for uniform reporting of grid refinement studies». In: *Journal of fluids engineering* 116.3 (1994), pp. 405–413.
- [22] Turgut Sarpkaya. «A critical review of the intrinsic nature of vortex-induced vibrations». In: *Journal of fluids and structures* 19.4 (2004), pp. 389–447.
- [23] Hermann Schlichting and Klaus Gersten. *Boundary-layer theory*. Springer, 2016.
- [24] Siemens. *Simcenter STAR-CCM+ Software User Manual*. Retrived at the URL "<https://www.plm.automation.siemens.com/global/en/products/simcenter/STAR-CCM.html>". 2019.
- [25] RA Skop and S Balasubramanian. «A new twist on an old model for vortex-excited vibrations». In: *Journal of Fluids and Structures* 11.4 (1997), pp. 395–412.

- [26] B. Sumer and J. Fredsøe. «Hydrodynamics around cylindrical structures». In: *In Advanced Series on Ocean Engineering* 12 (1997).
- [27] S. Taneda. «Experimental investigation of the wakes behind cylinders and plates at low reynolds numbers». In: *Journal of the Physical Society of Japan* 11.3 (1956), pp. 77–90.
- [28] Associazione Nazionale Energia del Vento. «Il contributo dell’eolico italiano per il raggiungimento degli obiettivi al 2030». In: 2017.
- [29] NPARC Alliac CFD Verification and Validation Web Site NASA. *Examining Spatial (Grid) Convergence*. 2008. URL: <http://https://www.grc.nasa.gov/WWW/wind/valid/tutorial/spatconv.html> (visited on ).
- [30] C.H.K. Williamson and Roshko A. «Vortex formation in the wake of an oscillating cylinder». In: *Journal of Fluids and Structures* 2.4 (1988), pp. 355–381.
- [31] M. M. Zdravkovich. *Flow around Circular Cylinders; Volume 1. Fundamentals*. Oxford University Press, Oxford, 1997.
- [32] M. M. Zdravkovich. *Flow around Circular Cylinders; Volume 2. Applications*. Oxford University Press, 2003.
- [33] Ming Zhao, Liang Cheng, and Hongwei An. «Numerical investigation of vortex-induced vibration of a circular cylinder in transverse direction in oscillatory flow». In: *Ocean Engineering* 41 (2012), pp. 39–52.